

## REVIEW

### Fundamental concepts, design rules and potentials in radiative cooling

To cite this article: Zhuning Wang *et al* 2025 *Rep. Prog. Phys.* **88** 045901

View the [article online](#) for updates and enhancements.

## You may also like

- [Molecular nanomagnets: a viable path toward quantum information processing?](#)  
A Chiesa, P Santini, E Garlatti et al.
- [Mechanical, electronic, optical, piezoelectric and ferroic properties of strained graphene and other strained monolayers and multilayers: an update](#)  
Gerardo G Naumis, Saúl A Herrera, Shiva P Poudel et al.
- [Many-body localization in the age of classical computing](#)  
Piotr Sierant, Maciej Lewenstein, Antonello Scardicchio et al.



www.hidenanalytical.com  
info@hiden.co.uk

## HIDEN ANALYTICAL

### Instruments for Advanced Science

Mass spectrometers for vacuum, gas, plasma and surface science



#### Residual Gas Analysis

Perform RGA at UHV/XHV. Our RGA configurations include systems for UHV science applications including temperature-programmed desorption and electron/photon stimulated desorption.

#### Thin Film Surface Analysis

Conduct both static and dynamic SIMS analysis with a choice of primary ions for full chemical composition and depth profiling. Our SIMS solutions include complete workstations and bolt-on modules.

#### Plasma Characterisation

Fully characterise a range of plasmas: RF, DC, ECR and pulsed plasmas, including neutrals and neutral radicals. Extend your analyses to atmospheric pressure processes using the HPR-60, with time-resolved mass/energy analysis.

 [www.HidenAnalytical.com](http://www.HidenAnalytical.com)

 [info@hiden.co.uk](mailto:info@hiden.co.uk)

This content was downloaded from IP address 222.205.47.26 on 14/04/2025 at 12:47

## Review

# Fundamental concepts, design rules and potentials in radiative cooling

Zhuning Wang , Sijie Pian, Yulei Zhang and Yaoguang Ma\* 

State Key Laboratory for Extreme Photonics and Instrumentation, College of Optical Science and Engineering, International Research Center for Advanced Photonics, ZJU–Hangzhou Global Scientific and Technological Innovation Center, Intelligent Optics and Photonics Research Center, Jiaxing Research Institute, Zhejiang University, Hangzhou 310027, People's Republic of China

E-mail: [mayaoguang@zju.edu.cn](mailto:mayaoguang@zju.edu.cn)

Received 16 October 2024, revised 25 March 2025

Accepted for publication 28 March 2025

Published 10 April 2025

Corresponding editor: Dr Roberta Palacino



### Abstract

Amidst the escalating environmental concerns driven by global warming and the detrimental impacts of extreme climates, energy consumption and greenhouse gas emissions associated with refrigeration have reached unprecedented levels. Radiative cooling, as an emerging renewable cooling technology, has been positioned as a pivotal strategy in the fight against global warming. This review examines the theoretical model of radiative cooling emitters and complex practical environment. We first investigate the thermodynamic interactions between environmental factors and the cooling surface, followed by an examination of innovative modulation techniques such as asymmetric/non-reciprocal radiative heat transfer mechanisms. Additionally, we summarize the latest advancements in structural design and simulation methodologies for radiative cooling materials at the device level. We then delve into potential applications of radiative cooling materials in various scenarios including energy-efficient construction, personal thermal management, photovoltaic cooling, and dynamic passive daytime radiative cooling materials with seasonal adaptability. In conclusion, we provide a comprehensive overview of this technology's strengths and current challenges to inspire further research and application development in radiative cooling technology with a focus on contributing towards energy conservation objectives and promoting a sustainable society.

Keywords: radiative cooling, thermal photonics, atmospheric window, directional thermal radiation, non-reciprocal thermal radiation, structural optimization design, dynamic thermal management

\* Author to whom any correspondence should be addressed.

## Contents

1. Introduction	2	4.2.4. Electrochromic materials.	33
2. Fundamentals of radiative sky cooling	3	4.3. Thermal control material with environmental adaptability	33
2.1. Thermodynamic equilibrium of a solid surface emitter	3	4.3.1. Thermo-hygroscopic response-induced mechanical deformation.	33
2.2. Environmental impact on the efficacy of radiative cooling	5	4.3.2. Radiation cooling devices with thermochromic materials.	34
2.2.1. Atmospheric transparency spectrum shaping	5	5. Challenge and outlook	35
2.2.2. Estimation of non-radiative heat transfer coefficients	7	Data availability statement	37
2.3. Performance analysis based on spectral and spatial characteristics	8	Acknowledgments	37
2.3.1. Performance of emitters with multiband emissivity modulation.	10	References	37
2.3.2. Performance of emitters with angular emissivity modulation.	12		
2.4. Theoretical models refined for practical scenarios	12		
2.4.1. Thermal management in a thermostatically controlled indoor environment.	12		
2.4.2. Thermal management of emitter under thermal source influence.	13		
2.4.3. Thermal management of emitter with varying posture and orientation.	14		
2.4.4. Thermal management of emitter with limited radiating angle range.	14		
3. Design of radiation cooling structures	15		
3.1. Typical optical simulation methods in the design of radiative cooling structures	15		
3.1.1. Transfer matrix method (TMM).	16		
3.1.2. Effective medium theory (EMT).	16		
3.1.3. Monte Carlo method (MCM).	16		
3.1.4. Full-wave electromagnetic simulation.	16		
3.2. Design of periodic photonic structures	17		
3.2.1. Photonic crystal.	17		
3.2.2. Metasurface.	17		
3.3. Design of aperiodic photonic structures	18		
3.3.1. Aperiodic multilayer film.	18		
3.3.2. Random particles.	18		
3.3.3. Porous polymer structure.	18		
3.3.4. Fiber-textile structure.	18		
4. Progress and applications of radiative cooling technology	19		
4.1. Radiation cooling devices for multi-scenario	19		
4.1.1. Energy-efficient building.	20		
4.1.2. PTM.	20		
4.1.3. PV cooling.	20		
4.1.4. Other potential and extension applications.	20		
4.2. Active dynamic thermal management	21		
4.2.1. Janus structure with asymmetric spectral design.	21		
4.2.2. Mechanical stretchable optical structure.	22		
4.2.3. Moisture transfer technique.	22		

## 1. Introduction

The environmental issues exacerbated by global warming, coupled with the detrimental effects of extreme climates, have become increasingly severe. As depicted in figure 1, the immense demand for refrigeration has emerged as a challenge that countries worldwide must confront [1]. In this context, how to reduce energy consumption and greenhouse gas emissions resulting from refrigeration has become a hot topic in global research, capturing the attention and efforts of numerous scholars and scientists.

Radiative cooling is considered a renewable cooling mechanism that has been put forth as a potential solution to counteract global warming. The fundamental principle of this approach involves minimizing solar absorption and augmenting the radiative heat transfer to outer space through the utilization of specific spectral attributes of engineered surfaces. By 400 BCE, the Persians had initiated the use of radiative cooling to manufacture ice during the sweltering summer nights [2]. In 1828, François Arago introduced the concept of radiative cooling [3]. The notion of passive day-time radiative cooling was first proposed by François Trombe in 1967 [4]. In 2014, researchers from Stanford achieved a milestone with the successful experimental demonstration of day-time sub-environmental radiative cooling [5]. In 2017, another team from University of Colorado, Boulder pioneered the kilometer-scale, high performance, and cost-effective production of daytime radiative cooling hybrid films [6]. These breakthroughs along with other advancements paved the way for a decade of vibrant growth in the realm of daytime radiative cooling, transitioning the field from theoretical propositions to a blossoming array of practical advancements.

Researchers have conducted extensive studies on the structure [5–10], fabrication processes [6, 9–11], and modulation mechanisms [12–14] of day-time radiative cooling materials, leading to the development of various radiative cooling structures, such as photonic crystals [7, 15], optical composite metamaterials [6, 16, 17], hierarchical porous polymers [9, 18–20], and radiative cooling wood [21]. Additionally, investigations into the integration of these devices with systems like building envelopes [22, 23], air conditioning [24], and solar cells [25–29] have been pursued. In the field of

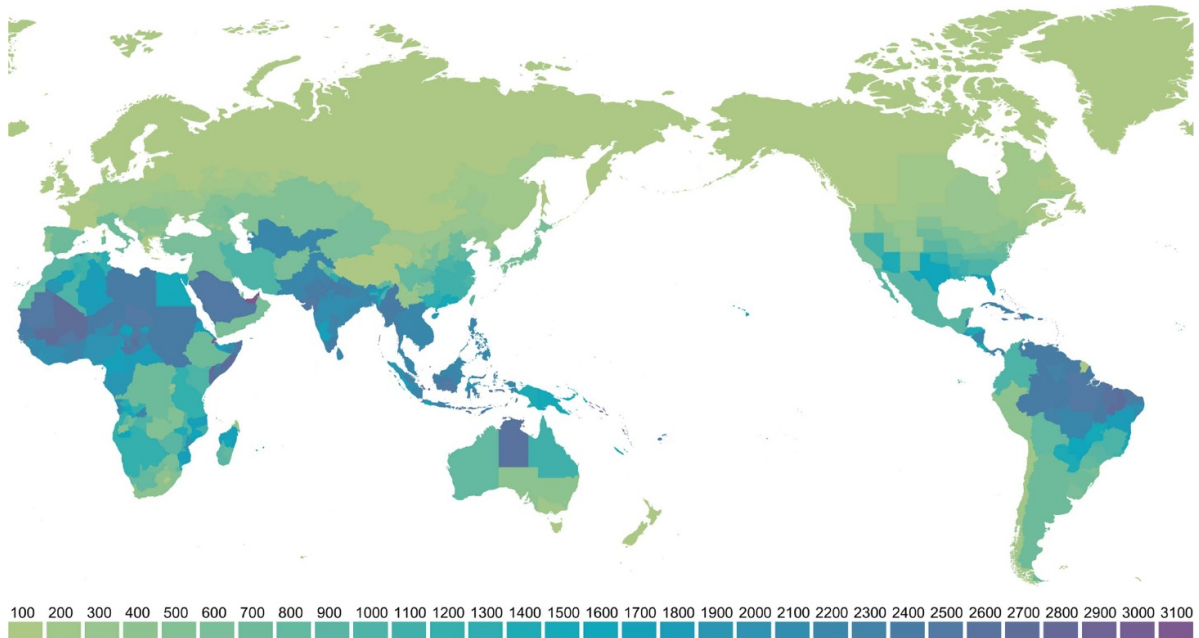


**Figure 1.** Global cooling demand: the world map of cooling degree days (CDDs) experienced across various regions during the year 2022.  $CDDs = \sum(T_m - T_b)^+$ , reflecting total cooling demand.  $T_m$  is daily mean temperature,  $T_b$  is baseline temperature. The '+' symbol indicates that CDDs increments only when  $T_m > T_b$ . The 2022 global CDDs map is based on data and methods open-sourced by Johnson *et al* [1].

dynamic thermal management, dynamic passive thermal control materials [30, 31], represented by hydrogels [32–34] and phase change materials [35–37], have garnered significant attention from researchers in radiative cooling, marking several milestone advancements.

To date, numerous groundbreaking works have emerged, progressively moving towards industrial application. Comprehensive literature reviews have thoroughly examined the fundamental principles [38–41], materials [39, 41, 42], influencing factors [43], applications [39–41, 44], and future prospects of radiative cooling [39–41, 44], offering invaluable insights and theoretical backing for the continued advancement of this field. However, in the realm of physical implementation pathways for passive daytime radiative cooling (PDRC) technology, there is a notable absence of systematic discourse, particularly concerning the selection of appropriate physical models tailored for specific application scenarios. This involves a comprehensive consideration of various physical factors and the identification of the optimal combination of structural configurations and material assemblies. Moreover, the application of efficient simulation techniques for the refined adjustment of design schemes poses a thought-provoking challenge.

Building upon previous research, this review first revisits the photonic and thermodynamic mechanisms underpinning radiative cooling, examining thermodynamic equilibrium within complex real-world scenarios. Subsequently, we articulate a theoretical framework for universal and scalable design strategies. The review then delves into the practical applications of PDRC materials across various industries, including energy-saving construction, personal thermal management (PTM), and photovoltaic (PV) cooling, as well as the

promising switchable PDRC materials designed to address the challenges of seasonal adaptability. In conclusion, the review assesses the current challenges faced by PDRC materials and anticipates future opportunities for their development. It is expected that this review will encapsulate the latest advancements in PDRC technology over the past few decades, injecting new momentum into research in the field and contributing to the realization of energy-saving and sustainable societies.

## 2. Fundamentals of radiative sky cooling

The mechanism behind radiative cooling is underpinned by Planck's law of blackbody radiation. In theory, all objects above absolute zero emit thermal radiation at a defined power, and high-temperature objects can be cooled through this process of thermal radiation. Interestingly, the atmospheric transmission window (ATSW) in the mid-infrared (MIR) spectrum (8–13  $\mu\text{m}$ ) aligns perfectly with the peak thermal radiation range for a blackbody at ambient temperatures (approximately 300 K). This alignment enables objects at room temperature to directly radiate heat into the cold expanse of space (approximately 3 K), potentially achieving temperatures lower than the surrounding environment through the process of radiative cooling.

### 2.1. Thermodynamic equilibrium of a solid surface emitter

To clarify the mechanism of radiation cooling, we examine a simple model of a solid surface emitter (figure 2(a)) with an area  $A$  and a temperature  $T$ , which is positioned with its normal vector directed towards the zenith to directly face the sky. The

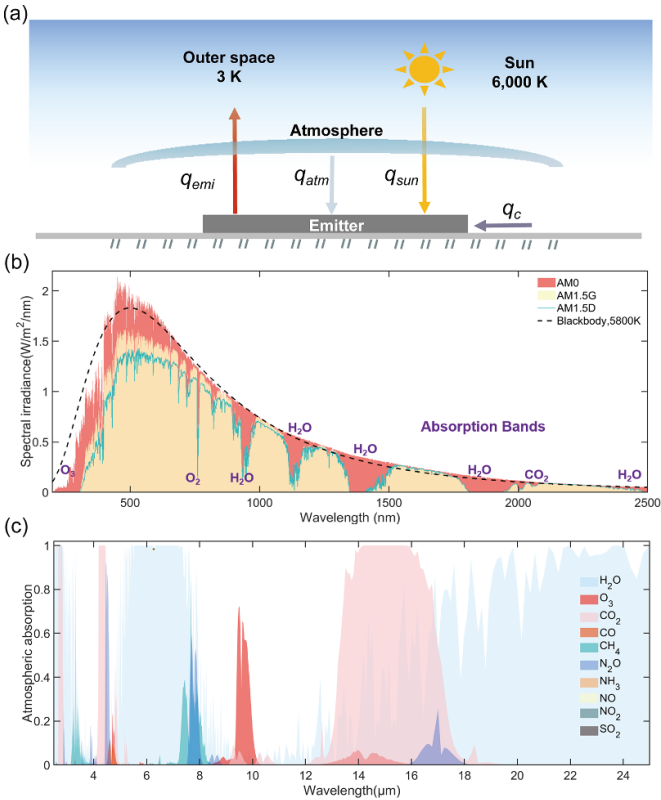


**Figure 2.** Daytime radiative cooling equilibrium and atmospheric spectra. (a) Thermodynamic equilibrium of daytime radiative cooling. (b) Solar spectra [45]. (c) Typical absorptance spectra of key constituents in the atmosphere [46, 47].

net cooling power of this emitter in an arbitrary environment characterized by a temperature  $T_{amb}$  can be articulated as:

$$q_{cool} = q_{emi}(T) - q_{sun} - q_{atm}(T_{amb}) - q_c. \quad (1)$$

This dynamic thermal equilibrium involves four key components: the emitter, the sun, outer space, and the ambient atmospheric conditions, as shown in figure 2(a). In this model,

**$q_{emi}$  denotes the thermal radiation heat flux spontaneously emitted by the emitter**, and can be calculated using the following equation:

$$q_{emi}(T) = \pi \int_0^{\infty} \int_0^{\frac{\pi}{2}} \varepsilon(\lambda, \theta) I_{BB}(\lambda, T) \sin(2\theta) d\theta d\lambda. \quad (2)$$

Here,  $\theta$  denotes the zenith angle, while  $\varepsilon(\lambda, \theta)$  represents the emissivity of the object at a specific wavelength  $\lambda$  and angle  $\theta$ . The spectral irradiance  $I_{BB}(\lambda, T)$  refers to the radiant energy emitted by a blackbody at temperature  $T$ , at the wavelength  $\lambda$ , ( $\text{W} \cdot \text{m}^{-2} \cdot \text{sr}^{-1} \cdot \mu\text{m}^{-1}$ ):

$$I_{BB}(\lambda, T) = \frac{2hc^2}{\lambda^5} \frac{1}{e^{hc/\lambda k_B T} - 1} \quad (3)$$

where  $h$  is the Planck's constant,  $c$  is the velocity of light,  $k_B$  is the Boltzmann constant.

**$q_{sun}$  refers to the solar radiation heat flux absorbed by the emitter.** In space, the radiation characteristics of the Sun closely mimic those of a perfect blackbody at a temperature of 5800 K, under which conditions we define the solar radiation as the AM 0 spectrum. However, as sunlight traverses the Earth's atmosphere and reaches the surface, it undergoes significant modifications due to the absorption and scattering effects of atmospheric molecules and particles, shifting the solar radiation spectrum from AM 0 to AM 1.5 (figure 2(b) [45]). Among the AM 1.5 spectra, AM 1.5D, which consists only of direct sunlight, is relatively constrained in practical applications since sunlight is seldom entirely direct. In contrast, AM 1.5 G encompasses both direct and scattered light, more accurately representing the actual solar radiation incident on the Earth's surface. Consequently, the AM 1.5 G spectrum is extensively used in radiative cooling and for evaluating the performance of PV systems. The influence of solar radiation is of paramount importance for solar-based radiative cooling. For instance, the solar radiation intensity corresponding to the AM1.5 G spectrum is standardized at  $1000 \text{ W m}^{-2}$ , which represents the unit intensity of sunlight. For an emitter with a solar absorption rate of 5%–10%, it would absorb 50–100  $\text{W m}^{-2}$  of solar energy, which is close to or potentially exceeds the cooling capacity limit of the emitter. The solar radiation absorbed by the emitter,  $q_{sun}$ , is typically expressed as follows:

$$q_{sun} = \cos\theta_{sun} \int_0^{+\infty} \varepsilon(\lambda, \theta_{sun}) I_{AM1.5G}(\lambda) d\lambda \quad (4)$$

$\theta_{sun}$  is the angle between the direction of the incident solar radiation and the normal direction of the emitter's surface.  $I_{AM1.5G}(\lambda)$  denotes the AM 1.5 G spectrum distribution of the solar radiation. Notably, the spectral radiative energy can be experimentally tested by solar spectroradiometer. Owing to the transparency of air in the 0.3–2.5  $\mu\text{m}$  wavelength range, a variety of mature detection methods based on different technical approaches [48, 49] can achieve rapid, efficient, and precise detection of the entire broad-range solar spectrum. The experimental method can validate the applicability of universal AM 1.5 G spectrum for local climate condition.

**$q_{atm}$  signifies the atmospheric radiative heat flux absorbed by the emitter.** The atmosphere consists of a complex mixture of various gases (such as water vapor and carbon dioxide, figure 2(c)), acting as a semi-transparent emitter that attenuates thermal radiation emitted from the Earth's surface towards outer space. Due to the combined effects of different gas constituents and sky temperatures, the sky radiation is predominantly focused in the infrared spectrum. However, within the atmospheric window (primarily 8–13  $\mu\text{m}$ , with parts in the 3–5  $\mu\text{m}$  [50] and 16–23  $\mu\text{m}$  [40] ranges), the sky atmosphere is highly transparent, constituting a critical channel for radiative cooling. In accordance with the principles of thermal radiation, the infrared radiation emitted from the sky and absorbed by an emitter can be expressed as:

$$q_{\text{atm}}(T_{\text{amb}}) = \pi \int_0^{+\infty} \int_0^{\frac{\pi}{2}} \varepsilon(\lambda, \theta) \varepsilon_{\text{atm}}(\lambda, \theta) I_{\text{BB}} \times (\lambda, T_{\text{amb}}) \sin(2\theta) d\theta d\lambda. \quad (5)$$

Here, the emissivity of the atmosphere is  $\varepsilon_{\text{atm}}(\lambda, \theta)$ , which is closely related to environmental and meteorological conditions. A detailed discussion of the atmospheric emissivity will be provided in section 2.2.1.

$q_c$  characterizes the non-radiative heat flux, which is the heat exchange between the emitter and the surrounding environment through thermal conduction and convection. Convection and conduction are consistently considered the primary mechanisms of cooling loss. When the operating temperature of an emitter exceeds the ambient temperature, the emitter's cooling loss power becomes negative, signifying an increase in the overall cooling capacity during this process. Conversely, for sub-ambient radiative cooling, this cooling loss process has a detrimental effect on the minimum temperature that can potentially be achieved.

The mathematical description of the non-radiative heat flux of the emitter,  $q_c$ , can be expressed as

$$q_c = h_c(T_{\text{amb}} - T) \quad (6)$$

where,  $h_c$  represents a combined non-radiative heat transfer coefficient, commonly ranging from 5–20 W (m<sup>2</sup>.K)<sup>-1</sup> in outdoor scenarios [24, 51], which characterizes the conductive and convective heat exchange ( $h_{\text{cond}}$ ,  $h_{\text{conv}}$ ):

$$h_c = h_{\text{cond}} + h_{\text{conv}}. \quad (7)$$

A detailed discussion of  $h_c$  will be provided in section 2.2.2.

## 2.2. Environmental impact on the efficacy of radiative cooling

In contrast to active cooling devices such as air conditioners and fans, radiative cooling-based devices operate passively, boasting the significant advantage of zero energy consumption. Essentially, the cold source for radiative cooling devices is the vast expanse of outer space, with the interaction facilitated through the Earth's atmospheric medium. Consequently, the influence of environmental parameters on the effectiveness of radiative cooling is of paramount importance. Notably, the atmospheric radiative heat flux  $q_{\text{atm}}$  and the non-radiative heat flux  $q_c$  are the two key parameters primarily influenced by environmental factors.

**2.2.1. Atmospheric transparency spectrum shaping.** The atmospheric radiative heat flux  $q_{\text{atm}}$  is modulated by changes in atmospheric emissivity  $\varepsilon_{\text{atm}}(\lambda, \theta)$ , which in turn is influenced by a suite of environmental factors such as the zenith angle, air humidity, cloud cover, aerosol, latitude, day-night effect, and seasonal effect. Figure 4(a) provides the calculated transmittance  $\tau_{\text{atm}}(\lambda, \theta)$  of aerosol-free and cloud-free atmosphere from the ground to space under different humidities.

Under clear or cloudy sky conditions, the atmospheric spectral emissivity can be determined using several computational tools as presented in table 1. Given the complex effects of different gases on the radiative properties of the sky atmosphere and the challenges in calculating this within theoretical models, these formulas all have their limitations. Under clear sky conditions, in theoretical calculations, the most commonly employed empirical formula is expressed as follows:

$$\varepsilon_{\text{atm}}(\lambda, \theta) = 1 - \tau_{\text{atm}}(\lambda, 0)^{1/\cos\theta} \quad (8)$$

with  $\tau_{\text{atm}}(\lambda, 0)$  being the transmission coefficient of the atmosphere in the zenith direction.

The effect of cloud cover has very complicated impacts on the atmospheric radiation due to the different types (e.g. cirrus, stratus), altitudes, thickness, constitution, droplet size distribution of clouds. It is also important to consider observation angle from the radiative cooling surface, and the constantly changing of cloud behaviors over time and space. Since the major composition of clouds is condensate water droplets and ice crystals that have an average emissivity of 0.92–0.98, the emissivity of thick clouds may be considered as 1 over the whole infrared spectrum, including the atmospheric window [75].

Ignoring other factors such as cloud height, cloud thickness, and the observation angle from the radiative cooling surface, the cloud cover fraction,  $f_{\text{cc}}$ , is the sole consideration. Thus, in cloudy conditions, the environmental radiation absorbed by the emitter,  $q_{\text{atm,cloud}}$ , is corrected to

$$q_{\text{atm,cloud}}(T_{\text{amb}}) = (1 - f_{\text{cc}}) \cdot q_{\text{atm}} + f_{\text{cc}} \cdot q_{\text{cloud}}. \quad (9)$$

Due to the assumed emissivity of thick clouds (black body) as 1, the clouds thermal radiation absorbed by the emitter can be represented as

$$q_{\text{cloud}}(T_{\text{amb}}) = \pi \int_0^{+\infty} \int_0^{\frac{\pi}{2}} \varepsilon(\lambda, \theta) I_{\text{BB}}(\lambda, T_{\text{amb}}) \sin(2\theta) d\theta d\lambda. \quad (10)$$

Figure 3(b) illustrates the increasing relationship between atmospheric radiative heat flux and the augmentation of cloud cover.

Environmental factors such as ambient temperature, humidity, cloud cover, gas composition, and suspended dust particles have a direct influence on atmospheric radiation. Moreover, changes in altitude can affect all these variables, making it an indispensable consideration when discussing atmospheric radiation.

The troposphere, where human activities predominantly occur, is the lowest layer of Earth's atmosphere, extending approximately 10–15 kilometers in thickness. The temperature profile of the troposphere is primarily influenced by the terrestrial radiation and atmospheric backradiation. As altitude increases, the absorption of terrestrial radiation decreases, and the insulating effect of the air becomes less pronounced due

**Table 1.** List of correlations that estimate the effective atmospheric emissivity.

Correlation	Validity conditions	Year	Sky	Reference
$\varepsilon_{\text{atm}} = c_1 + c_2 \cdot P_{\text{W}}^{1/2}$	Region dependent	1932	Clear	Brunt [52]
$\varepsilon_{\text{atm}} = c_1 - c_2 \cdot 10^{c_3 \cdot P_{\text{W}}}$	Region dependent	1936	Clear	Angstrom [53]
$\varepsilon_{\text{atm}} = 0.8004 + 0.00396 T_{\text{dp}}$		1961	Clear	Bliss [54]
$\varepsilon_{\text{atm}} = 1 - 0.261 e^{-0.00077(273.15 - T_{\text{amb}})^2}$	For Arizona and Alaska	1969	Clear	Idso <i>et al</i> [55]
$\varepsilon_{\text{atm}} = 0.67 \cdot e^{0.08}$	$0.2 < P_{\text{W}} < 20 \text{ mbar}$	1972	Clear	Staley <i>et al</i> [56]
$\varepsilon_{\text{atm}} = 0.1 + 3.53 \times 10^{-8} \cdot P_{\text{W}}^2 \cdot e^{(3000/T_{\text{amb}})}$	10.5–12.5 $\mu\text{m}$	1981	Clear	Idso [57]
$\varepsilon_{\text{atm}} = 0.24 + 2.98 \times 10^{-8} \cdot P_{\text{W}}^2 \cdot e^{(3000/T_{\text{amb}})}$	8–14 $\mu\text{m}$	1981	Clear	Idso [57]
$\varepsilon_{\text{atm}}(\lambda, \theta) = 1 - [1 - \varepsilon_{\text{atm}}(\lambda, 0)]^{1/\cos\theta}$	For Antarctic and Arctic	1982	Clear	Granqvist and Hjortsberg [58] Andreas and Ackley [59]
$\varepsilon_{\text{atm}} = [5.7723 + 0.9555 \times (0.6017)^Z] \times T_{\text{amb}}^{1.893} RH^{0.0665} \times 10^{-4}$	Nighttime, altitude dependent	1982	Clear	Centeno [60]
$\varepsilon_{\text{atm}} = 0.741 + 0.0062(T_{\text{dp}} - 273.15)$	Nighttime	1982	Clear	Berdahl and Fromberg [61]
$\varepsilon_{\text{atm}} = 0.727 + 0.0060(T_{\text{dp}} - 273.15)$	Daytime	1982	Clear	Berdahl and Fromberg [61]
$\varepsilon_{\text{atm}} =$	D is a constant related to altitude	1982	Cloudy	Centeno [60]
$\varepsilon_{\text{atm,clear}} + 10 \times f_{\text{cc}} [1/(D/T_{\text{amb}})^4 - \varepsilon_{\text{atm,clear}}]$				
$\varepsilon_{\text{atm}}(\theta) = 1$	$\lambda < 8 \mu\text{m}$ , $\lambda > 13 \mu\text{m}$	1982	Clear	Lushiku <i>et al</i> [62]
$\varepsilon_{\text{atm}}(\lambda, \theta) = 1 - (1 - \varepsilon_{\text{average}})[\tau_{\text{atm}}(\lambda, \theta)/\tau_{\text{average}}]e^{1.7b-b/\cos\theta}$ .	b is a constant related to region	1983	Clear	Berdahl <i>et al</i> [63]
$\varepsilon_{\text{atm}}(\theta) = 1 - [1 - \varepsilon_{\text{atm}}(0)]^{1/\cos\theta}$	8–13 $\mu\text{m}$	1984	Clear	Lushiku and Granqvist [64]
$\varepsilon_{\text{atm}} =$	Nighttime, altitude dependent	1984	Clear	Martin and Berdahl [65]
$0.711 + 0.56(T_{\text{dp}}/100) + 0.73(T_{\text{dp}}/100)^2 + 0.013\cos(2\pi t/24) + 0.00012(P_{\text{atm}} - 1000)$				
$\varepsilon_{\text{atm}} = 0.770 + 0.0038T_{\text{dp}}$	Nighttime	1984	Clear	Berger <i>et al</i> [66]
$\varepsilon_{\text{atm}} = \varepsilon_{\text{atm,clear}} + (1 - \varepsilon_{\text{atm,clear}})f_{\text{cc}}$		1984	Cloudy	Martin and Berdahl [65]
$\varepsilon_{\text{atm}} = \varepsilon_{\text{atm,clear}} [1 + 0.496 \cdot (10 \times f_{\text{cc}})^{2.45}]$	For Kansas	1993	Cloudy	Sugita and Berdahl [67]
$\varepsilon_{\text{atm}} =$	For Bennington, Nebraska	1995	Clear or Cloudy	Chen <i>et al</i> [68]
$0.736 + 0.00571T_{\text{dp}} + 3.3318 \times 10^{-6}T_{\text{dp}}^2$		1998	Clear	Dilley and O'Brien [69]
$\varepsilon_{\text{atm}} = -e^{-1.66[2.32 - 1.875(T_{\text{amb}}/273.15) + 0.735(\text{PWV}/25)^{1/2}]}$				
$\varepsilon_{\text{atm}} = f_{\text{cc}} + (1 - f_{\text{cc}})\varepsilon_{\text{atm,clear}}$		1999	Cloudy	Crawford and Duchon [70]
$\varepsilon_{\text{atm}} = 0.72 + 0.009 \cdot (P_{\text{W}} - 2)$	$P_{\text{W}} \geq 2$	2001	Clear	Niemelä <i>et al</i> [71]
$\varepsilon_{\text{atm}} = 0.72 + 0.076 \cdot (P_{\text{W}} - 2)$	$P_{\text{W}} < 2$	2001	Clear	Niemelä <i>et al</i> [71]
$\varepsilon_{\text{atm}} = 0.754 + 0.0044T_{\text{dp}}$	Night time, for Negev highlands, Israel	2004	Clear	Tang <i>et al</i> [72]
$\varepsilon_{\text{atm}} = 1.18(P_{\text{W}}/T_{\text{amb}})^{1/7}$	For Andean Altiplano, Bolivia	2007	Clear	Lhomme <i>et al</i> [73]
$\varepsilon_{\text{atm}} = \varepsilon_{\text{atm,clear}} \left[ 1.37 - 0.34 \left( \frac{P_{\text{sun,real}}}{P_{\text{sun,cloud}}} \right) \right]$	For Andean Altiplano, Bolivia	2007	Cloudy	Lhomme <i>et al</i> [73]
$\varepsilon_{\text{atm}} = C(P_{\text{W}}/T_{\text{amb}}) \left[ 1.67 - 0.83 \left( \frac{P_{\text{shortwave}}}{P_{\text{extra}}} \right) \right]$	For Zongo, Bolivia	2010	Cloudy	Sicart <i>et al</i> [74]
$\varepsilon_{\text{atm}}(\lambda, \theta) = 1 - \tau_{\text{atm}}(\lambda, 0)^{1/\cos\theta}$		2014	Clear	Raman <i>et al</i> [5]

Note:  $T_{\text{dp}}$  represents the dewpoint temperature (K);  $T_{\text{amb}}$  denotes the ambient temperature (K);  $P_{\text{W}}$  refers to the partial water vapor pressure (mbar);  $Z$  is the altitude (m);  $P_{\text{atm}}$  is the atmospheric pressure (hPa);  $RH$  is the relative humidity (%);  $t$  is the solar time; and  $\text{PWV}$  is the precipitable water content (mm).

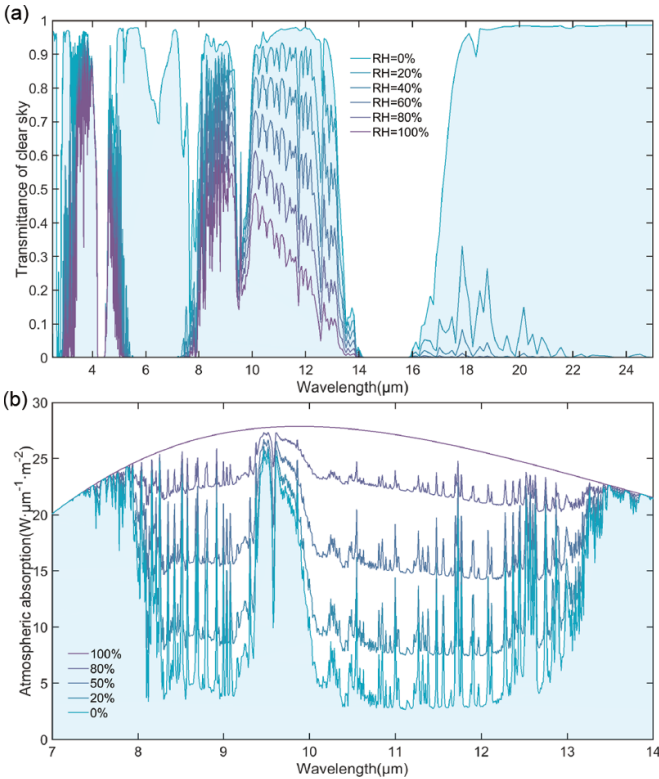


**Figure 3.** Influencing factors of atmospheric radiation. (a) Transmittance of the aerosol-free and cloud-free atmosphere with different ambient  $RH$  levels and  $T_{\text{amb}} = 300$  K in the zenith direction. The atmospheric transmittance is obtained from MODTRAN6 [47]. (b) Atmospheric radiation heat flux,  $q_{\text{atm},\text{cloud}}$ , under varying cloud cover fractions,  $f_{\text{cc}}$ , at  $T_{\text{amb}} = 300$  K and  $RH = 20\%$ .

to its decreasing density. Consequently, a vertical temperature gradient occurs, as depicted by the following formula:

$$T_{\text{amb}}(Z) = T_{\text{amb}}(Z_0) - R_{\text{TL}} \cdot Z - Z_0 \quad (11)$$

$Z$  is altitude, while  $R_{\text{TL}}$  signifies the temperature lapse rate (TLR). The TLR is influenced by various factors, such as latitude, season, and weather systems. Typically, an empirical value of  $0.0065^{\circ}\text{C m}^{-1}$  is adopted [79]. In other words, for every 1 km increase in altitude, the temperature decreases by  $6.5^{\circ}\text{C}$  (black line in figure 4). At lower environmental temperatures, the atmospheric radiation power is reduced, which is conducive to the effect of radiative cooling.

As altitude increases, the air becomes less dense, leading to a decrease in the number of molecules per unit volume of gases that can absorb infrared radiation, such as water vapor ( $\text{H}_2\text{O}$ ), carbon dioxide ( $\text{CO}_2$ ), and nitrous oxide ( $\text{N}_2\text{O}$ ) as depicted in figure 2(c). This results in an increase in atmospheric transparency.

As depicted in figure 2(c), among the various gas components, water vapor is a primary contributor to atmospheric re-emission. The decrease in its density with increasing altitude is a consequence of reduced atmospheric pressure, lower temperatures, diminished sources of water vapor, and the effects of

precipitation, which have all been collectively investigated and statistically validated. The density of water vapor ( $\rho_{\text{wv}}$ ) can be approximated as an exponential function of altitude [76].

$$\rho_{\text{wv}}(Z) = \rho_{\text{wv},0} \cdot \exp\left(\frac{Z_0 - Z}{H}\right) \quad (12)$$

where  $\rho_{\text{wv},0}$  denotes the water vapor density near the ground level  $Z_0$ , and  $H$  represents the water vapor scale height, whose value is dependent on the local environmental and climatic conditions. Generally, an empirical value of 2000 m is adopted for  $H$  [78].

The water vapor density at ground level is correlated with the ambient relative humidity ( $RH$ ). Based on the ideal gas law and the Clausius–Clapeyron equation [77], it can be expressed as follows:

$$\rho_{\text{wv},0} = P_{\text{wv},0} \cdot \frac{M_{\text{H}_2\text{O}}}{R \cdot T_{\text{amb}}} \quad (13)$$

$$P_{\text{wv},0} = 611 \cdot RH \cdot \exp\left(\frac{L_v}{R_v} \left(\frac{1}{273.15} - \frac{1}{T_{\text{amb}}}\right)\right) \quad (14)$$

$P_{\text{wv},0}$  denotes the water vapor pressure,  $M_{\text{H}_2\text{O}}$  is the molar mass of water ( $18 \text{ g mol}^{-1}$ ),  $R$  is the universal gas constant ( $8.31 \text{ J mol}^{-1} \text{ K}^{-1}$ ),  $L_v$  is the latent heat of evaporation (approximately  $2.435 \times 10^6 \text{ J kg}^{-1}$  at 300 K), and  $R_v$  is the gas constant for water vapor ( $4.615 \times 10^2 \text{ J kg}^{-1} \text{ K}^{-1}$ ), respectively.

As indicated by the orange line in figure 4, the absolute humidity decreases exponentially with altitude. Compared to the ground level, it is reduced by half at an altitude of 1.3 km and drops to approximately 10% at around 4 km. As depicted in figure 3(a), the lower humidity significantly enhances the transparency of the atmospheric window.

Throughout the troposphere, a wide distribution of various cloud types is observed (figure 4). At higher altitudes, the cloud layers become increasingly thinner. As illustrated in figure 3(b), a lower cloud cover results in reduced atmospheric radiation, which is conducive to radiative cooling.

In this subsection, we have discussed in detail the impact of environmental factors on atmospheric radiation. It can be concluded that lower temperatures, reduced humidity, and decreased cloud cover all contribute to lower atmospheric radiation, thereby facilitating radiative cooling. Moreover, an increase in altitude simultaneously leads to lower temperatures, reduced humidity, and less cloud cover, which collectively enhance the potential for radiative cooling.

### 2.2.2. Estimation of non-radiative heat transfer coefficients.

Environmental factors not only shape the atmospheric window but also play a pivotal role in modulating the non-radiative heat transfer coefficient  $h_c$  through the influence of spatial scales and wind speeds. This, in turn, profoundly affects the non-radiative heat flux  $q_c$ , ultimately determining the cooling performance of radiative cooling devices. Hence, it is essential to accurately quantify the non-radiative heat transfer coefficient  $h_c (\text{W} (\text{m}^2 \cdot \text{K})^{-1})$ .

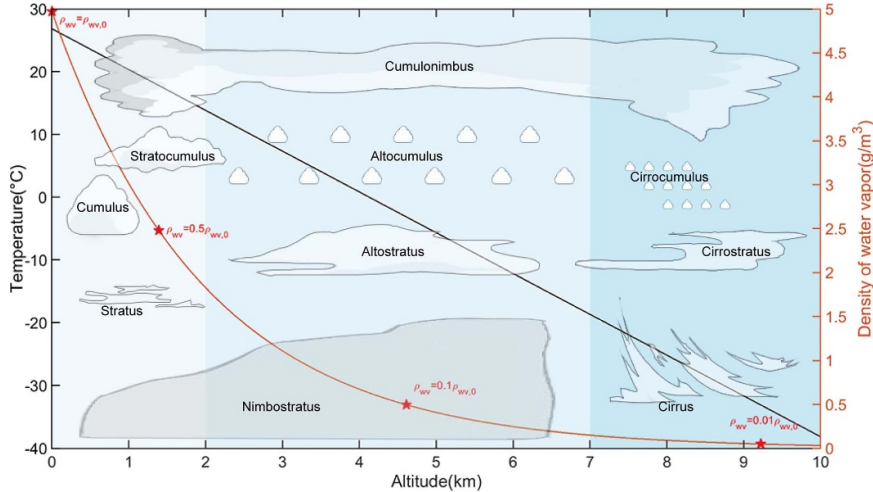


**Figure 4.** The influence of altitude on atmospheric radiation. The temperature and humidity decrease with increasing altitude [76, 77]. Under the assumed environmental conditions at sea level (altitude = 0), the ambient temperature  $T_{\text{amb}}$  is set to 300 K, the relative humidity  $RH$  is 20%, the water vapor scale height  $H$  is 2000 m [78], and the temperature lapse rate (TLR)  $\alpha$  is  $0.0065 \text{ }^{\circ}\text{C m}^{-1}$  [79]. The background image illustrates the distribution of various cloud types at different elevations.

Within confined spaces,  $h_c$  is related to the Nusselt number,  $N_u$ , and the Rayleigh number,  $R_a$ .

The Nusselt number  $N_u$  represents the ratio of convective heat transfer within the fluid boundary layer to the conductive heat transfer across that layer. It is defined as follows:

$$N_u = \frac{h_c L}{k} \quad (15)$$

$L$  represents the characteristic length (m), such as the height of an enclosed room or the diameter of a pipe.  $k$  is the thermal conductivity of the fluid ( $\text{W} (\text{m K})^{-1}$ ), with air having a value of approximately 0.026.

The Rayleigh number,  $R_a$ , is a dimensionless quantity that characterizes the ratio of the driving force for natural convection flow to the resistive force of viscosity. It is defined as follows:

$$R_a = \frac{g \beta (T_s - T_f) L^3}{\nu \alpha}. \quad (16)$$

The gravitational acceleration is denoted as  $g=9.81 \text{ m s}^{-2}$ . The volumetric expansion coefficient of air is  $\beta=3 \times 10^{-3} \text{ K}^{-1}$ .  $T_s$  and  $T_f$  represent the temperatures at the solid surface and in the fluid, respectively. At ambient conditions, the kinematic viscosity of air is  $\nu = 1.5 \times 10^{-5} \text{ m}^2 \text{ s}^{-1}$ , and its thermal diffusivity is  $\alpha = 1.5 \times 10^{-5} \text{ m}^2 \text{ s}^{-1}$ .

The relationship for calculating the Nusselt number  $N_u$  in relation to the Rayleigh number  $R_a$  is provided by [80]:

$$N_u = \frac{2}{\pi} \left[ \left( 1 - \frac{1}{\sqrt{8}} \right)^{\frac{1}{2}} + \left( \frac{(2/\pi)^{1/3}}{4} R_a^{1/3} \right)^{\frac{1}{2}} \right]^2. \quad (17)$$

For instance, in the context of a typical indoor environment, where the room height serves as the characteristic

length  $L=3 \text{ m}$ , under the condition of a minor temperature fluctuation ( $T_s - T_f = \pm 0.1 \text{ }^{\circ}\text{C}$ ) within the room, the computed convective heat transfer coefficient  $h_c$  is approximately  $0.96 \text{ W} (\text{m}^2 \text{ K})^{-1}$ , which aligns with the value of  $h_c = 1 \text{ W m}^{-2} \cdot \text{K}$  reported in [81].

In an open environment, the convective heat transfer coefficient is significantly influenced by wind speed  $V_{\text{wind}} (\text{m s}^{-1})$ . An empirical formulation capturing this relationship is presented as follows:

$$h_c = h_0 + b \cdot V_{\text{wind}}. \quad (18)$$

In the equation presented,  $h_0$  and  $b$  are constants that are closely tied to environmental factors and the specifics of the experimental setup. For instance, under the experimental conditions for a solar cell with a surface area of  $0.58 \text{ m} \times 0.58 \text{ m}$ , and without a PE shield, Zhao *et al* have derived a fitting equation of  $h_c = 8.3 + 2.5 \cdot V_{\text{wind}}$  [24]. Conversely, when the solar cell is equipped with a PE shield, the fitting equation shifts to  $h_c = 2.5 + 2.0 \cdot V_{\text{wind}}$  [24].

### 2.3. Performance analysis based on spectral and spatial characteristics

Beyond the extrinsic impact of the previously mentioned environmental factors, it is the spectral characteristics intrinsic to radiative cooling devices that are pivotal to their cooling capacity. In pursuit of maximizing cooling performance or achieving the lowest possible cooling temperature, the precise tuning of the emitter's spectral bands and emission angles has become a recent research focal point. In this context, it is imperative to quantitatively and thoroughly investigate the theoretical implications of spectral and spatial characteristics on radiative cooling.

**2.3.1. Performance of emitters with multiband emissivity modulation.** As shown in figure 5(a), under ambient temperature conditions, the thermal radiation emitted by objects overlaps with atmospheric radiation in the spectrum. Therefore, the spectral design of an emitter is essential to either enhance its thermal radiation or minimize the absorption of radiation from the atmosphere. Based on the spectral band design, emitters are typically categorized into two types: selective emitters and broadband emitters. A selective emitter exhibits unity emissivity within the wavelength range of 8–13  $\mu\text{m}$  (the atmospheric transparency window at room temperature), with no absorption in other wavelengths. In contrast, a broadband emitter (also known as a blackbody emitter) exhibits 100% emissivity across wavelengths longer than 2.5  $\mu\text{m}$ , with zero absorption in the solar spectrum. In addition to the well-known 8–13  $\mu\text{m}$  atmospheric transparency window, the 3–5  $\mu\text{m}$  and 16–23  $\mu\text{m}$  ranges are also recognized as typical atmospheric transparency windows. However, the latter is often subject to lower transmittance due to humidity (as shown in figure 3(a)), at 20% relative humidity, the atmospheric transmittance in the 16–23  $\mu\text{m}$  range is significantly reduced), and it is generally negligible. For these multiple atmospheric windows, we hypothesize two types of emitters: the dual-window emitter exhibits unity emissivity at the 3–5  $\mu\text{m}$  and 8–13  $\mu\text{m}$  atmospheric transparency windows, with zero emissivity at other wavelengths; the multi-window emitter, on the other hand, exhibits unity emissivity at the 3–5  $\mu\text{m}$ , 8–13  $\mu\text{m}$ , and 16–23  $\mu\text{m}$  atmospheric transparency windows, with zero emissivity at all other wavelengths.

Figure 5(b) depicts the net cooling flux as a function of temperature for emitters with various infrared spectral characteristics. The lowest achievable temperature corresponds to the point where the net cooling flux is zero, which is strongly influenced by non-radiative heat exchange. The net cooling flux is the intersection where the cooler temperature equals the ambient temperature; in this scenario, the emitter does not exchange heat non-radiatively with the ambient.

From the cooling flux-temperature plot, it is evident that a selective emitter can achieve a lower temperature, whereas a blackbody cooler exhibits a stronger net cooling flux under the same conditions. It is noteworthy that the net cooling flux of a blackbody emitter is also higher than that of a selective emitter under ambient temperature conditions, due to the radiation emitted by the blackbody emitter in the two other atmospheric windows (i.e. 3–5  $\mu\text{m}$  and 16–23  $\mu\text{m}$ ).

For dual-window emitters, the blackbody radiation spectrum at 30 °C exhibits a relatively lower energy distribution within the 3–5  $\mu\text{m}$  spectral band, leading to a cooling performance that is akin to that of selective emitters operating exclusively within the 8–13 micrometer atmospheric window. In arid conditions, the multi-window emitter demonstrates a more pronounced cooling potential across a wider temperature range, although its cooling performance is susceptible to humidity. In humid environments, its spectral performance converges towards that of a blackbody emitter (figure 3(a)). Consequently, researchers typically concentrate on the study of selective emitters and blackbody emitters under

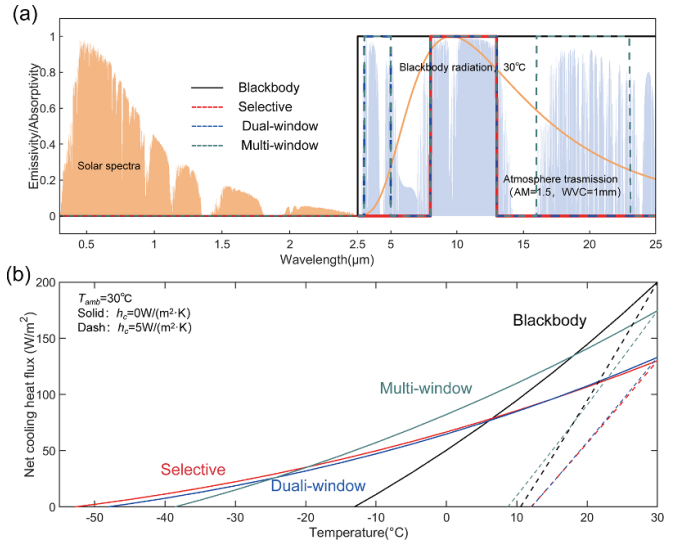


**Figure 5.** Theoretical elucidation of the cooling performance under spectral band-modulated daytime radiative cooling. (a) The solar spectrum is depicted with an orange shaded area, contrasted with the atmospheric transmission spectrum in the infrared wavelength range, shown as the light purple shaded area. The atmospheric transparency window corresponds to a clear sky under conditions of an air mass of 1.5 and a water vapor column of 1 millimeter, as reported by the Gemini Observatory [82] (available from: <http://www.gemini.edu/sciops/telescopes-and-sites/observing-condition-constraints/ir-transmission-spectra>). The atmospheric transparency window at 8–13  $\mu\text{m}$  exhibits significant spectral overlap with the blackbody radiation spectrum at room temperature, approximately 30 °C (orange solid curve). A blackbody emitter is depicted with an emissivity of 100% at wavelengths greater than 2.5  $\mu\text{m}$  and 0% at other wavelengths (black solid curve), a selective emitter is depicted with an emissivity of 100% at 8–13  $\mu\text{m}$  and 0% at other wavelengths (red dashed curve), a dual-window emitter is depicted with an emissivity of 100% at both the 3–5  $\mu\text{m}$  and 8–13  $\mu\text{m}$  atmospheric windows and 0% at other wavelengths (blue dashed line), and a multi-window emitter is depicted with an emissivity of 100% at the 3–5  $\mu\text{m}$ , 8–13  $\mu\text{m}$ , and 16–23  $\mu\text{m}$  atmospheric windows and 0% at other wavelengths (dark green dashed line). (b) Net cooling heat flux  $q_{\text{cool}}$  of the temperature  $T$  of the radiative cooler under various infrared emissivity profiles ( $\varepsilon(\lambda)$ ), including the blackbody emitter (black solid curve), the 8–13  $\mu\text{m}$  selective emitter (red dashed curve), the dual-window emitter that operates at both 3–5  $\mu\text{m}$  and 8–13  $\mu\text{m}$  (blue dashed curve) and the multi-window emitter that operates at 3–5  $\mu\text{m}$ , 8–13  $\mu\text{m}$  and 16–23  $\mu\text{m}$  (dark green dashed curve).

room temperature conditions, unless there are specific cooling environment requirements, such as the need for 3–5  $\mu\text{m}$  atmospheric windows for cooling high-temperature objects at 300 °C [83], or the suitability of multi-window emitters in arid desert environments [84]. For instance, in 2024, the research group led by Zhang at Tsinghua University designed and fabricated a dual-selective (Dual-selective) thermal emitter [84] that can simultaneously utilize two ATSWs (8–13  $\mu\text{m}$  and 16–23  $\mu\text{m}$ ) for cooling purposes, serving as a high-performance radiative cooling material. They demonstrated that this material exhibits superior sub-ambient cooling performance compared to existing typical radiative cooling emitters under arid and hot climate conditions. In addition to radiation cooling, the

significance of various atmospheric windows in other fields cannot be overlooked. As previously mentioned, the common surface temperature of high-speed aircraft (approximately 300 °C) corresponds to the 3–5 μm atmospheric window, within which precise infrared optical detection [48, 49] is crucial in fields such as environmental mapping, aerospace, and military applications. Concurrently, infrared camouflage research [85–88] also focuses on these atmospheric windows. For instance, Guo *et al* proposed a tunable infrared emitter composed of ZnS/Ge/Ag/Ge<sub>2</sub>Sb<sub>2</sub>Te<sub>5</sub>/Ag films based on phase-change materials [85], which can achieve MIR camouflage, radiation heat dissipation, and long-wavelength-infrared (LWIR) camouflage in wavelength ranges of 3–5 μm, 5–8 μm, and 8–14 μm, respectively.

In an ideal vacuum environment,  $h_c = 0$ , a blackbody emitter is capable of achieving a substantial temperature reduction of over 40 °C, while a selective emitter can elevate this to 60 °C, as depicted by the solid curve in figure 5(b). However, in real-world applications, the inevitable thermal losses attributed to non-radiative heat transfer cannot be dismissed. Even a modest non-radiative heat transfer coefficient of  $h = 5 \text{ W} (\text{m}^2 \text{ K})^{-1}$  can diminish the anticipated temperature reduction to merely 20 °C, as shown by the dashed curve in figure 5(b).

In addition, the concept of a perfect blackbody with 100% emissivity in the infrared spectrum and a perfect whitebody with 100% reflectivity in the solar spectrum is purely theoretical; a spectral performance of 95% is already considered exceptionally good. The deviation from these ideal spectral characteristics can result in a 5% reduction of the net radiative heat flux for cooling (approximately 10 W m<sup>-2</sup>) and a 5% increase in solar radiation heating (approximately 50 W m<sup>-2</sup>). Consequently, when accounting for both spectral performance and the impact of non-radiative heat transfer, a diurnal temperature decrease exceeding 15 °C in empirical testing is deemed a remarkably impressive achievement.

### 2.3.2. Performance of emitters with angular emissivity modulation.

Moreover, in light of the wavelength and angular dependencies of a given atmospheric transmission spectrum, we can refine the optimization of  $\varepsilon(\lambda, \theta)$  for each angle and wavelength to aspire to the optimal cooling efficacy.

Distinct from solid surface emitters, which can be modeled as Lambertian radiators, the atmospheric emissivity varies with observation angle, with a relative increase at larger zenith angles (see equation (8)). By meticulously tailoring the emissivity function  $\varepsilon(\lambda, \theta)$  (first row in figure 6(b)), we can effectively screen out the radiative heat exchange channels where atmospheric radiation surpasses that of the emitter, theoretically yielding an optimal ideal emitter. Under the assumption of perfect thermal insulation, this emitter can achieve an equilibrium temperature difference of  $T - T_{\text{amb}} \leq 150 \text{ }^{\circ}\text{C}$  (solid blue line in figure 6(a)).

The optimization of an ideal emitter necessitates precise adjustments at each angle and wavelength, a process

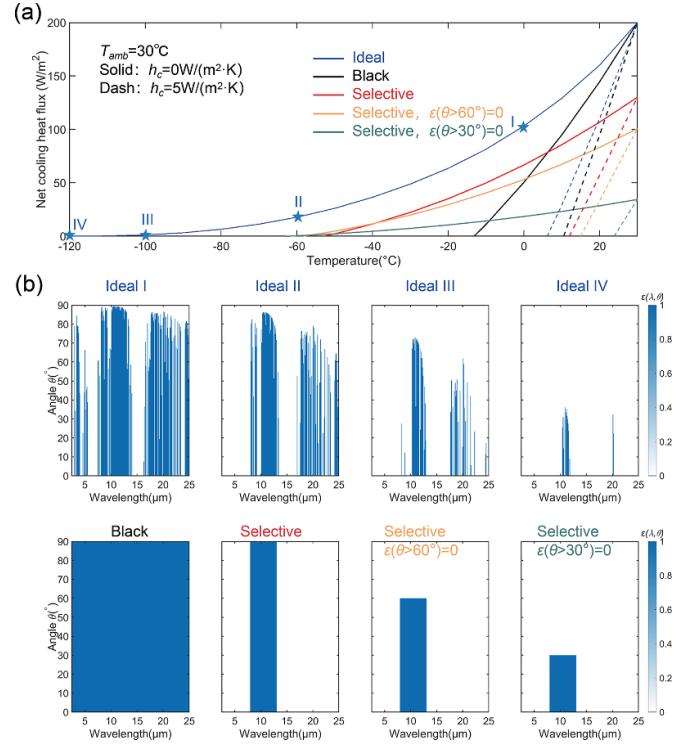


**Figure 6.** Theoretical investigation into the performance of daytime radiative cooling modulated by spectral angular characteristics. (a) Net cooling heat flux  $q_{\text{cool}}$  of the temperature  $T$  of the radiative cooler under various infrared emissivity profiles  $\varepsilon(\lambda, \theta)$ , including the ideal spectral-angular-selective emitter (blue curve), the blackbody emitter (black curve), the 8–13 μm selective emitter (red curve), the 8–13 μm selective emitter with  $\varepsilon(\theta > 60^\circ) = 0$  (yellow curve), and the 8–13 μm selective emitter with  $\varepsilon(\theta > 30^\circ) = 0$  (dark green curve). (b) The emissivity profiles  $\varepsilon(\lambda, \theta)$  of the radiative cooler in (a). The atmospheric transparency window corresponds to a clear sky under conditions of an air mass of 1.5 and a water vapor column of 1 mm, as reported by the Gemini Observatory [82] (available from: [www.gemini.edu/sciops/telescopes-and-sites/observing-condition-constraints/ir-transmission-spectra](http://www.gemini.edu/sciops/telescopes-and-sites/observing-condition-constraints/ir-transmission-spectra)).

that, while theoretically feasible and achievable in a laboratory setting for optimized coolers, presents significant challenges for large-scale production and widespread application. Moreover, the dynamic nature of short-term weather and long-term climate patterns has a substantial impact on the cooling performance of coolers designed based on a fixed atmospheric transmission spectrum. Nonetheless, the analysis of the ideal spectrum remains instructive for the design of radiative coolers. In experimental setups, researchers have employed simple horn-shaped metal barriers to effectively shield against large-angle radiative exchanges [89, 90], resulting in a narrow-band angle-selective profile as shown in the second row of figure 6(b), which can be seen as a compromise of the ideal emitter in real-world scenarios. For instance, ideal emitter IV can achieve a temperature drop of 150 °C in a thermally insulated environment, whereas a selective emitter (with  $\varepsilon(\theta > 30^\circ) = 0$ ) with a similar spectral profile (figure 6(b), far right), balancing cooling efficiency and

design/manufacturing complexity, can only realize a temperature drop of less than 100 °C (figure 6(a), blue and dark green solid lines). Compared to the full-angle selective emitters (solid red line in figure 6(a)), the narrow-band angle-selective emitters (solid yellow and dark green lines in figure 6(a)) do incur a loss in cooling power due to the shielding of large-angle radiative exchanges, yet they can achieve relatively lower cooling temperatures under conditions of perfect thermal insulation, with an additional temperature drop of approximately 5 °C–10 °C.

**2.3.2.1. Nonreciprocal thermal emitters.** Theoretical discussions in the preceding sections of this subsection are founded on Kirchhoff's law of thermal radiation [91]. The introduction of thermal nonreciprocity [92], which applies the principle of Lorentz nonreciprocity to the field of thermal sciences, offers a novel strategic approach. By implementing nonreciprocal strategies in thermal nanostructures, such as the use of magneto-optical (MO) materials [93, 94], time-space modulation [95], or optical nonlinear effects [96], it is feasible to disrupt the equivalence between spectral-angular emissivity  $\varepsilon(\lambda, \theta)$  and absorptivity  $\alpha(\lambda, \theta)$ . This innovation not only provides a new path to mitigate the loss mechanisms caused by Kirchhoff's law but also has the potential to enhance energy conversion efficiency.

In nonreciprocal systems, the spectral angular distributions of emissivity and absorptivity on a symmetric hemisphere are not consistent with each other. Consequently, the emitted thermal flux and the absorbed atmospheric thermal flux of the solid surface emitter should be correspondingly adjusted:

$$q_{\text{emi}}(T) = \frac{\pi}{2} \int_0^{\infty} \int_0^{\frac{\pi}{2}} [\varepsilon(\lambda, \theta) + \varepsilon(\lambda, -\theta)] \cdot I_{\text{BB}} \times (\lambda, T) \sin(2\theta) d\theta d\lambda \quad (19)$$

$$q_{\text{atm}}(T_{\text{amb}}) = \frac{\pi}{2} \int_0^{\infty} \int_0^{\frac{\pi}{2}} [\alpha(\lambda, \theta) + \alpha(\lambda, -\theta)] \cdot \varepsilon_{\text{atm}}(\lambda, \theta) I_{\text{BB}} \times (\lambda, T_{\text{amb}}) \sin(2\theta) d\theta d\lambda. \quad (20)$$

As depicted in figure 7(a), in conventional studies, reciprocal thermal emitters that comply with Kirchhoff's law exhibit equal emissivity  $\varepsilon(\lambda, \pm\theta)$  and absorptivity  $\alpha(\lambda, \pm\theta)$  in structures with reverse or translational symmetry, such as multilayered and periodic metasurfaces (inset), satisfying  $\varepsilon(\lambda, \pm\theta) = \varepsilon(\lambda, \mp\theta) = \alpha(\lambda, \pm\theta) = \alpha(\lambda, \mp\theta)$ . However, when the structural symmetry is compromised, an reciprocal yet geometrically asymmetric emission/absorption spectral angular response is observed: specifically,  $\varepsilon(\lambda, \pm\theta) = \alpha(\lambda, \pm\theta)$ , while  $\varepsilon(\lambda, \pm\theta) \neq \varepsilon(\lambda, \mp\theta)$  and  $\alpha(\lambda, \pm\theta) \neq \alpha(\lambda, \mp\theta)$ . This phenomenon has been experimentally verified using asymmetric gratings [97] or micro-wedge geometries [98]. For nonreciprocal systems, the introduction of external energy, such as magnetic or electric energy, is typically required to break Lorentz reciprocity, leading to a complex relationship between spectral angular

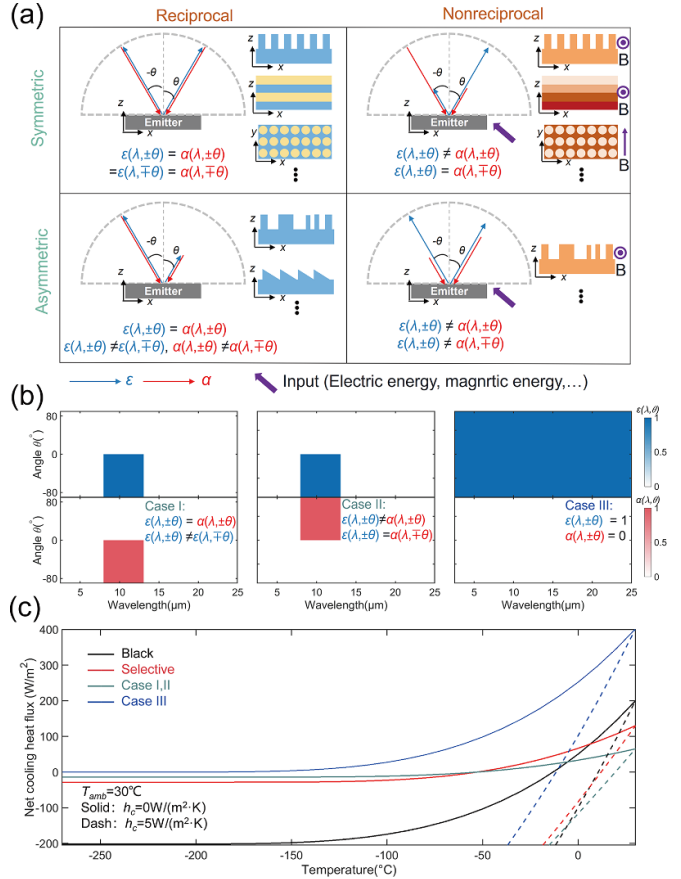


**Figure 7.** Theoretical analysis of nonreciprocal thermal emitters. (a) Relationship between spectral-angular emissivity and absorptivity for thermal emitters classified by reciprocity and geometric symmetry, along with illustrations of the corresponding structures. (b) Spectral angular response profiles of emission/absorption for various geometrically symmetric/asymmetric and radiatively reciprocal/nonreciprocal cases. Case I: reciprocal emission/absorption spectra with geometric asymmetry within the ATSW waveband; case II: nonreciprocal emission/absorption spectra with geometric symmetry within the ATSW waveband; case III: nonreciprocal emission/absorption spectra with geometric asymmetry across the broadband, where the optimal spectra satisfy  $\varepsilon(\lambda, \theta) = 1$ ,  $\alpha(\lambda, \theta) = 0$ . (c) Net cooling heat flux  $q_{\text{cool}}$  versus temperature  $T$  of the radiative cooler under various infrared emissivity profiles  $\varepsilon(\lambda, \theta)$ , including the blackbody emitter (black curve), the 8–13  $\mu\text{m}$  selective emitter (red curve), case I/II in (b) (dark green curve), and case III in (b) (blue curve). The atmospheric transparency window corresponds to a clear sky under conditions of an air mass of 1.5 and a water vapor column of 1 mm, as reported by the Gemini Observatory [82] (available from: <http://www.gemini.edu/sciops/telescopes-and-sites/observing-condition-constraints/ir-transmission-spectra>).

emissivity and absorptivity. For instance, in MO systems with an applied magnetic field  $\mathbf{B}$ , which are extensively studied in nonreciprocal thermophotonics [92], the relation  $\varepsilon(\lambda, \pm\theta, \mathbf{B}) = \alpha(\lambda, \pm\theta, \mathbf{B})$  does not hold regardless of the structure's symmetry. Nevertheless, geometric symmetries still result in  $\varepsilon(\lambda, \pm\theta, \mathbf{B}) = \alpha(\lambda, \pm\theta, \mathbf{B})$ . When thermal emitters are neither reciprocal nor geometrically symmetric [99], no specific relationship between  $\varepsilon(\lambda, \pm\theta, \mathbf{B})$  and  $\alpha(\lambda, \pm\theta, \mathbf{B})$  should be expected.

We firstly consider case I as depicted in figure 7(b): an 8–13  $\mu\text{m}$  band selective emitter is assumed to achieve a reciprocal asymmetric emission/absorption spectral angular response with  $\varepsilon(\theta > 0) = \alpha(\theta > 0) = 0$  and  $\varepsilon(\theta < 0) = \alpha(\theta < 0) = 1$  through the introduction of an asymmetric geometric design. The cooling thermal flux of this emitter as a function of temperature is shown by the dark green line in figure 7(c). It can be observed that, compared to the conventional 8–13  $\mu\text{m}$  selective emitter (red line in figure 7(c)) with a net cooling thermal flux of 130  $\text{W m}^{-2}$ , the net cooling thermal flux of case I is halved due to the reduction of half of the radiative heat exchange channels. Similarly, the atmospheric radiation heat flux in the 8–13  $\mu\text{m}$  band is approximately 28  $\text{W m}^{-2}$  (intersection of the red solid line with the y-axis in figure 7(c)), and the atmospheric radiation heat flux absorbed by case I is also halved to 14  $\text{W m}^{-2}$  (intersection of the dark green solid line with the y-axis in figure 7(c)). This reciprocal asymmetric emitter can be regarded as a special type of spectral angular selective emitter, which can be achieved by shielding a quarter of the hemispherical emission angle with a metal surface perpendicular to the solid surface emitter. Since the atmospheric radiation heat absorption and the emitter's own radiative heat flux are proportionally reduced, the steady-state temperature of case I under thermal insulation conditions is the same as that of the selective emitter (the intersection of the red and green solid lines with the x-axis in figure 7(c)). Therefore, this reciprocal asymmetric design does not offer any additional benefits in terms of temperature reduction and sacrifices a significant portion of the cooling power.

Next, we consider case II as depicted in figure 7(b): a selective emitter in the 8–13  $\mu\text{m}$  band is assumed to achieve a symmetric nonreciprocal emission/absorption spectral angular response with  $\varepsilon(\theta > 0) = \alpha(\theta < 0) = 0$  and  $\varepsilon(\theta < 0) = \alpha(\theta > 0) = 1$  by introducing external energy to break Lorentz reciprocity. The change in cooling thermal flux with temperature for this emitter is also shown by the dark green line in figure 7(c). Due to the generalized Kirchhoff's law and the principle of energy conservation [92], the curve for case II coincides exactly with that of case I. The analysis applied to case I is fully applicable to case II as well. Compared to reciprocal emitters, the symmetric nonreciprocal design does not provide any additional cooling benefits and instead results in a significant sacrifice of cooling power. Up to now, the majority of proposed nonreciprocal thermal emitters belong to this symmetric type.

Finally, we consider case III as depicted in figure 7(b): an idealized blackbody emitter is hypothesized to achieve an ideal nonreciprocal emission/absorption spectral angular response with  $\varepsilon = 1$  and  $\alpha = 0$ . The change in cooling thermal flux with temperature for this emitter is also shown by the blue line in figure 7(c). Case III is analogous to a perfect radiative cooling device that emits all of its thermal radiation outward without any absorption. Compared to a conventional blackbody emitter (black line in figure 7(c), with a net cooling thermal flux of 200  $\text{W m}^{-2}$ ), Case III increases the net cooling thermal flux to 400  $\text{W m}^{-2}$ , nearly doubling the cooling effect, with the difference equating to the total atmospheric radiation across

the broad spectrum (intersection of the black line with the y-axis in figure 7(c)). Additionally, due to the complete absence of absorption, case III can theoretically reach absolute zero (0 K) under thermally insulated conditions. In terms of cooling power and maximum temperature drop, case III is undoubtedly the perfect solution. However, there are currently no effective methods to achieve perfect nonreciprocal effects across the entire thermal radiation spectrum, and this hypothesis simultaneously violates the second and third laws of thermodynamics, making it impractical.

Nevertheless, we can still envision that within narrower bandwidths and relatively weaker modulation ranges, nonreciprocal designs could be used to enhance the efficiency of radiative cooling. Spatiotemporal modulation systems based on the principle of time-reversal symmetry [95, 100–102], which do not require external magnetic field excitation, are promising solutions as they can break the constraints of the law of energy conservation. For instance, a graphene-based grating structure, comprising periodic graphene strips on a dielectric substrate and a perfect electric conductor substrate, forms a dynamically modulated Fermi level for traveling waves, achieving nonreciprocal radiation and absorption characteristics under extremely narrow angular bandwidth (only 36.73°) and wavelength bandwidth ( $14.267 \pm 0.013 \mu\text{m}$ ) [100]. However, it is noteworthy that although spatiotemporal modulation has shown effectiveness in actively controlling nonreciprocal thermal radiation without an external magnetic field, physical experimental validation in the thermal radiation spectrum remains to be achieved. Currently, the angular and spectral ranges of nonreciprocal spectra are extremely narrow, and realizing broadband or wide-angle nonreciprocal radiation using magnet-free spatiotemporal modulation remains an open challenge.

## 2.4. Theoretical models refined for practical scenarios

In practical applications, as illustrated in figure 8, radiative cooling devices are frequently integrated within more intricate systems. This necessitates the consideration of various factors, including the radiative interactions between the emitter and the external environment (e.g. buildings, mountains), the thermal equilibrium process between the emitter and the internal environment (e.g. building envelopes and indoor spaces, clothing and human body), the differences between the internal and external surfaces of the emitter, the orientation of the emitter, and subambient heat conduction, among others. Under these circumstances, the simplified model of a solid surface emitter is no longer sufficient and requires modification. Thus, modified models tailored for several potential real-world scenarios are required to provide more accurate descriptions of radiative cooling systems.

**2.4.1. Thermal management in a thermostatically controlled indoor environment.** Building energy consumption accounts for approximately 40% of the global total energy consumption, with a significant portion of this energy being

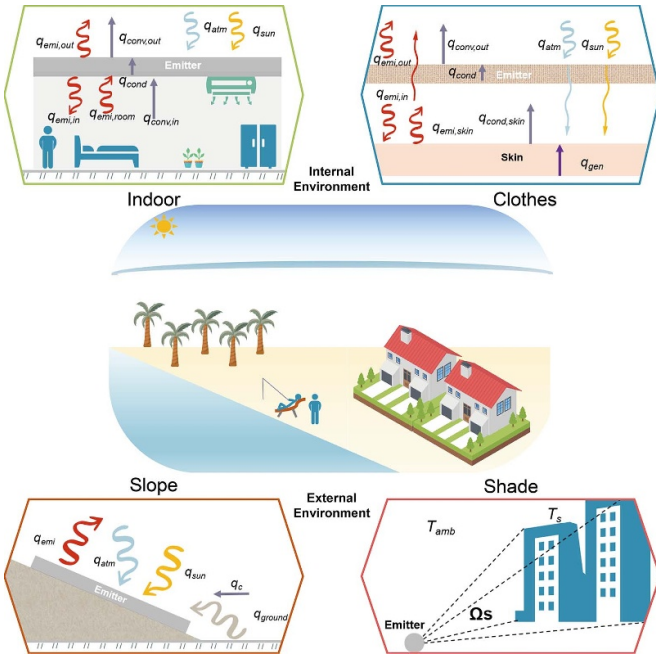


**Figure 8.** Thermodynamic equilibrium under commonly used correction models.

utilized through traditional heating, ventilation, and air conditioning (HVAC) systems for indoor thermal management (ITM) [103]. Consequently, passive radiative cooling methods that cool objects without the need for additional energy input can play a crucial role in the development of energy-efficient buildings.

In the realm of ITM, it is imperative to consider not only the thermal interaction between the emitter and the indoor environment, but also the exchange of heat amidst planar emitters and the outdoor atmosphere. The roof's upper and lower surfaces, serving as emitters, often exhibit distinct emissivity, necessitating a thorough consideration of the thermodynamic interactions involved. Concurrently, due to the presence of indoor air conditioning, the indoor environment is commonly treated as a thermally equilibrated blackbody in simulations. A steady-state heat transfer model analysis was used to evaluate the heat flux of the slab to the indoor environment and calculate the heating set point when applied to indoor environment (figure 8).

When calculating the heat flux to the indoor environment of slab as canopy, the energy balance equations of the outer and inner surfaces of the slab are as follows [104],

$$q_{\text{emi,out}} + q_{\text{conv,out}} = \varepsilon_{\text{out,ir}} \cdot q_{\text{atm}} + q_{\text{cond}} + \varepsilon_{\text{sun}} \cdot q_{\text{sun}} \quad (21)$$

$$q_{\text{emi,in}} + q_{\text{cond}} = \varepsilon_{\text{in,ir}} \cdot q_{\text{emi,room}} + q_{\text{conv,in}}. \quad (22)$$

Here,  $q_{\text{emi,out}}$  and  $q_{\text{emi,in}}$  are employed to represent the radiative heat flux emitted by the outer and inner surfaces of the slab, respectively.  $q_{\text{emi,room}}$  represents the radiative heat flux from the room.  $q_{\text{sun}}$  represents the solar radiative heat flux.  $q_{\text{atm}}$  represents the atmospheric radiative heat flux.  $q_{\text{cond}}$  represents the conductive heat flux from the interior to the

exterior of the slab.  $q_{\text{conv,out}}$  and  $q_{\text{conv,in}}$  denote the convective heat transfer coefficient of the slab outer and inner surface, respectively,

$$q_{\text{emi,out}}(T_{\text{out}}) = \varepsilon_{\text{out,ir}} \sigma T_{\text{out}}^4 \quad (23)$$

$$q_{\text{emi,in}}(T_{\text{in}}) = \varepsilon_{\text{in,ir}} \sigma T_{\text{in}}^4 \quad (24)$$

$$q_{\text{emi,room}}(T_{\text{room}}) = \sigma T_{\text{room}}^4 \quad (25)$$

$$q_{\text{atm}}(T_{\text{amb}}) = \int_0^{\frac{\pi}{2}} \int_0^{\infty} \pi \sin(2\theta) \cdot I_{\text{BB}}(T_{\text{amb}}, \lambda) \times \left(1 - \tau_{\text{atm}}(\lambda)^{1/\cos(\theta)}\right) d\theta d\lambda \quad (26)$$

$$q_{\text{sun}} = \cos\theta_{\text{sun}} \int_0^{+\infty} I_{\text{AM1.5G}}(\lambda) d\lambda \quad (27)$$

$$q_{\text{cond}} = k_{\text{slab}} \cdot \frac{T_{\text{in}} - T_{\text{out}}}{t_{\text{slab}}} \quad (28)$$

$$q_{\text{conv,out}} = h_{\text{out}} \cdot (T_{\text{room}} - T_{\text{in}}) \quad (29)$$

$$q_{\text{conv,in}} = h_{\text{in}} \cdot (T_{\text{room}} - T_{\text{in}}). \quad (30)$$

Furthermore,  $\theta_{\text{sun}}$  is the angle between the direction of the incident solar radiation and the normal direction of the outer surface.  $T_{\text{amb}}$ ,  $T_{\text{out}}$ ,  $T_{\text{in}}$ , and  $T_{\text{room}}$  represent the ambient temperature, the temperature of the outer slab surface, the temperature of the inner slab surface, and indoor temperature, respectively. The Stefan-Boltzmann constant, denoted as  $\sigma = 5.67 \times 10^{-8} \text{ W} (\text{m}^2 \cdot \text{K}^4)^{-1}$ .  $\varepsilon_{\text{out,ir}}$  and  $\varepsilon_{\text{in,ir}}$  correspond to the emissivity of the outer and inner surfaces of the slab, respectively.  $h_{\text{out}}$  and  $h_{\text{in}}$  represent the convective heat transfer coefficient at the outer and inner surfaces of the slab, respectively.  $k_{\text{slab}}$  represents the thermal conductivity of the slab, and  $t_{\text{slab}}$  indicates the thickness of the slab.

And the net cooling heat flux of slab could be calculated.

$$q_{\text{net,slab}} = \tau_{\text{slab,ir}} \cdot q_{\text{emi,room}} + \varepsilon_{\text{in,ir}} \cdot q_{\text{emi,room}} + q_{\text{conv,in}} - (q_{\text{emi,in}} + \tau_{\text{slab,sun}} \cdot q_{\text{sun}} + \tau_{\text{slab,ir}} \cdot q_{\text{atm}}) \quad (31)$$

where  $\tau_{\text{slab,sun}}$  and  $\tau_{\text{slab,ir}}$  denote the solar spectrum-weighted transmission and infrared band-weighted transmission, respectively, of the slab.

It is worth noting that the ITM model presented in this study is specifically tailored for the scenario where a radiatively controlled slab is used as a canopy. When the slab is utilized as a wall, the calculations must be integrated with the special case of a tilted surface model section (2.4.3) rotated 90 degrees. Adhering to this protocol, a range of simple models can be employed to accommodate the majority of radiative control material applications, thereby facilitating a comprehensive thermodynamic analysis.

**2.4.2. Thermal management of emitter under thermal source influence.** Objects subject to cooling are frequently influenced by other heat sources. Activities such as the operation of machinery and human occupancy within a building generate additional heat. For ITM models, this surplus heat can be

counteracted by the functioning of HVAC systems. However, in other thermal management models, such as those focused on personal thermal comfort, the extra heat absorbed by objects must be taken into account in the heat balance computations.

Radiative regulating textiles, a rapidly evolving research area, are characterized by their lightweight, breathable, and moisture-wicking properties, which frequently constrain the thickness of the fabric and present an undeniable level of translucency. The material attributes of the textile's inner and outer surfaces are often significantly distinct, mandating separate and nuanced analysis. Furthermore, thermodynamic assessments of these textiles must also incorporate the thermal conductivity of the air gap between the fabric and the skin, as well as the heat produced by the human body at rest. Human skin has been demonstrated to function as an almost blackbody radiator, with an emissivity exceeding 0.96 [105]. The application of passive radiative cooling and heating for PTM is an emerging topic within the engineering field.

A steady-state heat transfer model analysis was used to evaluate the heat power of the textile to the outdoor PTM (figure 8). When calculating the heat flux to the outdoor PTM, ignoring the convection of the air gap between the human body and the textiles, the energy balance equations of the inner and outer surfaces of the textile are as follows [104].

On outer surface:

$$q_{\text{gen}} = -\varepsilon_{\text{out,ir}} \cdot q_{\text{atm}} + q_{\text{emi,out}} + q_{\text{conv,out}} - \left[ (1 - r_{\text{tex,sun}}) - \frac{\tau_{\text{tex,sun}}^2 \cdot r_{\text{skin,sun}}}{1 - r_{\text{tex,sun}} \cdot r_{\text{skin,sun}}} \right] \cdot q_{\text{sun}}. \quad (32)$$

On skin surface:

$$q_{\text{gen}} = (1 - r_{\text{in,ir}}) \cdot q_{\text{emi,skin}} - q_{\text{emi,in}} + q_{\text{cond,skin}} - \frac{\tau_{\text{tex,sun}} \cdot \varepsilon_{\text{skin,sun}}}{1 - r_{\text{tex,sun}} \cdot r_{\text{skin,sun}}} \cdot q_{\text{sun}}. \quad (33)$$

The process of heat transfer within textiles:

$$T_{\text{out}} - T_{\text{in}} = \frac{t_{\text{tex}}}{k_{\text{tex}}} \left( \varepsilon_{\text{in,ir}} \sigma T_{\text{in}}^4 + \varepsilon_{\text{out,ir}} \sigma T_{\text{out}}^4 - \varepsilon_{\text{in,ir}} \sigma T_{\text{skin}}^4 - \varepsilon_{\text{out,ir}} \cdot q_{\text{atm}} - \varepsilon_{\text{tex,sun}} \cdot q_{\text{sun}} \right) - \frac{k_a (T_{\text{skin}} - T_{\text{in}}) t_{\text{tex}}}{k_t t_{\text{air}}}. \quad (34)$$

Here,  $q_{\text{emi,in}}$ ,  $q_{\text{emi,out}}$ , and  $q_{\text{emi,skin}}$  denote the radiative heat fluxes at the inner surface, outer surface, and skin surface of the textile, respectively.  $q_{\text{atm}}$  represents the radiative heat flux from the atmosphere.  $q_{\text{sun}}$  indicates the solar radiation flux.  $q_{\text{cond,skin}}$  signifies the heat transfer from the skin through the air gap to the textile.  $q_{\text{conv,out}}$  denotes the convective heat fluxes at the outer surface of the textile.  $q_{\text{gen}}$  represents metabolic heat generation flux.  $\tau_{\text{tex,sun}}$  and  $\tau_{\text{tex,ir}}$  denote the solar spectrum-weighted transmission and infrared band-weighted transmission, respectively, of the textile.  $\varepsilon_{\text{out,ir}}$  represent the infrared band-weighted absorption at the outer surface of the textile.  $\varepsilon_{\text{in,ir}}$  signify the infrared band-weighted absorption, at the inner

surface of the textile.  $\varepsilon_{\text{tex,sun}}$  and  $\varepsilon_{\text{skin,sun}}$  represent the solar absorption of the textile and skin, respectively.

$$q_{\text{emi,out}} (T_{\text{out}}) = \varepsilon_{\text{out,ir}} \sigma T_{\text{out}}^4 \quad (35)$$

$$q_{\text{emi,in}} (T_{\text{in}}) = \varepsilon_{\text{in,ir}} \sigma T_{\text{in}}^4 \quad (36)$$

$$q_{\text{emi,skin}} (T_{\text{skin}}) = \sigma T_{\text{skin}}^4 \quad (37)$$

$$q_{\text{atm}} (T_{\text{amb}}) = \int_0^{\frac{\pi}{2}} \int \pi \sin(2\theta) \cdot I_{\text{BB}} \times (T_{\text{amb}}, \lambda) \left( 1 - \tau_{\text{atm}}(\lambda)^{1/\cos(\theta)} \right) d\theta d\lambda \quad (38)$$

$$q_{\text{sun}} = \cos \theta_{\text{sun}} \int_0^{+\infty} I_{\text{AM1.5G}} (\lambda) d\lambda \quad (39)$$

$$q_{\text{cond,skin}} = k_{\text{air}} \cdot \frac{T_{\text{skin}} - T_{\text{in}}}{t_{\text{air}}} \quad (40)$$

$$q_{\text{conv,out}} = h_{\text{out}} \cdot (T_{\text{out}} - T_{\text{amb}}). \quad (41)$$

For the sake of consistency in formula presentation, there is an overlap in content between equations (23)–(30) and (35)–(41). Where  $T_{\text{skin}}$  represent the skin temperature of the textile.  $t_{\text{tex}}$  and  $t_{\text{air}}$  represent the thickness of the textile and the air gap, respectively.  $k_{\text{tex}}$  and  $k_{\text{air}}$  denote the thermal conductivities of the textile and air, respectively.

Furthermore, under non-steady-state conditions, the transient cooling heat flux of the textile can be calculated based on equations (32) and (33),

$$\begin{aligned} q_{\text{cool,skin}} &= (1 - r_{\text{in,ir}}) \cdot q_{\text{emi,skin}} - q_{\text{emi,in}} + q_{\text{cond,skin}} \\ &\quad - \frac{\tau_{\text{tex,sun}} \cdot \varepsilon_{\text{skin,sun}}}{1 - r_{\text{tex,sun}} \cdot r_{\text{skin,sun}}} \cdot q_{\text{sun}} - q_{\text{gen}} \\ &= -\varepsilon_{\text{out,ir}} \cdot q_{\text{atm}} + q_{\text{emi,out}} + q_{\text{conv,out}} \\ &\quad - \left[ (1 - r_{\text{tex,sun}}) - \frac{\tau_{\text{tex,sun}}^2 \cdot r_{\text{skin,sun}}}{1 - r_{\text{tex,sun}} \cdot r_{\text{skin,sun}}} \right] \cdot q_{\text{sun}} - q_{\text{gen}}. \end{aligned} \quad (42)$$

Notably, the specific spectral requirements for radiation-regulating textiles vary depending on the application scenario. For example, textiles designed for cooling purposes may require infrared transparency/emissivity, while those for insulation purposes may necessitate infrared reflectivity. Additionally, there are Janus textiles that aim to balance cooling and insulation. Therefore, it is essential to design the spectral properties of the textile's inner and outer surfaces with a more specific application.

#### 2.4.3. Thermal management of emitter with varying posture and orientation.

The diverse application scenarios of radiative cooling technology necessitate that the posture of emitters are not limited to facing the sky directly. In fact, an appropriate tilt angle is essential based on the specific application requirements. For instance, in the construction field, radiative cooling materials are applicable not only to horizontal roofs but also to sloped roofs and vertical walls. In the context

of radiative cooling textiles, it is noted that approximately 97% of a standing person's clothing area is perpendicular to the ground [106]. Moreover, radiative cooling devices are capable of effectively reducing the temperature of PV cells, mitigating the performance degradation caused by elevated temperatures [107]. In mid-latitude regions, where sunlight utilization is paramount, PV systems are typically installed at specific angles to optimize their capture of solar radiation throughout the year, across various seasons and time periods [108]. Consequently, the model of a solid surface emitter is not directly applicable to the inclined surface emitters represented by solar cells.

To evaluate the cooling performance of the emitter with a tilt angle of  $\theta_t$ , as depicted in the figure 8, we utilized a simplified model of a tilt surface emitter to analyze the energy balance of the emitter. The cooling flux  $q_{\text{cool,tilt}}(T)$  can be calculated by the following thermal equilibrium:

$$\begin{aligned} q_{\text{cool,tilt}}(T) = & q_{\text{emi}}(T) - q_{\text{ground}}(T_{\text{ground}}, \theta_t) \\ & - q_{\text{atm}}(T_{\text{amb}}, \theta_t) - q_{\text{sun}}(\theta_{\text{sun}}) - q_c. \end{aligned} \quad (43)$$

In contrast to a solid surface emitter facing the sky, the tilt surface emitter, due to its angular inclination  $\theta_t$ , not only experiences a change in the solar incidence angle,  $\theta_{\text{sun}}$ , but also undergoes a modification in the amount of atmospheric radiation it absorbs. Furthermore, the tilt surface emitter additionally captures a portion of the radiation emanating from the ground. The ground is often modeled as a blackbody, with its temperature  $T_{\text{ground}}$  typically not lower than the temperature of the ambient atmosphere,  $T_{\text{amb}}$ .

Due to the emitter's tilt, it receives a portion of the radiation from the ground:

$$\begin{aligned} q_{\text{ground}}(T_{\text{ground}}, \theta_t) = & \int_{\theta_t}^{\frac{\pi}{2}} \sin \theta \cos \theta [2 * \cos^{-1}(\cot \theta * \cot \theta_t)] \\ & \times d\theta \int_0^{\infty} I_{\text{BB}}(\lambda, T_{\text{ground}}) \varepsilon(\lambda) d\lambda. \end{aligned} \quad (44)$$

When examining the interaction between an inclined surface and atmospheric radiation, the radiation absorbed by the surface,  $q_{\text{atm}}(T_{\text{amb}}, \theta_t)$  can be expressed as follows:

$$\begin{aligned} q_{\text{atm}}(T_{\text{amb}}, \theta_t) = & \int_0^{\infty} \int_0^{2\pi} \int_0^{\frac{\pi}{2}} \sin \theta \cos \theta \varepsilon_{\text{atm}}(\lambda, \theta_n) I_{\text{BB}} \\ & \times (\lambda, T_{\text{amb}}) \varepsilon_{\text{top}}(\lambda) d\theta d\psi d\lambda. \end{aligned} \quad (45)$$

Here,  $\psi$  represents the azimuthal angle in the hemispherical coordinate system.  $\theta_n$  is the angle with respect to the zenith direction, which is given by equation (47).  $\varepsilon_{\text{atm}}(\lambda, \theta_n)$  is the emissivity of the atmosphere which is given by equation (48),

$$\theta_n(\theta, \psi, \theta_t) = \cos^{-1}(\sin \theta \cos \psi \sin \theta_t + \cos \theta \cos \theta_t) \quad (46)$$

$$\varepsilon_{\text{atm}}(\lambda, \theta_n) = \begin{cases} 1 - \tau(\lambda)^{\frac{1}{\cos \theta_n}}, & \theta_n < \frac{\pi}{2} \\ 0, & \theta_n \geq \frac{\pi}{2} \end{cases} \quad (47)$$

where  $\tau(\lambda)$  is the atmospheric transmittance in the zenith direction.

**2.4.4. Thermal management of emitter with limited radiating angle range.** The previously described models characterize the thermal radiation behavior of emitters in open environment scenarios. In practical applications, however, an unobstructed setting is often unattainable. Within certain radiating angular ranges, the emitter is expected to primarily engage in radiative heat exchange with surrounding objects, rather than the sky, due to the presence of obstructions. For instance, in urban area, the radiative impact from adjacent buildings must be considered. Accounting for the radiative heat flux  $q_s$  from the surrounding objects, the cooling flux  $q_{\text{cool}}(T)$  can be calculated by the following thermal equilibrium:

$$\begin{aligned} q_{\text{cool}}(T) = & q_{\text{emi}}(T) - q_s(T_s, \Omega_s) - q_{\text{atm}}(T_{\text{amb}}, \Omega_s) \\ & - q_{\text{sun}} - q_c. \end{aligned} \quad (48)$$

Initially, we address the impact of obstructions on solar radiation. Given the average Earth–Sun distance of approximately 150 million kilometers, the sunlight received at the Earth's surface can be treated as parallel beams. Neglecting the reflection of sunlight by the surrounding environment, the solar radiation absorbed by an emitter,  $q_{\text{sun}}$ , remains unaffected unless it is directly shaded by adjacent obstructions. If an emitter with a total area of  $A$  has an area  $A_s$  shaded, the absorbed solar radiation  $q_{\text{sun,shad}}$  can be simply determined by multiplying the original solar radiation by the ratio of the unshaded area to the total area,  $(A - A_s)/A$ . Moreover, when surrounding obstructions are in close proximity to the emitter, the multiple reflections and scattering of sunlight between the emitter and obstructions cannot be overlooked. This can lead to a several-fold increase in the solar radiation absorbed by the emitter, substantially diminishing the cooling efficacy of radiative cooling devices. Consequently, it is imperative to maintain an adequate distance between the radiative cooling devices and the surrounding environment during and application.

In contrast to open scenarios, the presence of obstructions leads to a situation where the atmospheric radiation absorbed by a solid surface emitter within the obstructed solid angle  $\Omega_s$  is replaced by the radiation  $q_s$  from the surrounding objects (figure 8). The expressions for  $q_s(T_s, \Omega_s)$  and the absorbed atmospheric radiation  $q_{\text{atm}}(T_{\text{amb}}, \Omega_s)$  are as follows:

$$\begin{aligned} q_{\text{atm}}(T_{\text{amb}}, \Omega_s) = & \int_0^{\Omega_s} d\Omega \cos \theta \int_0^{\infty} d\lambda I_{\text{BB}} \\ & \times (T_{\text{amb}}, \lambda) \varepsilon_{\text{atm}}(\lambda, \theta) \varepsilon(\lambda, \theta) \end{aligned} \quad (49)$$

$$q_s(T_s, \Omega_s) = \int_0^{\Omega_s} d\Omega \cos \theta \int_0^{\infty} d\lambda I_{\text{BB}}(T_s, \lambda) \varepsilon(\lambda, \theta). \quad (50)$$

Surrounding objects are commonly modeled as blackbodies with a specific surface temperature  $T_s$ . In urban settings

during clear summer days, due to the urban heat island effect, the surface temperature  $T_s$  of buildings can be approximately 20 °C higher than the ambient atmospheric temperature  $T_{\text{amb}}$ .

To mitigate the impact of radiative heat transfer from the surrounding environment at higher temperatures, angle modulation of the emitter's spectral properties can effectively enhance the cooling effect. For instance, in 2023, the Cui team innovatively designed a micro-wedge structure tailored for manipulating the direction of thermal radiation emission, thereby effectively controlling the directional emission of heat radiation [98]. Due to meticulous engineering design, this micro-wedge structure achieves significant variation in its spectral directional emissivity, with a broad range from 0.9 to 0.1, demonstrating exceptional contrast tuning capabilities. Particularly on outdoor vertical surfaces, compared to isotropic emitters, this angular-selective emitter can provide superior daytime radiative cooling performance, with a cooling enhancement of up to 2 °C.

In this section, we thoroughly investigate the intrinsic mechanisms and extrinsic factors influencing radiative cooling. To optimize the radiative cooling effect, it is essential to integrate actual environmental conditions and application scenarios, and to conduct precise optimization design for specific wavelengths and angles. This design aims to minimize absorbed external radiation and maximize the device's own radiative heat dissipation, thereby achieving the desired cooling temperature or cooling power. In the subsequent section, we will delve into the specific design concepts and methodologies for achieving these objectives.

### 3. Design of radiation cooling structures

In the realm of daytime radiative cooling, the task of meeting the exacting criteria for solar reflectance and infrared emission across the full spectrum has emerged as a challenge that no single raw material has been capable of satisfying. Consequently, the employment of at least two raw materials (including air) in the fabrication of radiative cooling materials marks a pivotal advance in the material's development. In response, researchers have focused on structural design, amalgamating various materials with distinct optical properties into composite materials to achieve broad spectral tuning of the base material. This strategy markedly improves the material's spectral responsiveness, characterized by heightened solar reflectance and augmented infrared emission. The design of these structures is critically important, as it entails the strategic integration and optimization of the spectral properties of diverse raw materials to engineer functional materials with optimized selective spectral characteristics. This section will provide a review of simulation methodologies and commonly employed structures within the field.

#### 3.1. Typical optical simulation methods in the design of radiative cooling structures

As fabrication technology advances, nanostructures have been proposed and fabricated to achieve radiative cooling effects.

To investigate the properties of materials and optimize their composition and structure prior to manufacturing, a variety of simulation methods have been employed. The optical properties of radiative cooling materials, with various combinations of materials, layer numbers, thicknesses, and diverse particle sizes and shapes, can be optimized by numerically solving Maxwell's equations [109].

The applications of numerical techniques and commercial software in calculating the optical properties of radiative cooling materials have greatly facilitated the development of this field. Given the availability of multiple simulation methods, it is crucial to understand their accuracy and limitations before choosing the most appropriate one for a particular application.

**3.1.1. Transfer matrix method (TMM).** The TMM stands as an efficient numerical technique for calculating the propagation characteristics of electromagnetic waves within one-dimensional periodic structures. Grounded in the boundary conditions of the wave equation, this method represents the electromagnetic properties of each layer in matrix form, with the entire structure's impact on wave transmission being computed through matrix multiplication.

In the context of one-dimensional periodic structures composed of multiple dielectric layers, each layer is represented by a  $2 \times 2$  transfer matrix. If we denote the transfer matrix of the  $m$ th layer as  $M_m$ , the relationship can be established as follows:

$$\begin{bmatrix} E_m \\ H_m \end{bmatrix} = \begin{bmatrix} \cos\delta_m & -\frac{i}{\eta_m} \sin\delta_m \\ -i\eta_m \sin\delta_m & \cos\delta_m \end{bmatrix} \cdot \begin{bmatrix} E_{m+1} \\ H_{m+1} \end{bmatrix} = M_m \cdot \begin{bmatrix} E_{m+1} \\ H_{m+1} \end{bmatrix} \quad (51)$$

where

$$\delta_m = \frac{2\pi}{\lambda} n_m d_m \cos\theta_{i,m+1} \quad (52)$$

$$\eta_m = \begin{cases} \sqrt{\frac{\epsilon_0}{\mu_0}} \cdot n_m \cos\theta_{i,m+1}, & (\text{s wave}) \\ \sqrt{\frac{\epsilon_0}{\mu_0}} \cdot \frac{n_m}{\cos\theta_{i,m+1}}, & (\text{p wave}) \end{cases} \quad (53)$$

$\lambda$  refers to the wavelength of the incident light in vacuum,  $n_m$  indicates the refractive index of the  $m$ th layer,  $d_m$  signifies its thickness, and  $\theta_{i,m+1}$  is the angle of incidence at which light propagates from the  $m$ th layer into the  $(m+1)$ th layer.

In the model of electromagnetic wave propagation, the transmission characteristics of the entire structure are encapsulated by the product of the individual layer transfer matrices. For a structure composed of  $N$  layers, the total transfer matrix  $M$  is:

$$\begin{bmatrix} E_1 \\ H_1 \end{bmatrix} = M_1 \cdot M_2 \cdot M_3 \cdots M_N \begin{bmatrix} E_{N+1} \\ H_{N+1} \end{bmatrix} = M \begin{bmatrix} E_{N+1} \\ H_{N+1} \end{bmatrix}. \quad (54)$$

Next, we employ the TMM to compute the transmittance and reflectivity. Let the elements of the transfer matrix  $M$  be denoted as  $A$ ,  $B$ ,  $C$ , and  $D$ ,

$$M = \begin{bmatrix} A & B \\ C & D \end{bmatrix}. \quad (55)$$

The transmission and reflection coefficients of the thin-film system are expressed as follows:

$$r = \frac{A\eta_0 + B\eta_0\eta_{N+1} - C - D\eta_{N+1}}{A\eta_0 + B\eta_0\eta_{N+1} + C + D\eta_{N+1}} \quad (56)$$

$$t = \frac{2\eta_0}{A\eta_0 + B\eta_0\eta_{N+1} + C + D\eta_{N+1}}. \quad (57)$$

The reflectance and transmittance are expressed as  $R = r \cdot r^*$  and  $T = t \cdot t^*$ , respectively.

In the computational task of spectral response for structures designed to control light via thin-film interference, the TMM demonstrates unparalleled efficiency and speed, showcasing its outstanding performance. When integrated with cutting-edge optimization algorithms such as needle optimization, TMM is capable of rapidly executing the optimized design of thin-film structures based on predefined spectral objectives. This unique attribute positions TMM as a preeminent tool in the design research of one-dimensional photonic crystals and multi-layer film structures.

However, TMM necessitates that each layer be composed of a uniform dielectric with a constant dielectric constant. As such, it is not directly applicable to the simulation of complex optical composite structures. To address this limitation, it is imperative to first employ alternative methods to determine the effective dielectric constant of the composite material. Only then can the TMM be utilized to proceed with the calculation of the optical properties.

**3.1.2. Effective medium theory (EMT).** The EMT for composite materials is derived from the fundamental laws of electromagnetism, with its cornerstone being the linear constitutive relationship between the electric displacement vector  $D$  and the electric field intensity  $E$ . In an ideal, spatially isotropic homogeneous dielectric, this relationship is expressed as  $D = \epsilon E$ . For the composite, non-uniform media, the effective dielectric constant is defined as follows:

$$\int_V D(x, y, z) dx dy dz = \epsilon_{\text{eff}} \int_V E(x, y, z) dx dy dz. \quad (58)$$

By adopting certain assumptions about the geometric shape and topological structure of inclusions within non-uniform media, an analytical expression for the macroscopic dielectric constant of non-uniform media can be obtained. This expression is a function of the volume fractions and dielectric constants of the constituent components. The most celebrated are the M–G theory and the Bruggeman theory, both of which are EMTs applicable to systems with spherical inclusions where the particle diameter is much smaller than the wavelength. However, the M–G theory treats the matrix as a continuous phase and the filler particles as discontinuous, whereas the Bruggeman theory views both the matrix and the filler as discontinuous particles.

For composite systems with spherical particles, the M–G formula [110] is expressed as:

$$\epsilon_{\text{eff}} = \frac{\epsilon_2 [\epsilon_1 + 2\epsilon_2 + 2f(\epsilon_1 - \epsilon_2)]}{\epsilon_1 + 2\epsilon_2 - f(\epsilon_1 - \epsilon_2)} \quad (59)$$

where  $\epsilon_{\text{eff}}$  is the effective dielectric constant,  $\epsilon_1$  is the dielectric constant of the particles (dispersed phase),  $\epsilon_2$  is the dielectric constant of the matrix, and  $f$  is the particle volume fraction. The M–G theory is not symmetric and necessitates the assumption that one component is the dispersed phase and the other is the matrix.

The Bruggeman formula [111] is given by:

$$f \frac{\epsilon_1 - \epsilon_{\text{eff}}}{\epsilon_1 + 2\epsilon_{\text{eff}}} + (1-f) \frac{\epsilon_2 - \epsilon_{\text{eff}}}{\epsilon_2 + 2\epsilon_{\text{eff}}} = 0. \quad (60)$$

In this equation,  $\epsilon_1$  and  $\epsilon_2$  are the dielectric constants of the particles (dispersed phase) and the matrix, respectively,  $\epsilon_{\text{eff}}$  is the effective dielectric constant, and  $f$  and  $(1-f)$  are the volume fractions of the respective components. The Bruggeman theory is a symmetric theory where different components are treated equivalently in the formula.

These EMTs are derived under static field conditions. When the variation of the electric field strength is sufficiently slow, there is no significant difference in the response of the medium to static and slowly varying fields. When the wavelength of the incident wave is much larger than the physical size of the components, the medium can be considered to be under the influence of a static field, making the EMTs applicable.

In the field of radiative thermal management, the design of photonic devices with non-periodic porous structures and randomly doped particle structures is commonly treated as homogeneous dispersion systems. The dispersed phase within these systems, whether particles or air voids, primarily functions to scatter sunlight, with physical dimensions mostly at the sub-micron scale. Consequently, in the MIR spectral range, such structures are well-suited for treatment as homogeneous media via the EMT approach, which simplifies models and enhances simulation efficiency.

Furthermore, for periodic photonic devices, the EMT method is also applicable to two-dimensional photonic crystals and metasurfaces when their periodicity is much smaller than the incident wavelength. However, it is important to note that the constituents of composite materials are not always directly equivalent to simple spherical particles. For instance, in structures with fibrous random doping or cruciform metasurface unit cells, the effective dielectric constant may be anisotropic. In such cases, the M–G or Bruggeman formulas need to be modified based on the EMT theory. In summary, when applicable conditions are met, the application of EMT theory effectively streamlines models and improves the efficiency of simulation calculations.

Nevertheless, when the constituent size of composite materials increases to a scale comparable to the wavelength of incident light, the variation in electric field strength becomes pronounced [112]. Under such circumstances, the medium can

no longer be treated as being under static or slowly varying fields. Consequently, the various approximation formulas within the EMT become inapplicable, necessitating the adoption of more precise models to describe these complex physical phenomena [113].

**3.1.3. Monte Carlo method (MCM).** The MCM is a numerical technique based on stochastic sampling that is used to address complex physical processes. In the field of radiative thermal management, this method is frequently employed to compute the spectral characteristics of randomly scattering media with particle doping. For multi-layered random optical media doped with micro and nano-sized particles, assuming that the particles are spaced sufficiently far apart so that their scattering fields do not couple, light can be treated as classical particles and a geometric optics approximation can be applied. The propagation of light within the medium can thus be decomposed into a series of independent events including transmission, scattering, absorption, reflection, and transmission [114]. If the effective scattering coefficient  $\sigma_{\text{eff}}$ , effective absorption coefficient  $\kappa_{\text{eff}}$ , and effective asymmetry factor (anisotropy parameter)  $g_{\text{eff}}$  for each layer of the medium are known, a photon packet with weight  $W$  can be emitted into the random medium during a single sampling instance. As the photon packet undergoes absorption, reflection, and transmission during propagation, the value of  $W$  will decrease until the energy of the photon packet is completely dissipated [115],

$$\sigma_{\text{eff}} = \pi \int_0^{\infty} Q_s R^2 N(R) dR \quad (61)$$

$$\kappa_{\text{eff}} = \pi \int_0^{\infty} Q_a R^2 N(R) dR \quad (62)$$

$$g_{\text{eff}} = \frac{\pi}{\sigma_{\text{eff}}} \int_0^{\infty} Q_s g R^2 N(R) dR. \quad (63)$$

The dimensionless scattering coefficient ( $Q_s$ ) and the dimensionless absorption coefficient ( $Q_a$ ) are computed using Mie theory. Additionally, the asymmetry parameter ( $g$ ), which characterizes the asymmetry of the scattering process, is also derived from Mie theory. The quantity  $N(R)$  represents the number of particles with radius  $R$  per unit volume. During each photon-particle interaction where scattering occurs, it is essential to determine the deflection angle  $\theta_s$  of the photon packet, which dictates the direction of its subsequent propagation. This angle  $\theta_s$  can be calculated using the effective asymmetry parameter  $g_{\text{eff}}$ .

$$\cos \theta_s = \begin{cases} \frac{1}{2g_{\text{eff}}} \left[ 1 + g_{\text{eff}}^2 - \left( \frac{1-g_{\text{eff}}^2}{1-g_{\text{eff}}+2g_{\text{eff}}\xi} \right)^2 \right], & g_{\text{eff}} \neq 0 \\ 2\xi - 1, & g_{\text{eff}} = 0 \end{cases} \quad (64)$$

$\xi$  denotes a uniformly distributed random number within the interval  $(0,1)$ . Ultimately, by conducting sampling statistics on the behavior of a large number of photon packets of the

same type, we can progressively approximate the theoretical value of the medium's optical response.

The MCM facilitates a relatively rapid prediction of the spectral and light field control characteristics in random scattering media. Owing to its statistical nature, the results are insensitive to specific structural variations when a sufficiently large number of samples is used. However, it is important to note that since the method overlooks interference effects of light and coupling between particles during computation, it yields accurate results primarily at low particle concentrations. At higher doping concentrations, the MCM may deviate from actual values. Nonetheless, in scenarios where phenomena such as Anderson localization or coherent backscattering are not pertinent, the MCM still offers qualitative guidance for the design of scattering media.

**3.1.4. Full-wave electromagnetic simulation.** While the aforementioned methods demonstrate unique precision and efficiency advantages in simulating specific optical structures, they fall short in addressing more general cases such as high-concentration scatterer doping, particles with specific shapes, and multilevel structures. These methods are inadequate for precise evaluation of optical properties due to the difficulty in obtaining analytical results. In these instances, the introduction of full-wave electromagnetic simulation models becomes imperative, enabling numerical solutions to Maxwell's equations for accurate depiction of electromagnetic behavior.

Rigorous coupled-wave analysis (RCWA) is a semi-analytical electromagnetic simulation technique that expands the electromagnetic fields and the device to be simulated in the Fourier domain. During the simulation, the device is conceptualized as a multilayered structure, with each layer exhibiting uniform optical constants in the  $z$ -direction, allowing for the solution of the vector Maxwell's equations in the form of coupled waves in the Fourier domain, and subsequent analysis of electromagnetic wave propagation. The matching of boundary conditions between layers is achieved through the use of scattering matrices, enabling the accurate solution of electromagnetic fields and the derivation of optical characteristics such as diffraction efficiency and spatial field distribution. As the RCWA solution process occurs in the Fourier domain, the device response is represented as a superposition of spatial harmonics. Frequency scanning is necessary when calculating the broadband characteristics of broadband devices.

For periodic structures like metasurfaces and photonic crystals, which exhibit spatial periodicity, RCWA can complete modeling and simulation within a limited number of Fourier spatial frequencies, demonstrating a significant computational efficiency advantage. However, when dealing with non-periodic structures in the  $xy$ -plane, such as porous or stochastic particle structures, RCWA requires the construction of a sufficiently large model to capture the statistical nature of these random structures, preventing local periodicity from distorting the calculation results. Moreover, the increased detail

**Table 2.** Simulation methods.

Method	2D/3D photonic crystal	Metasurface	Multilayer	Porous/fibrous structure	Random particle structure
Transfer matrix method (TMM)				✓	
Monte Carlo method (MCM)				✓	✓
Finite-difference-time-domain (FDTD)	✓	✓	✓	✓	✓
Rigorous-coupled-wave analysis (RCWA)	✓	✓	✓	✓	✓
Finite element method (FEM)	✓	✓	✓	✓	✓

in the model leads to a substantial rise in the number of harmonics required, which dramatically increases resource consumption and computation time. Although RCWA can still be used for modeling and computation of such structures, its efficiency may be inferior to other full-wave electromagnetic simulation techniques.

The finite-difference time-domain (FDTD) method is a widely utilized full-wave simulation technique for modeling the electromagnetic response of nanoscale structures and devices. FDTD discretizes space into subwavelength grids (Yee cells), with electric and magnetic fields sampled alternately on these grids: electric field components are located at the centers of cell edges, and magnetic field components are at the centroids of cell faces. This converts Maxwell's equations into a set of finite difference equations for numerical solution. The FDTD method, which does not introduce any physical approximations, offers high modeling precision. By increasing the accuracy of the grid division, the numerical simulation results can approach the theoretical values asymptotically. Moreover, as a time-domain model, FDTD can capture the broadband response characteristics of a device in a single simulation without the need for frequency scanning.

However, the FDTD method does not inherently optimize for specific device structures. Structures with periodic and non-periodic patterns, when using an equivalent number of Yee cells, consume nearly identical computational resources and time. Nevertheless, the requirement for subwavelength-scale grid sizes (typically less than 1/4 of the wavelength) presents significant challenges in terms of time cost and memory demand for large-scale device simulations. FDTD may, in certain cases, be more prone to convergence issues compared to other numerical methods. Factors such as excessively large grid sizes, inappropriate time step choices, incorrect boundary condition settings, and noise introduced by sources can prevent convergence. In contrast, the finite element method (FEM) solves partial differential equations (PDEs) using piecewise polynomial approximations, allowing for more flexible meshing and better adaptation to complex geometries and material properties, generally leading to better convergence.

The FEM is a versatile numerical technique used to address problems in electromagnetic field, solid mechanics, fluid dynamics, thermal conduction, etc. The essence of FEM is to decompose complex geometric shapes and boundary conditions into simpler subdomains and to solve approximate numerical solutions of PDEs within these subdomains.

Specifically, FEM divides the region of interest into a finite number of elements, forming interconnected meshes, typically comprising free triangular or tetrahedral networks in two and three-dimensional simulation spaces. By multiplying the PDEs with appropriate test functions via the variational principle, the equations are transformed into integral equations in a less stringent form. This alternative formulation allows for problem-solving within continuous media, albeit with reduced precision. Boundary and source conditions are incorporated into the global FEM linear equations of the entire network, usually in the form of sparse matrices, through surface and volume integrals. Solving this system of equations with numerical methods such as iterative or direct methods yields numerical solutions for post-processing.

The FEM is not only applicable to the solution of electromagnetic field problems but also to any continuous physical or multiphysics field problems that can be discretized. The unique advantage of FEM lies in its ability to tackle convergence issues that may plague other electromagnetic simulation methods. With sufficient computational resources, FEM can directly solve a vast number of PDEs corresponding to finely discretized free meshes, thereby addressing any multiphysics problem for arbitrary geometric configurations. Consequently, for complex physical field problems or intricate and precise structural models, FEM might be the only viable approach.

The selection of full-wave electromagnetic field simulation methods should be customized to suit the specific demands of the problem at hand, ultimately resulting in a more refined solution.

The simulation methods used for optimizing specific types of radiative cooling materials are summarized in table 2. It is important to note that the table merely indicates the applicability of different simulation methods to the design of specific structures. A detailed discussion on the preference for specific simulation methods to economize computational resources and time for individual structure design will follow in the subsequent text.

### 3.2. Design of periodic photonic structures

Advancements in design and fabrication techniques have catalyzed the rapid progression of photonic approaches in the realm of efficient radiative cooling, particularly in the area of sub-ambient daytime radiative cooling. This method permits the modification of the optical properties of composite materials by implementing periodic structures such as photonic

crystals [7, 15, 116, 117] or metasurfaces [8, 118], which can alter the effective dielectric constant, enhance periodic resonances, or form photonic bandgaps, thereby transforming the spectral radiative characteristics of radiative cooling devices. This ingenious approach opens up a multitude of possibilities for augmenting radiative cooling capabilities and offers a novel and effective solution for temperature management and energy efficiency across various applications. At the design stage, the modeling of periodic structures is particularly amenable to RCWA methods, and even computationally intensive methods such as FDTD and FEM simulations require relatively modest computational resources and time.

**3.2.1. Photonic crystal.** Within the domain of artificial materials, photonic crystals stand out for their mesoscopic-scale periodic distribution of dielectric constants. What sets them apart is the presence of photonic bandgaps, akin to the energy band structure in electronic crystals, which prohibit the propagation of light within specific wavelength ranges. By finely tuning the periodic parameters, the position and width of the photonic bandgaps can be manipulated, allowing for high-efficiency and finely tuned spectral control. This attribute positions photonic crystals as an ideal candidate for fulfilling the selective spectral modulation requirements of daytime radiative cooling devices. At the design level, 1D photonic crystals, which are essentially multilayer film structures, can be effectively simulated using the TMM with minimal computational time and resource usage. For 2D and 3D photonic crystals, full-wave electromagnetic simulations are employed, facilitated by the introduction of periodic boundary conditions, with the RCWA method being particularly advantageous for modeling and computation.

In 2013, Fan's team at Stanford University proposed a novel composite photonic structure for daytime radiative cooling [7]. This design ingeniously integrates a one-dimensional chirped photonic crystal composed of magnesium fluoride ( $MgF_2$ ) and titanium dioxide ( $TiO_2$ ) with a two-dimensional photonic crystal made of silicon carbide (SiC) and quartz, utilizing silver (Ag) as the bottom reflector (figure 9(a)). The structure achieves high reflectivity in the solar radiation spectrum (0.3–2.5  $\mu m$ ) and high emissivity in the two MIR atmospheric transparency windows at 8–13  $\mu m$  and 16–25  $\mu m$ , theoretically predicting exceptional radiative cooling performance.

In 2015, Fan's team developed a photonic crystal thermal blackbody for PV cooling [15]. This thermal blackbody exhibits high transmissivity in the solar spectrum and high emissivity in the infrared spectrum. The structure is composed of a square-lattice photonic crystal with a periodicity of 6  $\mu m$ , fabricated by etching 10  $\mu m$ -deep air holes into a 500  $\mu m$ -thick double-side-polished fused silica wafer. Compared to a bare silicon wafer, this material can achieve an additional 13 °C temperature reduction for solar cells during the daytime.

In 2018, a simple and low-cost radiative cooler based on one-dimensional photonic crystals was reported [117], exhibiting an average emissivity of 96% within the ATSW (8–13  $\mu m$ ). The ultra-broadband emissivity property was

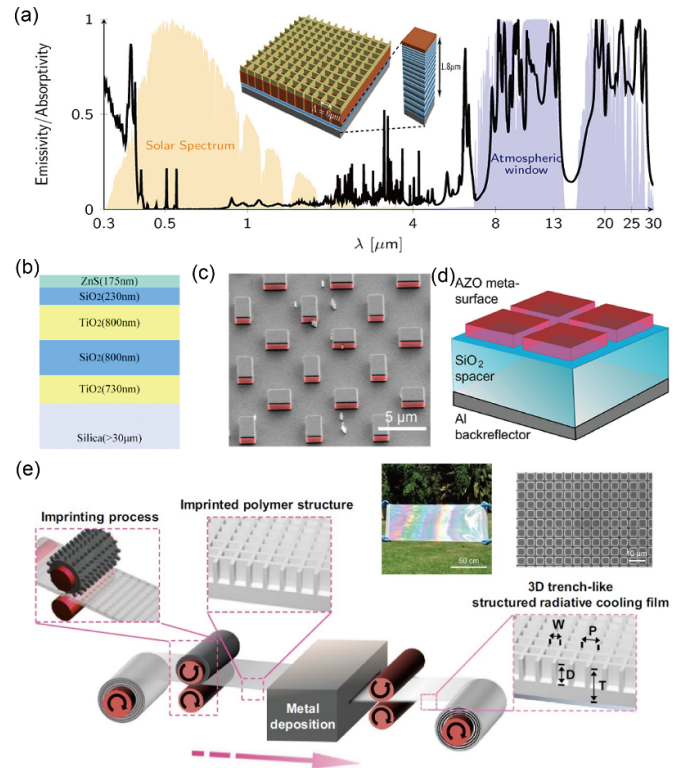


**Figure 9.** PDRC devices based on periodic photonic structures. (a) Composite photonic crystal PDRC device. Reprinted with permission from [7]. Copyright (2013) American Chemical Society. (b) Radiative cooler based on one-dimensional photonic crystal structure. Reprinted with permission from [117] © Optical Society of America. (c) Dielectric resonator radiative cooling metasurface. [8] John Wiley & Sons. © 2017 WILEY-VCH Verlag GmbH & Co. KGaA, Weinheim. (d) AZO-based radiative cooling metasurface. Reprinted with permission from [118]. Copyright (2018) American Chemical Society. (e) Flexible polymer PDRC metasurface prepared in batches using roll-to-roll process. Reproduced from [11]. CC BY 4.0.

achieved through a tandem structure composed of two lossy materials,  $SiO_2$  and  $TiO_2$ , which constructed strongly overlapping optical resonances (figure 9(b)). An additional lossless material,  $ZnS$ , was used as the top layer to minimize the Fresnel reflection across the entire structure, demonstrating exceptional angular insensitivity and radiative cooling capability.

**3.2.2. Metasurface.** The subwavelength characteristics and the high degree of structural design freedom of metasurfaces [8, 11, 118–121] offer a viable solution for further enhancing the spectral modulation efficiency of daytime radiative cooling devices and for achieving a thinner device design. If the metasurface is a two-dimensional periodic structure, the design typically involves the RCWA as the preferred method for modeling individual periodic atoms. In cases where the metasurface is composed of diverse types of atoms, thereby disrupting the periodicity, the FDTD and FEM become more suitable for simulation.

In 2017, Fumeaux's team at Adelaide University fabricated a dielectric resonator (DR) metasurface composed of doped n-type silicon (Si) and silver (Ag), as depicted in figure 9(c) [8]. This metamaterial leveraged the dipole resonances supported by Si particles to effectively modulate the emissivity within ATSWs.

In 2018, the Muskens team at Southampton University designed a transparent conductive oxide (TCO) metasurface based on aluminum (Al) doped zinc oxide ( $\text{ZnO}$ ) [118]. The metasurface, comprising a metallic reflector, a dielectric spacer, and an AZO layer (figure 9(d)), achieved a low solar absorption of 0.16 and a high infrared thermal radiation emissivity of 0.79, thereby facilitating radiative cooling for spacecraft applications.

Moreover, the use of phase-change materials such as vanadium dioxide ( $\text{VO}_2$ ) to construct radiative cooling metasurfaces for dynamic regulation has emerged as a recent research trend. For instance, in 2023, Estakhri *et al* proposed a design of dual nanophotonic structures, which incorporate phase-change material ( $\text{VO}_2$ ) and a layer of TCO (aluminum-doped zinc oxide, AZO) to form the metasurface [120]. Each design features a thin layer of unpatterned or patterned  $\text{VO}_2$  to facilitate thermal switching between the desired hot state ( $T > 68^\circ\text{C}$ ) and cold state ( $T < 68^\circ\text{C}$ ). The structure achieves high reflectivity across the solar spectrum (0.4–2.5  $\mu\text{m}$ ) and high absorption within the thermal atmospheric transparent window (8–13  $\mu\text{m}$ ). Owing to its inherent compactness and passive, adaptive properties, this planar structure shows great potential for applications in radiative cooling of electronic devices and spacecraft.

In 2024, Li *et al* adopted a  $\text{VO}_2$ -based metasurface strategy to design and fabricate a temperature-adaptive metasurface radiative cooling device (ATMRD) [121]. Through sophisticated metasurface design, the device not only significantly enhanced the emissivity performance but also markedly reduced the solar absorption rate, effectively addressing the mutual constraint between low solar absorption and high thermal infrared emissivity in traditional designs. Compared to conventional adaptive thermal radiative devices (ATRDs), the ATMRD achieved a 7.54% reduction in solar absorption rate and a 13.3% increase in high-temperature emissivity. The designed ATMRD exhibits outstanding dynamic radiative thermal management capabilities.

However, photonic radiators still face several challenges that have hindered the widespread adoption and practical application of the research findings in this area. The manufacturing process, particularly for 3D radiators, demands a high level of precision, making the cost of photonic radiators a significant barrier to practical applications. Additionally, the current limitations in achieving large-scale production are due to the complexity of the processes and the availability of the necessary facilities. Consequently, photonic radiators remain in an early stage of development, primarily confined to laboratory research and exploration. In recent years, the advancements in polymer printing technologies based on roll-to-roll (R2R) processes have made the large-scale batch production of ordered daytime radiative cooling devices feasible [11], as

illustrated in figure 9(e). Nevertheless, the realization of the batch production of more complex structures still depends on the further development of related manufacturing techniques.

### 3.3. Design of aperiodic photonic structures

The strict translational symmetry inherent in periodic configurations poses a challenge in engineering applications. Aperiodic structures, leveraging their statistical properties, can achieve broadband responsiveness with insensitivity to incident angles. Common aperiodic examples in radiative cooling materials include aperiodic multilayer film structures, randomly distributed micro- and nanoparticles, and porous structures. Radiative cooling devices with random photonic structures are characterized by their low cost and ease of mass production. For stochastic photonic structures, the modeling via full-wave electromagnetic simulations necessitates an adequately large model size to ensure that the optical statistical properties of the composite materials encompass the randomness of their local distributions, thereby minimizing errors. This typically entails a substantial investment of computational resources and time. Therefore, when feasible, employing more resource-efficient methods such as EMT or the MCM to calculate a subset of the spectral bands, rather than conducting full-wave electromagnetic simulations across the entire spectrum, can significantly conserve memory space and reduce computational time.

**3.3.1. Aperiodic multilayer film.** In the realm of optics, thin film design frequently turns to empirical structures such as symmetric multilayer stacks, periodic configurations, and quarter-wave stacks. The incorporation of non-periodic multilayer designs within the domain of radiative cooling has substantially broadened the application landscape for optical thin films. Notably, multilayer dielectric photonic structures, which harness the broadband absorption of metal-oxygen bonds, are capable of achieving high infrared emissivity, opening up new avenues for the design and application of thin film optics. Despite being classified as aperiodic, the multilayer film exhibits uniform medium properties within the  $x$ - $y$  plane for each layer, thereby rendering the design approaches and advantages of periodic structures applicable to aperiodic multilayer films. Consequently, the TMM remains the optimal simulation technique for such multilayer film structures.

In 2014, Fan *et al* further streamlined the structural design and developed a photonic film composed of multiple layers of films, which was the first to experimentally observe a radiative cooling effect below ambient temperature under intense direct sunlight during the daytime [5]. As shown in figure 10(a), the daytime radiative cooling device consists of seven alternating layers of different thicknesses of hafnium dioxide ( $\text{HfO}_2$ ) and silicon dioxide ( $\text{SiO}_2$ ), with a 200 nm Ag layer at the bottom, capable of reflecting 97% of solar radiation and exhibiting high emissivity in the atmospheric window at 8–13  $\mu\text{m}$ . Under direct sunlight with an intensity exceeding 850  $\text{W m}^{-2}$ , the device achieved a temperature drop of 4.9  $^\circ\text{C}$ . This research is

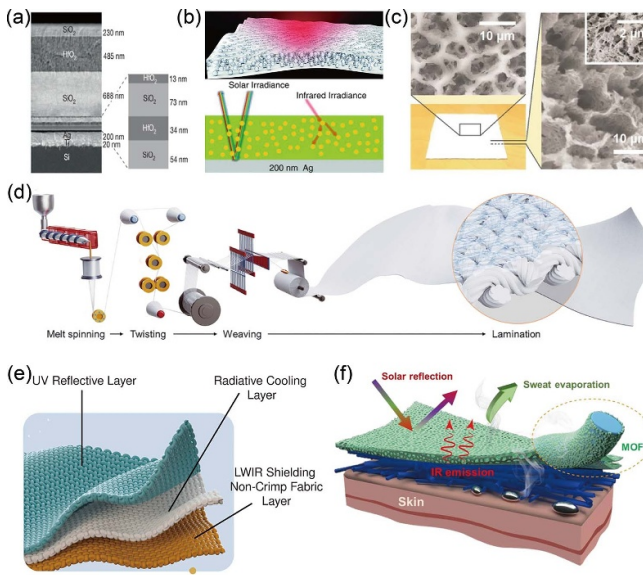


**Figure 10.** PDRC devices based on aperiodic photonic structures. (a)  $\text{HfO}_2\text{-SiO}_2$  multilayer film structure. Reproduced from [5], with permission from Springer Nature. (b) Random glass-polymer hybrid metamaterial film. From [6]. Reprinted with permission from AAAS. (c) Hierarchically porous polymer coatings. From [9]. Reprinted with permission from AAAS. (d) Hierarchical-morphology metafabric. From [122]. Reprinted with permission from AAAS. (e) Dual mode Janus fabrics. Reproduced from [104]. CC BY 4.0. (f) Hierarchically nanostructured cellulosic wearable metafabric. Reprinted from [10], Copyright (2024), with permission from Elsevier.

considered a groundbreaking achievement in the field of daytime radiative cooling.

In 2020, the Lee's group designed a four-layer membrane structure for daytime radiative cooling [123]. The membrane structure is composed of aluminum oxide ( $\text{Al}_2\text{O}_3$ ), silicon nitride ( $\text{Si}_3\text{N}_4$ ),  $\text{SiO}_2$ , and Ag, and the thickness and stacking order of each layer were adjusted using the particle swarm optimization algorithm. In the range of  $8\text{--}13\ \mu\text{m}$ , the membrane structure achieved an average emissivity of 87%, while its average absorption in the solar radiation spectrum was 5.2%. Under direct sunlight, the membrane structure was able to reduce the temperature by up to  $8.2\ ^\circ\text{C}$ .

**3.3.2. Random particles.** By doping polymers with inorganic particles, the spectral requirements of daytime radiative cooling devices can be effectively met. The doping of inorganic micro- and nanoparticles, through their strong scattering of sunlight [124] or the phonon polariton resonance in the MIR band [125], not only enhances the solar radiation reflectivity but also improves the MIR emissivity of daytime radiative cooling devices. Over the past decade, including  $\text{SiO}_2$  [6, 126–129],  $\text{TiO}_2$  [16, 17, 130, 131],  $\text{Al}_2\text{O}_3$  [132, 133],  $\text{ZnO}$  [134],  $\text{BaSO}_4$  [135], and other nanoparticle or microparticle dopants have been widely utilized and have achieved significant spectral modulation effects in the solar radiation and

MIR thermal radiation bands. In composite radiative cooling materials, the particle sizes of common dopants typically range from hundreds of nanometers to micrometers, which is comparable to the wavelengths of interest in the radiative cooling domain, spanning from 0.3 to 25 micrometers. Specifically in the infrared region, the random particles or air voids in aperiodic structures are typically much smaller than the wavelengths, making them suitable for refractive index fitting using the EMT and subsequent computational simplification with the TMM. In the solar spectral range, given that the doping concentration usually does not exceed 20% by volume [6], these conditions meet the size and non-interference criteria for the application of the MCM. However, if the particle sizes are not well-matched or if the concentration of random particles is too high, leading to significant interparticle interactions that cannot be ignored, the MCM becomes inapplicable. In such cases, full-wave electromagnetic simulation emerges as the only viable option.

In 2017, Yin and Yang at Colorado University developed a glass-polymer composite metamaterial by randomly embedding resonant polar dielectric microspheres ( $\text{SiO}_2$ ) into polymethylene (TPX), as depicted in figure 10(b) [6]. This material controls the thermal radiation performance of the metamaterial in the MIR band by adjusting the diameter of the microspheres (thickness  $50\ \mu\text{m}$ , emissivity  $>0.93$ ), and due to the roll-to-roll fabrication process, the composite metamaterial can be mass-produced. With Ag at the bottom to reflect sunlight, the metamaterial exhibited a radiative cooling power of  $93\ \text{W m}^{-2}$  at noon.

In 2022, a PDRC coating by embedding  $\text{Y}_2\text{O}_3/\text{TiO}_2$  particles into polydimethylsiloxane (PDMS) polymer [17] was developed. The uniformly dispersed  $\text{TiO}_2$  and  $\text{Y}_2\text{O}_3$  particles resulted in a solar reflectance of 92.2%.

In 2023, an organic-inorganic tandem structure combining polyether sulfone (PES),  $\text{Al}_2\text{O}_3$ , and  $\text{TiO}_2$  was developed. PES was chosen for its high solar reflectance and thermal emissivity, while  $\text{Al}_2\text{O}_3$  nanoparticles offered UV reflection and superhydrophobic properties. The addition of  $\text{TiO}_2$  provided comprehensive UV protection, self-cleaning capabilities, and significantly enhanced cooling performance [16]. This PES- $\text{Al}_2\text{O}_3\text{-TiO}_2$  cooler exhibited an ultra-high solar reflectance of over 97% and a high MIR emissivity of 0.92. Notably, despite PES's sensitivity to UV radiation, these optical properties did not diminish even after 280 d of equivalent UV exposure.

**3.3.3. Porous polymer structure.** The operation mechanism of porous material relies on the presence of numerous randomly distributed pores of varying sizes within its interior, which scatter solar radiation while effectively reducing material absorption during electromagnetic wave propagation, leading to high solar reflection. Moreover, polymers, due to their solubility differences in various solvents, possess a unique advantage in the fabrication of porous structures. Many polymers, with specific molecular bonds or functional groups, exhibit vibrational frequencies that align with ATSWs, thereby enhancing radiative cooling capabilities [136]. Consequently,

polymers with high MIR emission, combined with porous structures that exhibit high solar reflection, can achieve superior daytime radiative cooling performance. Porous structures can be regarded as random particle structures with air voids as the dopant particles, typically simulated using full-wave electromagnetic methods. Radiative cooling materials based on porous structures often exhibit porosities exceeding 50% [9]. When employing the MCM for simulation, it may be challenging to meet the low-concentration doping criteria, leading to potential inaccuracies; however, it still serves as a valuable theoretical reference. Additionally, it is noteworthy that the pore size distribution in aerogel materials is often on the order of tens of nanometers, which is much smaller than the wavelength of light, allowing for the use of the EMT for calculation.

In 2018, Yang and Yu at Columbia University developed a poly(vinylidene fluoride-co-hexafluoropropylene) porous coating [P(VdF-HFP)HP] using a phase inversion process, as illustrated in figure 10(c) [9]. This coating demonstrated exceptional spectral control for daytime radiative cooling without the need for a metallic reflector. The porous coating possesses a solar reflectance of 0.96 and an infrared emissivity of 0.97, and it exhibited a cooling effect of approximately 6 °C below the ambient temperature in thermal tests that accounted for air convection. Moreover, this polymer coating is easily applicable by spraying onto various surfaces, offering good durability and even colorability. These attributes make it a promising candidate for widespread use as a high-performance passive radiative cooling material.

In 2020, Lee's group utilized light-induced free radical polymerization to prepare PVDF-polyurethane acrylate (PUA) coatings, resulting in a uniform porous structure [18]. Owing to the porous PVDF-PUA material's solar reflectance of up to 0.9336 and its infrared emissivity in the atmospheric window due to vibrations such as C–C, C–F, C–O, and C backbone, the prepared coatings exhibit efficient daytime radiative cooling properties.

In 2021, a hierarchical porous PMMA film [19] was developed. This film integrates periodic arrays of micropores with randomly distributed nanopores, achieving refrigeration below ambient temperature during both nighttime (approximately 8.2 °C) and daytime (approximately 6.0 °C–8.9 °C).

In 2023, a porous metafoam composed of polycarbonate (PC) and PDMS for daytime radiative cooling was produced [20]. The structure achieved a high solar reflectance of 0.97, an infrared emissivity of 0.91, and a low thermal conductivity of 46 mW (m K)<sup>-1</sup>, and its energy-saving capabilities for assisting building cooling systems were validated through computational analysis.

**3.3.4. Fiber-textile structure.** In engineering practice, the integration of passive radiative cooling technology into textiles is emerging as a simple, cost-effective, and energy-saving strategy for personal thermal comfort, with various implementation methods corresponding to different physical mechanisms.

One strategy entail boosting the solar reflectance of conventional commercial fabrics by integrating them with additional components, which involves introducing randomly dispersed inorganic particles either on the fabric surface or within the fiber matrix.

A notable example of this approach is the development of a hierarchical meta-fabric by Tao and Ma in 2021 [122]. This meta-fabric is woven from polylactic acid (PLA) microfibers embedded with titanium dioxide particles and features a thin ultraviolet protective layer of polytetrafluoroethylene (PTFE) on the outer surface, addressing both internal fiber and external fabric surface design. Outdoor experiments have demonstrated that this meta-fabric covers the human body at a temperature approximately 4.8 °C lower than that of commercial cotton fabrics (figure 10(d)). Building upon the concept of hierarchical and graded design, in 2024, Ma *et al* introduced a dual-mode (DM) radiative thermal management fabric based on fiber and weaving structures (figure 10(e)) [104].

In 2023, inspired by the efficient optical properties and water-resistant, breathable structure of human skin's epidermal and dermal layers, a bio-metafabric with superior optical properties, good breathability, durability, and flexibility was developed [137]. Using a simple and scalable dyeing process, they encapsulated optical microparticles (such as SiO<sub>2</sub>, BaSO<sub>4</sub>, TiO<sub>2</sub>, etc.) on a commercial cotton-polyester fabric substrate with polyvinylidene fluoride (PVDF), creating a random particle structure system, and produced a bio-metafabric with 97% solar reflectance and 97% emissivity in the atmospheric window. Outdoor tests revealed that the bio-metafabric's temperature was significantly lower than that of white fabrics like nonwoven, polyester, and linen available in the market, achieving an average cooling effect of 5.2 °C below the ambient temperature during the day. Wearing a hat made of bio-metafabric resulted in a 5.0 °C lower temperature on the top of the head compared to wearing a white cotton hat. The bio-metafabric has the potential for wide application in outdoor tents, car covers, and other fields.

In an alternative approach, advanced fabrication techniques such as electrospinning are utilized to produce micro/nanofiber structured textiles. The micro/nanofiber structure can be regarded as a specialized type of porous structure, sharing the characteristic of high porosity with conventional porous materials. The fibers, ranging in diameter from nanometers to micrometers, act as efficient scattering structures for sunlight, thereby achieving high solar reflectance. Moreover, the molecular bond vibrations of the polymer within these fibers contribute to a high MIR emissivity, making this structure ideal for daytime radiative cooling.

In 2023, Tang and Wang drew inspiration from the microstructure of silk cocoons to develop a nanofibrous silk fabric using an electrospinning technique, which features a pure silk fibroin matrix and excellent passive cooling capabilities [138]. The meticulously designed fibers with a broad diameter distribution enable the fabric to effectively scatter sunlight across the 0.3–2.5 μm wavelength range, achieving a high weighted reflectance of 95%. For the ultraviolet light range (0.3–0.42 μm), the reflectance is also as high as 92%. Outdoor

tests have demonstrated that this fabric can lower the temperature by 3.8 °C during the day and 6.4 °C at night, respectively, below the ambient environmental temperature.

Additionally, as an excellent compatibility platform, random particle structures, porous structures, and micro/nano-fiber structures can work synergistically on the fabric substrate. In 2024, Fu *et al* developed a sustainable, cost-effective, super-durable, and nanostructured cellulosic meta-fabric (CWF) (figure 10(f)) [10]. Polyurethane was utilized to enhance the flexibility and mechanical properties of cellulose acetate, while the doping of ZIF-8 nanoparticles improved the material's visible light scattering capability. Finally, by employing an electrospinning technique, the composite solution was spun into a porous radiation-cooling super-fabric, the CWF. This fabric achieved 95.7% solar reflectivity, 0.94 infrared emissivity, high mechanical strength, washability, surface hydrophobicity, and UV resistance. This metafabric demonstrated a high cooling efficiency of 5.7 °C under direct sunlight in summer, along with anti-washing and UV stability.

The fiber-textile structure is inherently complex, necessitating the use of full-wave electromagnetic simulations for accurate analysis. However, as discussed in this subsection, depending on the engineering implementation, the fiber-textile structures can often be approximated as random particle structures or porous structures. In such cases, the MCM or the EMT can be employed as auxiliary assessment tools, allowing for a rough determination of the textile material's optical properties with fewer computational resources. In conclusion, for composite radiative cooling materials, the choice of simulation method should be carefully considered, taking into account the structural characteristics, the scale of material composition, and the operational wavelength range.

## 4. Progress and applications of radiative cooling technology

### 4.1. Radiation cooling devices for multi-scenario

As previously discussed, over the past decade, a wide range of radiative cooling devices with various structural designs have been realized. Radiative cooling devices have evolved from their initial laboratory-scale fabrication, validation, and theoretical studies of light control to large-scale batch production and application research. In this section, we will focus on the temperature control of radiative cooling devices and outline their applications in several areas, including cooling and energy saving in indoor spaces of buildings, PTM, PV cooling, and energy and water harvesting.

**4.1.1. Energy-efficient building.** Buildings, serving as the venues for human labor and habitation, consume a substantial amount of energy for the purpose of thermal management within their interiors. The capability to modulate the emissivity of building surfaces to facilitate radiative cooling during the

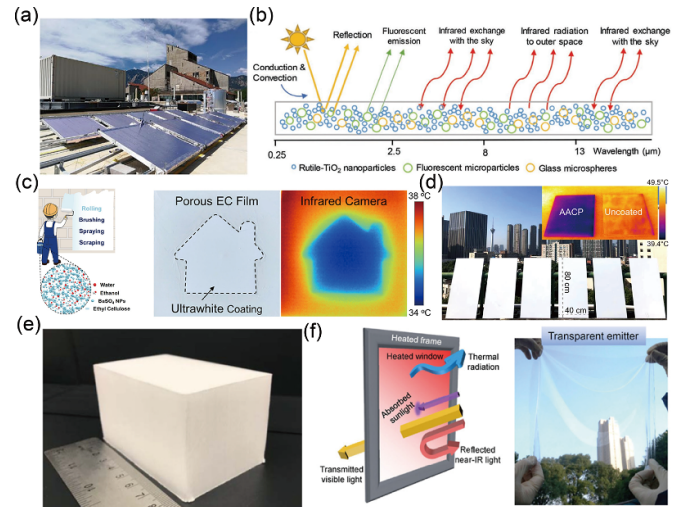


**Figure 11.** Radiative cooling materials for architectural applications. (a) PDRC water cooling module (RadiCool module) for energy saving in air conditioning systems. Reprinted from [24], Copyright (2019), with permission from Elsevier. (b) Schematic diagram of the cooling mechanism of the self-adaptive sub-ambient daytime radiative cooling (SDRC) coating. [139] John Wiley & Sons. © 2020 Wiley-VCH GmbH. (c) Schematic, photograph, and infrared image of the ethyl cellulose (EC)-BaSO<sub>4</sub> coating. Reprinted with permission from [22]. Copyright (2022) American Chemical Society. (d) The anti-aging cooling paint. Reproduced from [23]. CC BY 4.0. (e) Structured cooling wood. From [21]. Reprinted with permission from AAAS. (f) Transparent cooling window. Reproduced with permission from [140]. CC BY-NC-ND 4.0.

summer months could yield substantial energy-saving benefits for these structures.

Given that the roofs and side walls of most buildings feature large areas of flat surfaces, coatings [9, 141] or thin film [6, 11] structures can readily be integrated with the building to achieve spectral modification of the roof or exterior wall, thereby directly reducing the thermal load from the environment [142]. Further, daytime radiative cooling devices can also contribute to energy savings by providing cooling power for air conditioning systems. In 2019, Yang *et al* at Colorado University developed a PDRC water cooling module (RadiCool module) using the team's previously proposed composite metamaterial for daytime radiative cooling [6], as illustrated in figure 11(a). This module is capable of continuously producing chilled water below ambient temperature, which is used for cooling the air conditioning condenser [24]. The experimental radiative cooling system (RadiCold system) can provide a power of 607 W during the daytime and can reach up to 1296 W during the nighttime. By incorporating a water storage device, the system can also avoid wasting cooling power when cooling is not required. In 2020, Dai *et al* developed a building coating composed of a styrene-acrylic emulsion as the matrix material, supplemented with TiO<sub>2</sub> rutile powder, glass microspheres, and fluorescent pigments (SrAl<sub>2</sub>O<sub>4</sub>:Eu<sup>2+</sup>, Dy<sup>3+</sup>, Yb<sup>3+</sup>) as fillers (figure 11(b)) [139]. This coating exhibits good workability, making it easy to

mix and apply to building surfaces. Notably, the incorporation of fluorescent pigments has the potential to convert sunlight below 450 nm that is absorbed into visible fluorescent emission, thereby enhancing the effective solar reflectance of  $\text{TiO}_2$ . In 2022, Hu's team developed an eco-friendly high-performance super-white coating composed of a porous ethyl cellulose (EC) matrix, a water/ethanol green solvent, and irregular  $\text{BaSO}_4$  nanoparticles ( $\text{BaSO}_4$  NPs) and applied it to the field of building refrigeration (figure 11(c)) [22]. Even under high humidity conditions and direct sunlight exposure, this coating can significantly reduce the sub-ambient temperature. In 2022, Zhang *et al* developed a graded porous anti-aging radiative cooling coating composed of hydrophobic  $\text{TiO}_2$  nanoparticles (figure 11(d)) [23]. After simulating three years of natural pollution and one year of sunlight exposure, the coating's solar reflectance decreased by only 0.4% and 0.5%, demonstrating excellent long-term stability.

Materials such as wood and tiles also possess the potential to serve as radiative cooling materials. In 2019, Hu's team at Maryland University developed a wood-based radiative cooling material with daytime radiative cooling functionality [21] (figure 11(e)). Leveraging the molecular vibrations, stretching, and the neatly arranged fiber structure of cellulose, this wood can effectively scatter incident sunlight and enhance its infrared emissivity. It possesses excellent mechanical properties, making it suitable for direct use as a building material. In 2023, Tso's group prepared an  $\text{Al}_2\text{O}_3$  porous cooling ceramic using phase inversion and sintering techniques [143]. The ceramic had a solar reflectance of 0.996 and could achieve over  $130 \text{ W m}^{-2}$  of cooling power during the daytime. The Hu's team at Maryland University obtained a porous radiative cooling glass doped with nano- $\text{Al}_2\text{O}_3$  particles using a partially sintered method [144]. This structure achieved a solar reflectance greater than 0.96 and an infrared emissivity of about 0.95, achieving cooling of about  $3.5^\circ\text{C}$  in high humidity environments. Compared to the polymer-based strategy, the above two daytime radiative cooling devices composed of pure inorganic oxides have better mechanical strength and stronger long-term weather resistance, making this strategy more suitable for cooling and energy-saving in buildings.

Radiative cooling materials can also be applied to energy-saving windows to maintain the desired transparency of the windows (visible band,  $0.38\text{--}0.76 \mu\text{m}$ ) while improving their performance in the near-infrared (NIR,  $0.76\text{--}2.5 \mu\text{m}$ ) and MIR (MIR,  $0.3\text{--}2.5 \mu\text{m}$ ) bands. In 2020, Zhou *et al* proposed a strategy to enhance the energy efficiency of building thermal management by modulating the spectral characteristics of windows [140]. By introducing a dual-layer coating structure with a high-MIR emissive outer layer (PDMS) and a near-infrared reflective inner layer (indium tin oxide, ITO) (figure 11(f)), it can effectively reduce the input of ineffective solar energy and promote its own thermal radiation. Experimental results show that compared to general near-infrared reflective windows, this strategy can achieve a cooling of approximately  $7^\circ\text{C}$ . In 2022, a plasmonic meta-glass design using a two-dimensional hexagonal array of tungsten nanorings was proposed, blocking approximately 87% of infrared

radiation in the  $750\text{--}1800 \text{ nm}$  range and maintaining 60% visible light transmission for indoor illumination [145]. In 2024, Richards *et al* proposed a polymer-based microphotonic multi-functional metamaterial [146]. Compared to traditional glass, this metamaterial can scatter 73% of sunlight while maintaining a higher visible light transmittance, creating a more comfortable private environment and possessing self-cleaning properties. Due to its extremely high emissivity ( $\sim 0.98$ ) in the MIR thermal radiation band, the metamaterial can provide approximately  $97 \text{ W m}^{-2}$  of cooling power at ambient temperature. Although numerous excellent works exist, it has been observed that there is a limited number of studies that have truly achieved independent tri-band modulation [147]. The endeavor to realize modulation across such a broad spectral range ( $0.38\text{--}20 \mu\text{m}$ ) using a single structure presents significant challenges. Moreover, as consumer demands for energy-saving windows become increasingly diverse, the single function of cooling alone can no longer meet the market needs [148]. The future research focus will be on the development of multi-functional smart windows that integrate technologies for intelligent response, power generation, and energy storage. For example, Xu *et al*'s ESEG smart window, integrating louver solar cells, thermotropic hydrogel, and ITO glass, achieves 90% luminous transmission and 54% solar modulation, with an 18.24% photoelectric efficiency paving a new path for multi-functional integration including energy storage and saving [149].

#### 4.1.2. PTM.

PTM is of critical importance to human comfort and health in daily activities. Outdoor workers and sports enthusiasts often need to be exposed to high temperatures, which can lead to health issues related to heat. In outdoor environments, strategies for thermal management of open spaces are highly inefficient, and textile-based human body radiative cooling technology is considered an attractive approach [150–152]. Traditional textiles lack the design for optical bands (solar radiation and MIR thermal radiation bands), making it difficult to achieve efficient indoor/outdoor thermal management. In recent years, various thermal management textiles for human body radiative cooling have been proposed to meet the demands of personal thermal comfort.

In 2016, Cui *et al* at Stanford University first experimentally realized an indoor PTM textile based on nanoporous PE (nanoPE) (figure 12(a)) [150]. Due to the internal voids within the textile being similar in size to the wavelengths of visible light, it can strongly scatter visible light, making the textile opaque and providing privacy. The voids are much smaller than the wavelengths of MIR thermal radiation, allowing human body radiation to directly pass through the fabric into the environment, achieving a cooling effect on the human body under indoor conditions. To improve the wearability of nanoPE, they achieved the bulk preparation of nanoPE fibers in 2018 based on the melt extrusion process (figure 12(b)) [153]. When applied to human skin indoors, the fabric based on these fibers can achieve a cooling effect of approximately  $2.3^\circ\text{C}$ .

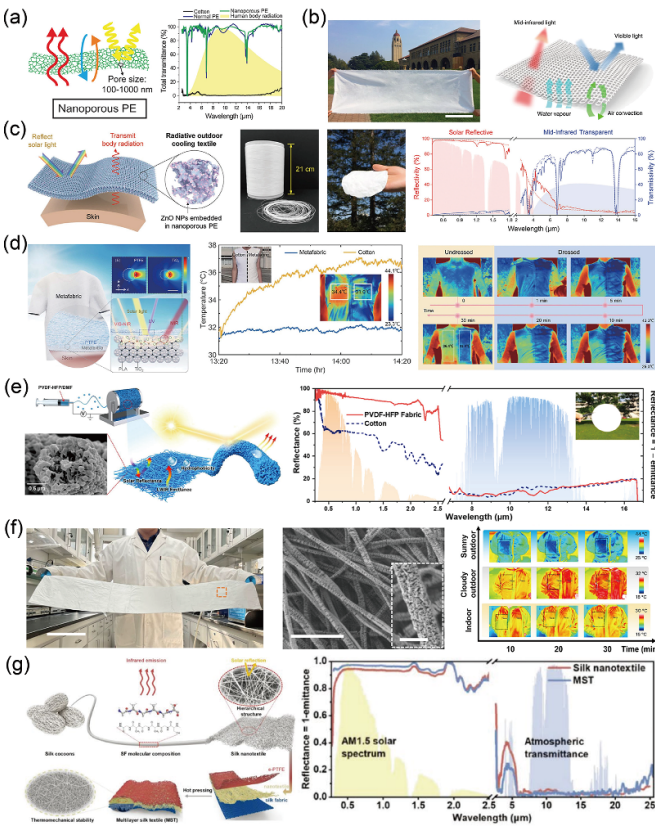


**Figure 12.** Radiative cooling materials for personal thermal management. (a) Schematic of the infrared (FTIR) transmission spectrum and the Fourier transform infrared (FTIR) transmission spectrum of nanoporous polyethylene (PE) textiles. From [150]. Reprinted with permission from AAAS. (b), Photographs and radiative cooling principles of nanoporous PE textiles. Reprinted with permission from reference. Reproduced from [153], with permission from Springer Nature. (c) Schematic of ZnO nanoparticle-embedded nanoporous PE textiles and the corresponding solar reflectance and infrared transmittance. [154] John Wiley & Sons. © 2018 WILEY-VCH Verlag GmbH & Co. KGaA, Weinheim. (d) Schematic of the multilayer morphological superstructure, real-time temperature profiles, and infrared images. From [122]. Reprinted with permission from AAAS. (e) Preparation process diagram of the multistage porous polyvinylidene fluoride-co-hexafluoropropylene (PVDF-HFP) textiles and the corresponding solar reflectance. Reprinted from [155], Copyright (2023), with permission from Elsevier. (f) Photographs, scanning electron microscopy (SEM) images, and outdoor cooling performance of the all-weather radiative cooling polyoxymethylene (POM) textiles. Reproduced from [156], with permission from Springer Nature. (g) Multilayer silk textile (MST) for radiative cooling. [157] John Wiley & Sons. © 2023 Wiley-VCH GmbH.

To achieve human body radiative cooling in outdoor environments, the team further introduced infrared-transparent ZnO nanoparticles into the nanoPE structure (figure 12(c)), maintaining high transmittance in the MIR band while achieving sunlight reflection [154]. This structure finally achieved a solar radiation reflectance of greater than 0.9, compared to commercial textiles, it could cool the simulated skin by 5 °C–13°C.

In addition to achieving high MIR transmission, another strategy for achieving human body radiative cooling is to have

textiles with high MIR emissivity. This strategy removes constraints on the thickness of the fabric and the choice of materials, making it easier to achieve high reflectivity in the solar radiation band through photonic structure design. Therefore, it is highly suitable for human body radiative cooling in outdoor environments with direct sunlight. Currently, various structures that can be used for outdoor human body radiative cooling, including electrospun films [155–158] and leather [159], have been proposed successively.

In 2021, Zeng *et al* developed a hierarchical meta-fabric [122]. This meta fabric is woven from PLA microfibers embedded with titanium dioxide particles, with a thin ultraviolet protective layer of PTFE attached to the outer surface, designed for PTM. Outdoor experiments have shown that this meta fabric covers the human body at a temperature about 4.8 °C lower than commercial cotton fabrics (figure 12(d)). Also in 2021, Zhu *et al* achieved nano structural modification of commercial silk through molecular bonding design and an impregnation-pulling process, successfully introducing a large number of Al<sub>2</sub>O<sub>3</sub> nanoparticles onto its surface to enhance its ultraviolet reflection performance [160]. The fabricated radiative cooling fabric could achieve a temperature reduction of approximately 3.5 °C below ambient temperature under direct sunlight. In 2023, Wang and colleagues utilized a vapor-induced phase separation technique to prepare a nano laminated porous fabric of PVDF-co-hexafluoropropylene (HFP) [155]. The resulting PVDF-HFP fabric exhibited an average solar reflectance of approximately 93.7% and an infrared emissivity of approximately 0.919 (figure 12(e)). In the same year, Zhu *et al* proposed a polyoxymethylene (POM) nanofiber radiative cooling textile [156]. As shown in figure 12(f), unlike the broadband emission characteristics of traditional radiative cooling textiles in the MIR band, this textile exhibits high emissivity in the ATSW and high transmission outside the window. Therefore, it can achieve efficient human body radiative cooling both outdoors (in sunny and cloudy weather) and indoors, providing a solution to the incompatibility issue between outdoor and indoor human body cooling design. In 2024, a multilayer structured radiative cooling silk (MST) based on electrospinning technology was developed, as illustrated in figure 12(g) [157]. The radiative cooling fabric achieved a solar reflectance of 0.965 and an infrared emissivity of 0.971, and it also exhibited excellent wearability and biosafety. Also in 2024, to address the urban heat island effect, Wu *et al* developed a spectrally selective hierarchical fabric (SSHF) [106] with dominant emissivity in the ATSW, minimizing the net thermal gain from the environment. Owing to the strong Mie scattering from its nano-micron hybrid fiber structure, the SSHF exhibits a high solar spectral reflectance of 0.97. When vertically positioned in a simulated outdoor urban setting during the day, the SSHF was 2.3 °C cooler than solar-reflective broadband emitters and demonstrated exceptional abrasion resistance.

**4.1.3. PV cooling.** Solar energy is widely regarded as a clean and abundant source of power, playing a crucial role in addressing the increasingly severe energy crisis [164]. The

Shockley–Queisser model [161] serves as a critical tool for evaluating the thermodynamic limits of solar cell performance. Within this model, under the radiative recombination limit and assuming efficient collection of all generated carriers without any reflection losses, the product of the open-circuit voltage  $V_{OC}$  of a single p–n junction solar cell and the charge  $q$ —a key parameter determining the optimal efficiency—is less than the bandgap energy  $E_g$ , as described by the following equation [163]:

$$qV_{OC} = E_g \left( 1 - \frac{T_{cell}}{T_{sun}} \right) - kT_{cell} \\ \times \left[ \ln \left( \frac{\Omega_{emit}}{\Omega_{sun}} \right) + \ln \left( \frac{4n^2}{I} \right) - \ln(QE) \right]. \quad (65)$$

The first term on the right represents the conversion of the energy of photons with  $E_g = h\nu$  (where  $\nu$  is frequency) to electrostatic energy and includes fundamental thermodynamic losses based on Carnot's theorem, where  $T_{cell}$  is the solar-cell temperature and  $T_{sun}$  is the temperature of the Sun. This reduces  $V_{OC}$  by 5% compared with  $E_g$  at room temperature.

The term within the square brackets incorporates three entropy-related factors, which contribute to the linear degradation of solar cell performance with increasing temperature. The first component reflects the entropy increase due to photon absorption and re-radiation via spontaneous emission in a semiconductor; whereas an incoming photon from the direct solar spectrum is incident within a narrow solid angle of  $\Omega_{sun} = 2.16 \times 10^{-5}$  rad, the outgoing photons emitted through spontaneous emission are distributed over a broader solid angle of  $\Omega_{emit} = 2\pi$  rad. Furthermore, the Shockley–Queisser limit represents the thermodynamic theoretical limit that a single pn-junction cell can achieve without considering the last two terms, as illustrated in figure 13(a). This limit does not exceed 33% at room temperature and deteriorates with increasing temperature.

However, for decades, the efficiency of solar cells has remained below the thermodynamic limit, with most manufactured cells maintaining an efficiency range of 10%–18% [163]. This discrepancy is primarily explained by the last two terms of equation (65). The term  $\ln \left( \frac{4n^2}{I} \right)$ , where  $\ln \left( \frac{4n^2}{I} \right)$  represents the refractive index and  $I$  the light concentration factor, describes the effect of incomplete light trapping within the solar cell, which is particularly relevant for light with energy just above the bandgap energy  $E_g$  and poorly absorbed. In a planar cell without light trapping,  $E_g$  is equivalent to 1, and this term reflects a loss in open-circuit voltage  $V_{OC}$  of approximately 100 mV. Conventional solar cells also feature a surface texture that results in multiple internal reflections of light within the semiconductor slab, enhancing the light intensity by a factor of  $I$  relative to a planar slab. For cells operating within the classical ray optical limit, the maximum achievable value of  $I$  is  $4n^2$ , causing this entropy term to vanish.

The last term within the square brackets elucidates another significant cause of efficiency loss: non-radiative exciton recombination. This recombination is predominantly caused by crystallographic defects, impurities, and other carrier traps

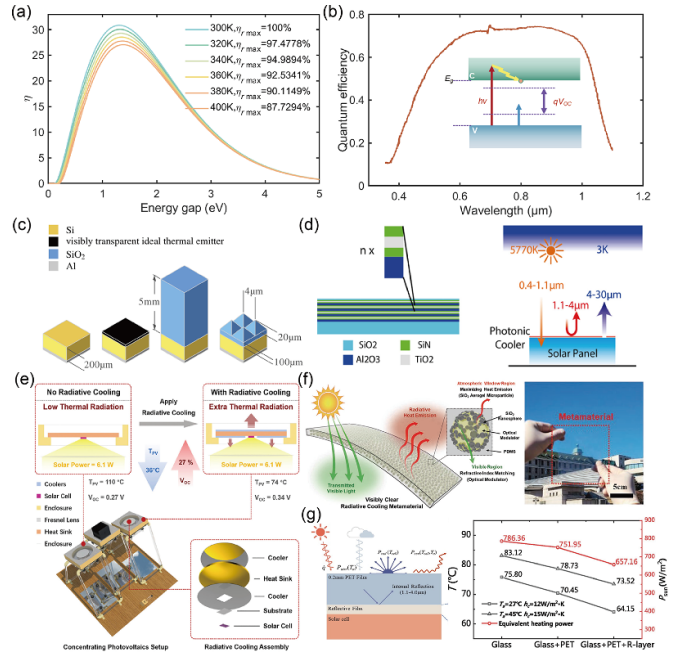


**Figure 13.** Temperature effects and radiative cooling structures for solar cells. (a) Limiting efficiency curves for a single band-gap (p–n junction) solar cell at various temperatures [161].  $\eta$  represents the absolute efficiency, while  $\eta_r$  denotes the relative efficiency. (b) Quantum efficiency of a silicon solar cell [162]. The inset depicts the energy diagram of a single-junction solar cell [163]. Light with energy  $h\nu$  (indicated by the red arrow) induces excitation from the valence band ( $V$ ) to the conduction band ( $C$ ) in the semiconductor. Following thermalization within the conduction band, an electron-hole pair is generated across the bandgap with energy  $E_g$ . Light with energy below the bandgap (represented by the blue arrow) remains unabsorbed. (c)  $\text{SiO}_2$  photonic crystal. Reprinted with permission from [25] © Optical Society of America. (d)  $\text{SiO}_2$ - $\text{SiN}$ - $\text{Al}_2\text{O}_3$ - $\text{TiO}_2$  multilayer film. Reprinted with permission from [26]. Copyright (2017) American Chemical Society. (e) Radiative cooling device for CPV. Reprinted from [27], Copyright (2020), with permission from Elsevier. (f)  $\text{SiO}_2$  aerogel microparticle@PDMS metamaterial. [28] John Wiley & Sons. © 2021 Wiley-VCH GmbH. (g) PET-metal composite film. Reprinted from [29], Copyright (2022), with permission from Elsevier.

within the bulk, at interfaces, and on the surface. The quantum efficiency for radiative recombination ( $QE$ ) is defined as  $QE = R_{rad}/(R_{rad} + R_{nrad})$ , where  $R_{rad}$  and  $R_{nrad}$  represent the radiative and non-radiative recombination rates, respectively. As illustrated in figure 13(b), the peak QE of silicon cells does not exceed 0.8 and declines rapidly with spectral blue-shift in the visible range [162], undoubtedly resulting in considerable energy loss.

Due to the limitations of battery efficiency, only a portion of solar energy is converted into electricity, with the remainder being dissipated as heat, leading to an increase in battery temperature [165]. In conjunction with our analysis of equation (65), it is evident that high temperatures induce a linear degradation in battery performance. Typically, for every 1 °C rise in temperature, the relative efficiency of solar cells decreases by 0.4%–0.5% [166]. Given that the global PV installed capacity exceeded 1.4TW in 2024, a 1 °C temperature rise results in an annual electricity loss

equivalent to the residential consumption of 6.4 million people in China. Consequently, employing daytime radiative cooling techniques to reduce solar cell temperatures by 1 °C–10 °C [15, 25, 27, 28, 167] presents a viable approach to enhancing battery efficiency and safeguarding the cells.

In 2014, Fan's team at Stanford University first proposed a strategy to enhance the infrared thermal emissivity of a battery by introducing periodic photonic structures on its surface, and theoretically validated the cooling effect that this strategy could bring about (figure 13(c)) [25]. In 2015, they designed and fabricated a visible-light-transparent  $\text{SiO}_2$  photonic crystal thermal radiation blackbody [15]. This structure maintained (and even slightly increased) the battery's absorption of solar energy while significantly enhancing its emissivity in the MIR range. Compared to bare silicon, it could achieve a temperature reduction of 13 °C for the covered silicon. In 2017, they further optimized the design by introducing a multilayer film photonic structure composed of  $\text{SiO}_2$ - $\text{SiN}$ - $\text{Al}_2\text{O}_3$ - $\text{TiO}_2$  on the battery's surface (figure 13(d)), achieving comprehensive spectral modification [26]. This photonic structure could achieve a broadband high emissivity in the MIR range for the battery while reflecting NIR solar radiation with a wavelength shorter than the battery's bandgap. Theoretical calculations predicted that this strategy could lower the temperature of commercial batteries by 5.7 °C. In 2020, Bermel *et al* designed a radiative cooling device for a concentrating PV (CPV) system (figure 13(e)) [27]. This device provided a large-area radiative cooling heat sink for GaSb solar cells, radiating to the sky without affecting the cell's reception of sunlight. Experimental results showed a temperature reduction of 5 °C–36 °C for the battery, corresponding to an 8%–27% relative increase in open-circuit voltage, and could extend the battery's lifetime by 4–15 times. In 2022, a fully transparent and flexible radiative cooling metamaterial by incorporating hexadecane-infused  $\text{SiO}_2$  aerogel particles into a PDMS film was developed (figure 13(f)) [28]. The resulting metamaterial exhibited over 91% high transmittance and greater than 98% high infrared emissivity. When integrated onto the surface of a solar cell, this material could lower the temperature of the cell by approximately 7.7 °C compared to a bare solar cell in outdoor tests. In the same year, Xia *et al* at Nanjing Tech University [29] proposed a PV cell composite structure incorporating a high-reflectivity layer composed of a polyethylene terephthalate (PET) film and metallic PDRC (figure 13(g)). Consequently, under direct outdoor sunlight, the operating temperature of the PV cell can be reduced by 11.65 °C.

Although photonic methods have demonstrated exceptional effectiveness in the radiative cooling of PV systems, it is crucial to acknowledge that the cost analysis of radiative cooling solar cells has scarcely been addressed, primarily due to the uneconomical nature of this approach. To illustrate, consider a typical 1 MW PV power plant equipped with 5000 m<sup>2</sup> of solar panels, which generates approximately 10<sup>6</sup> kWh of electricity annually. If the radiative cooling solution were to reduce the average temperature of the PV system by 10 °C, thereby enhancing its relative efficiency by 5% [166], an additional 50 000 kWh of electricity would be produced each year. Based on the typical electricity price in the United States of

0.1\$ kWh<sup>-1</sup> [168], this cooling strategy would yield an extra revenue of 1\$ (m<sup>2</sup> yr)<sup>-1</sup> for each unit area of the solar panel. However, given the typical lifespan of silicon cells, which is around 25 years [169], and the fact that the cost of photonic-based PV cooling solutions is often several times or even tens of times higher than 25\$ m<sup>-2</sup> due to material and processing limitations, the cost recovery of this approach presents a significant challenge. Until the cost issue of 25\$ m<sup>-2</sup> is effectively addressed, radiative cooling solar cells will remain in a state of negative returns, thereby limiting the large-scale application of radiative cooling solutions in PV systems due to the tradeoff between cost and performance in terms of economics. We firmly believe that once the cost issue is resolved, radiative cooling technology will witness a revolutionary breakthrough and advancement in the field of PV cooling.

**4.1.4. Other potential and extension applications.** At room temperature, a daytime sub-ambient radiative cooler can provide a net cooling power of approximately 100 W m<sup>-2</sup> [143]. This power output may not be sufficient for some large-scale, energy-intensive cooling scenarios; however, the generated cold is ingeniously harnessed for a range of potential and extended applications.

**4.1.4.1. Electricity generation.** Carefully designed selective thermal emitters [176] and selective solar absorbers [177] are each poised to maintain a temperature difference with the surrounding environment throughout the day. The combination of these two elements opens up more possibilities for the development of thermoelectric generators. In 2019, Fan *et al* at Stanford University integrated radiative coolers with thermoelectric generators, utilizing the cooler as the cold side and the ambient air as the hot side [170]. In this setup, thermoelectric devices can continuously generate electricity via the Seebeck effect (figure 14(a)). The output power measured under nighttime conditions exceeded 100 mW m<sup>-2</sup>, sufficient to power specific electronic devices such as light-emitting diodes (LEDs) and sensors. Owing to the inevitable absorption of sunlight, radiative cooling thermoelectric generation with ambient air as the hot side often underperforms during the day. In 2022, Chen's group circumvented this issue by directing sunlight onto a solar-selective absorber at the hot side of the thermoelectric generator using mirrors, with the radiative cooler serving as the cold side (figure 14(b)) [171]. This approach yielded a significantly higher output power of 489 mW m<sup>-2</sup> during the day. Following a similar rationale, in 2023, Li *et al* used a radiative cooler as the cold side and fixed the hot side to a copper plate exposed to direct sunlight (figure 14(c)), achieving an impressive power output of 3 W m<sup>-2</sup>, capable of charging small electronic devices such as calculators [172].

**4.1.4.2. Water harvesting, desalination and ice storage.** Conventional freshwater harvesting methods necessitate additional energy sources, such as electricity and fossil fuels, leading to significant energy consumption [173, 178, 179]. Radiative cooling has emerged as a viable strategy for water

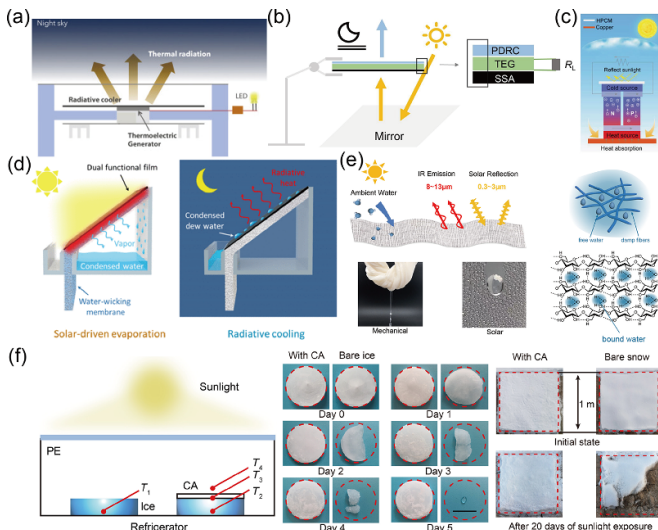


**Figure 14.** Radiative cooling devices hold immense potential with a range of extended applications. (a) Thermoelectric power generation utilizing nighttime radiative cooling. Reprinted from [170], Copyright (2019), with permission from Elsevier. (b) All-weather thermoelectric power generation with radiative temperature control, enhanced by the use of mirrors. Reprinted from [171], Copyright (2022), with permission from Elsevier. (c) All-weather thermoelectric power generation featuring copper plates as solar-selective absorbers for radiative temperature control. [172] John Wiley & Sons. © 2023 Wiley-VCH GmbH. (d) Sustained freshwater collection via the integration of interfacial solar desalination and dew condensation harvesting. Reprinted with permission from [173]. Copyright (2020) American Chemical Society. (e) Cellulose-derived fabrics designed for water harvesting purposes. Reprinted with permission from [174]. Copyright (2022) American Chemical Society. (f) Ice storage enabled by radiative cooling. From [175]. Reprinted with permission from AAAS.

collection and addressing water scarcity issues. For centuries, humans have harnessed radiative condensation to gather dew [180]. Initially, reported radiative dew condensers were only operational at night, relying on their ability to radiate MIR thermal energy to the clear night sky [181–183]. Conventional solar interfacial evaporators for freshwater collection are sunlight-dependent and are not effective for seawater desalination during the night. Recent studies have demonstrated that the combination of solar-driven interfacial desalination with dew generation enables all-weather water collection [173, 179, 184, 185]. In 2020, Xu *et al* at Stanford University developed a thin-film-based bifunctional system that integrates interfacial solar-thermal desalination with dew collection, capable of generating freshwater during the day (figure 14(d)) [173]. This thin-film system exhibits a solar absorption rate of approximately 95% and an emissivity of around 0.9 in the 8–13 micron wavelength range. This configuration can produce freshwater at a rate of  $1.13 \text{ l} (\text{m}^2 \text{ h})^{-1}$  with a water collection efficiency of 71.1%. During the day, it can desalinate seawater under one sun illumination, and at night, it collects dew at a rate of  $0.1 \text{ l} (\text{m}^2 \text{ d})^{-1}$ . In 2022, Chen's group designed an all-weather freshwater collection device that utilizes a solar selective absorber (SSA) in conjunction with sky radiative

cooling [179]. The fabricated SSA boasts a high solar absorption rate of 0.92 and a MIR thermal emissivity of 0.11, which, by minimizing thermal radiation losses, offers superior diurnal thermal conversion performance. Additionally, it incorporates a hollow structure to reduce conductive heat losses, achieving a high solar evaporation rate ( $1.23 \text{ kg m}^{-2} \text{ h}^{-1}$ ). Moreover, a plasma-treated transparent radiative cooling polymer with enhanced solar transmittance (0.92) and MIR thermal emissivity (0.91) is employed for freshwater collection. A theoretical freshwater collection rate of  $0.044 \text{ kg m}^{-2} \text{ h}^{-1}$  was achieved during the night. Outdoor results indicate an all-day water collection amount of  $0.87 \text{ kg m}^{-2}$ . This strategy of all-day water collection through the coupling of SSA and transparent radiative cooling shows potential for applications in seawater desalination and freshwater collection in tropical desert regions. In the same year, a cellulose-based hierarchical structured radiative cooling fabric was reported for efficient water collection (figure 14(e)) [174]. The abundant hydroxyl groups on the cellulose chains can strongly adsorb water through hydrogen bonding. Notably, this fabric can be curled or folded, and the adsorbed water can be extracted through mechanical compression or heating.

As the ambient temperature decreases further, the surface temperature of the cooler will fall below the freezing point of water. Dew on the surface will then transform into ice, and the existing ice is safeguarded to prevent melting under solar radiation. This concept can be regarded as an extension of water harvesting and has been successfully demonstrated in experiments (figure 14(f)) [175].

#### 4.2. Active dynamic thermal management

A single spectral design cannot fully meet the customized thermal management needs of people in different environments and climatic conditions. For example, while daytime radiative cooling devices can provide significant cooling effects and energy savings in hot summer conditions, they may lead to environmental overcooling at night or during cold winter periods, potentially increasing the energy consumption of additional heating systems or reducing human thermal comfort [186, 187].

Active dynamic radiative thermal management devices can activate their radiative cooling function in high-temperature environments and close their thermal radiation channels in low-temperature environments, achieving radiative insulation or solar heating. This provides a feasible solution for radiative thermal management that adapts to environmental changes. Therefore, they have been widely studied in the past five years. However, achieving dynamic radiative thermal management devices still faces challenges such as energy consumption, spectral modulation efficiency, and process complexity. Researchers have proposed various strategies to address these issues and specific application scenarios.

##### 4.2.1. Janus structure with asymmetric spectral design.

The asymmetric spectral structure is primarily achieved through the design of completely opposite spectral control

on the front and back sides of the device (i.e. the front side for the spectral control needed for radiative cooling, and the back side for the spectral control required for radiative insulation/heating), thereby forming a unique Janus (two-faced) structure. By simply flipping the device, the outward spectral characteristics of the thermal management object can be rapidly altered to switch between cooling and insulation/heating modes. Although the Janus structure inherently represents a static spectral control strategy, its simplicity in implementation, ease of fabrication, and the higher degree of freedom in material selection for static spectral properties have led to extensive research in recent years.

In 2017, Cui's group at Stanford University designed an indoor DM thermal management textile, as shown in figure 15(a) [188]. The core structure of this textile consists of a bilayer asymmetric thermal radiator composed of carbon (C) and copper (Cu), embedded within an infrared-transparent nanoPE film. In the radiative cooling mode, the high-emissivity C layer faces the environment. Due to the reduced thickness of the nanoPE between the human skin and the thermal radiator at this time, body heat can be efficiently transferred to the thermal radiator via thermal conduction. When the textile is flipped to operate in the insulation mode, the side with lower emissivity faces outward to minimize heat loss. This structural design can expand the human thermal comfort zone by 6.5 °C. In 2019, a multifunctional Janus film with a sandwich structure by sequentially depositing ultra-long MnO<sub>2</sub> nanowires and Cu nanowires onto a cellulose fiber@layered double hydroxide (LDH) substrate membrane via vacuum filtration (figure 15(b)) was developed [189]. The resultant Janus film exhibits asymmetric infrared radiative emissivity, which is utilized for on-demand PTM: the low emissivity layer (Cu NWs layer) faces outward to impede body heat radiation, while the high emissivity layer (cellulose@LDH layer) is turned outward to enhance body heat radiation. Additionally, the film boasts excellent breathability, flexibility, interfacial compatibility, and wear-resistant antibacterial activity.

For DM radiative thermal management in outdoor environments, in 2021, Li's group reported a multilayered passive nanostructured Janus textile, as shown in figure 15(c) [190]. In the heating mode, the textile utilizes a copper/zinc nanoparticles (Cu/ZnNPs) coating to suppress the MIR emissivity (~0.16) while leveraging localized surface plasmon resonance (LSPR) to absorb solar radiation (>0.8). On the cooling side, the textile achieves a MIR emissivity of ~0.87 and a solar reflectance of ~0.91, utilizing a porous structure of PTFE and polymethyl methacrylate (PMMA). Compared to traditional textiles, this Janus textile can increase or decrease the temperature of a simulated skin by 8.1 6 °C<sup>-1</sup> under sunlight exposure, while also allowing for continuous power generation using a thermoelectric module. In 2022, Xu's group fabricated a Janus film (figure 15(d)) [191], which integrated opposite functions of cooling and heating by embedding SiO<sub>2</sub> and CNTs within PDMS, respectively. This method exhibits minimal modulation in the infrared spectrum, with the heating mode relying on sunlight, while the cooling function is

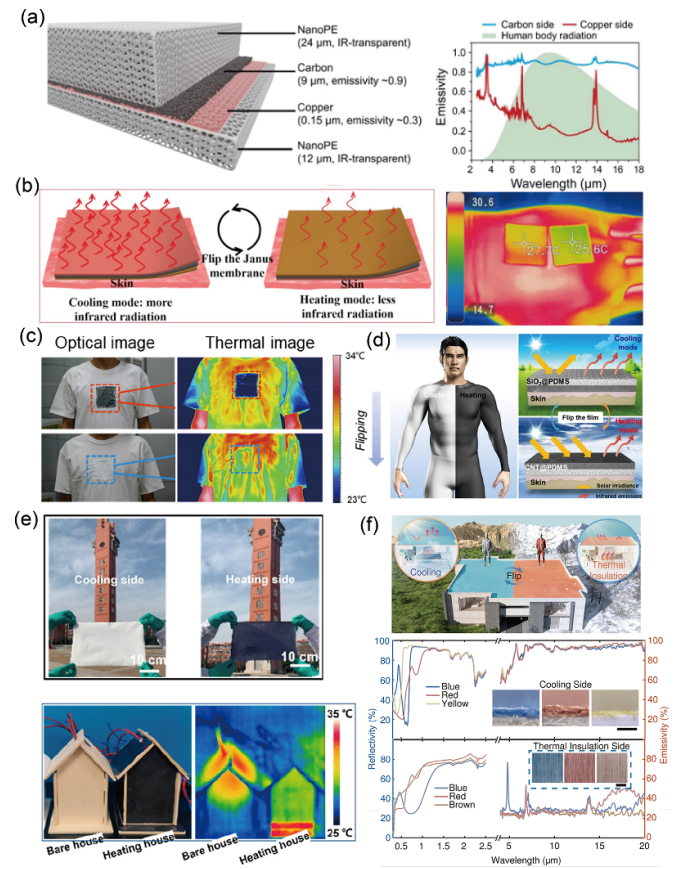


**Figure 15.** Janus materials. (a) Schematic illustration and spectral graph of the copper/carbon-nanoPE bimodal fabric. From [188]. Reprinted with permission from AAAS. (b) Schematic illustration and infrared photograph of the MnO<sub>2</sub>NWs/CuNWS-LDH Janus film. Reprinted from [189], Copyright (2019), with permission from Elsevier. (c) Photograph and infrared photograph of the nanostructured Janus textile. Reprinted with permission from [190]. Copyright (2021) American Chemical Society. (d) Schematic illustration of the SiO<sub>2</sub>/CNT-PDMS Janus film. Reprinted with permission from [191]. Copyright (2022) American Chemical Society. (e) Photograph and infrared photograph of the PVDF/MXene Janus film. Reprinted with permission from [192]. Copyright (2023) American Chemical Society. (f) Schematic illustration and spectral graph of the dual mode Janus fabrics. Reproduced from [104]. CC BY 4.0.

maintained throughout the night. In 2023, a PVDF/MXene Janus film by decorating MXene on porous PVDF with a rich coral-like hierarchical structure was reported [192]. This Janus film can easily switch between cooling and heating modes by flipping (figure 15(e)), achieving a diurnal temperature drop of 9.8 °C in cooling mode and a temperature rise of 8.1 °C in heating mode. Similar film materials include AgNW/rGO/PVDF and PPy/NaH<sub>2</sub>PO<sub>4</sub>@PMMA Janus films. In 2024, Pian *et al* reported a DM radiative thermal management fabric based on fiber and weaving structures [104]. Functionally, the cooling side of the fabric consists of a PTFE porous film overlaying a PLA fiber weave doped with TiO<sub>2</sub> nanoparticles, achieving a solar reflectance of 92% and an infrared emissivity of 94%. Conversely, the insulating side

is made of a metal wire weave coated with PE, exhibiting an infrared emissivity below 30%. Macroscopically, the DM fabric features a three-dimensional, multi-layered weaving structure that spatially stratifies to accommodate various structural scales, ingeniously integrating nanostructures, fiber structures, and the spatial configuration of the fabric. Thanks to its multilayer design, both the cooling and insulating sides can be simultaneously colored and are easily compatible with scalable manufacturing processes. This fabric demonstrates remarkable thermal management performance and energy-saving effects under diverse climatic conditions (figure 15(f)).

In addition to their use in human thermal management fabrics, Janus materials also show promise for applications in settings such as buildings and windows. In 2022, Han's group proposed a DM asymmetric photonic mirror (APM) composed of silicon-based diffraction gratings, which demonstrated an average infrared asymmetry of 20% between outgoing and incoming radiation [119]. Under overcast skies, the APM in cooling mode achieved an 8 °C temperature drop, while the APM in heating mode resulted in a 5.7 °C temperature increase. It is important to note that the photothermal materials commonly used are often dark in color, which restricts the further large-scale application of Janus materials in scenarios with high daylighting needs.

Due to the ability to adapt to various environments, Janus materials possess strong thermal management capabilities. However, all reported Janus materials to date are static and require manual flipping for mode switching. By incorporating appropriate simple mechanical structure designs, Janus materials can also achieve continuous or quasi-continuous active mechanical regulation. In 2020, a thermal management device based on polyimide (PI) film was proposed, which features side-by-side solar heating and radiative cooling components [193]. To enable continuous regulation of the thermal management power, the device utilizes a pair of electro controllable rotary actuators to adjust the area of the heating and cooling sections exposed to the sky. Inspired by the structure of blinds, in 2022, a multi-mode switchable thermal management system was developed, integrating radiative cooling and heating sections on the rotatable blades of blinds, achieving multi-mode switching between radiative cooling, solar heating, and natural lighting [194]. Long's team proposed a programmable interwoven radiative thermal management surface that can dynamically switch the overlapping sequence of cooling and insulation modes to regulate the functions of radiative cooling and solar heating [195].

#### 4.2.2. Mechanical stretchable optical structure.

Mechanically stretchable optical structures are typically fabricated on elastic substrates such as PDMS. By stretching (or compressing) the elastic substrate, the geometric parameters of the internal optical response structures, such as period, volume, and duty cycle, are altered, thereby modulating the overall optical response characteristics of the device. Since stretching is a continuous process, this strategy can generally

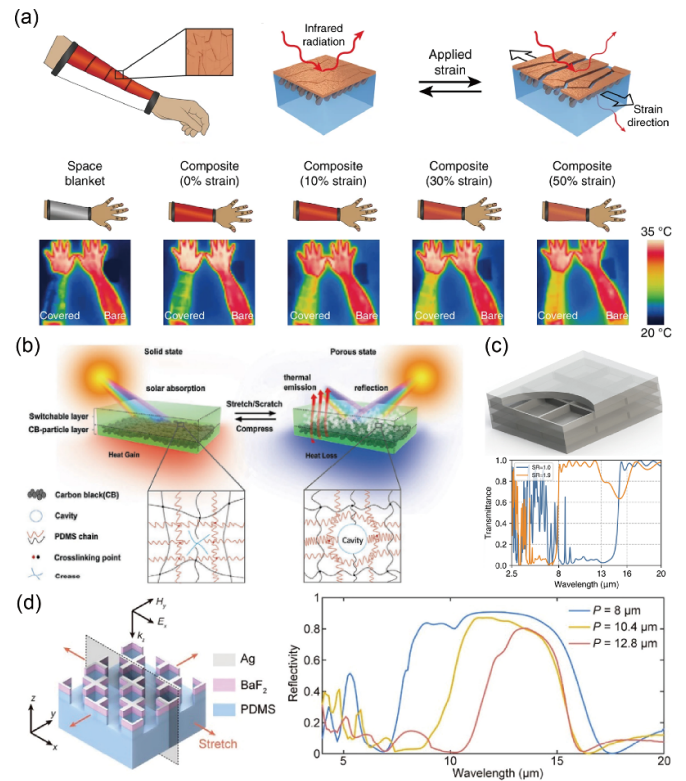


**Figure 16.** Dynamic radiative thermal management devices based on mechanically stretched optical structures. (a) Squid skin biomimetic composite material. Reproduced from [196]. CC BY 4.0. (b) Mechanically responsive silicone cooling/heating coating. Reproduced from [197]. CC BY 4.0. (c) Stretchable selective optical filter based on a multilayer film structure. Reprinted with permission from [198]. © Optical Society of America. (d) Stretchable metal–dielectric–metal metasurface emitter (SME). Reprinted with permission from [12]. © Optica Publishing Group.

achieve continuous and uniform modulation of the spectral properties on the device surface, offering unique advantages in dynamic radiative thermal management.

In 2019, Gorodetsky's team at University of California drew inspiration from the dynamic color-changing ability of squid skin and developed a composite material with tunable radiative properties [196]. As shown in figure 16(a), the composite consists of two layers: a bottom stretchable infrared-transparent polymer substrate and a top layer of infrared-reflective metal structures. Without mechanical actuation, the composite reflects nearly all incident infrared radiation. Under mechanical actuation, the gaps between the metals increase, exposing the bottom polymer substrate and leading to the transmission of thermal radiation. The material has a transmittance switch ratio of approximately 25, and with an estimated mechanical energy input of  $\sim 3 \text{ W m}^{-2}$ , it can modulate the heat flux by about  $36 \text{ W m}^{-2}$ . In 2020, Cui *et al* developed a mechanoresponsive silicone cooling/heating coating [197]. As shown in figure 16(b), this material achieves spectral regulation of solar radiation wavelengths by controlling the opening and closing of internal pores. In the compressed state, the

internal pores close, reducing reflectance and allowing for the absorption of 95% of solar radiation. In the stretched state (achieved through stretching, scratching, etc.), the internal pores open, reflecting 93% of solar radiation. Also in 2020, Ma *et al* developed a stretchable multilayer film structure selective filter using highly elastic and stretchable material, ethylene-propylene-diene monomer (EPDM), and air as high and low refractive index layer materials, respectively, which is suitable for tunable radiative cooling (figure 16(c)). Based on the principle of thin-film interference, the stretching operation alters the film thickness, thus modulating the emissivity of the radiative cooling system within the atmospheric window. As the stretch ratio increases from 1 to 1.9, the filter achieves continuous transmittance modulation from 0.05 to 0.95 in the atmospheric window. With the cooling mode turned off, the temperature decrease is only 1 °C; however, with the cooling mode activated, the average temperature decrease reaches 7.7 °C, demonstrating exceptional dynamic response characteristics. In 2024, Ma *et al* introduced a stretchable metal–dielectric–metal metasurface emitter (SME) for dynamic radiation management (figure 16(d)) [12]. In its initial state, the metasurface leverages resonance effects to reduce its emissivity within the ATSW band, thereby achieving insulation. During biaxial stretching, the periodicity of the metasurface is adjusted, causing a shift in the resonance wavelength and enhancing its thermal emission capability. Concurrently, the stretching process leads to a reduction in the substrate thickness and an increase in the spacing between meta-atoms, thereby decreasing the solar absorption of the SME. Throughout the stretch ratio ranging from 1 to 1.6, the SME achieved continuous emissivity modulation from 0.14 to 0.75 in the ATSW band. Under natural convection conditions at 25 °C during daytime, the device is projected to provide a temperature control range of approximately 15.0 °C, demonstrating exceptional capabilities for wide-range continuous regulation.

**4.2.3. Moisture transfer technique.** By reversibly wetting porous polymers, the adjustment of light scattering characteristics can be readily achieved for dynamic switching [199, 201]. Due to the potential for multiple scattering processes at the interface between the pores and the polymer framework, the scattering efficiency can be altered by infusing liquid into the pores. In 2019, Mandal *et al* discovered that porous white PVDF-HFP films, when wetted with isopropanol, transition from opaque to transparent in the solar spectrum, with a decrease in light scattering and an increase in solar transmittance [199]. Additionally, porous PE films reversibly convert from infrared-transparent to opaque upon immersion in alcohol (figure 17(a)). The optical conversion mechanism primarily relies on the inherent non-absorbing nature of the polymer and the difference in refractive index. Wetting porous polymers with a liquid having a matching refractive index can transition the polymer from scattering to transparency. This functionality can be applied to seasonal or diurnal temperature regulation and energy-efficient architectural design.

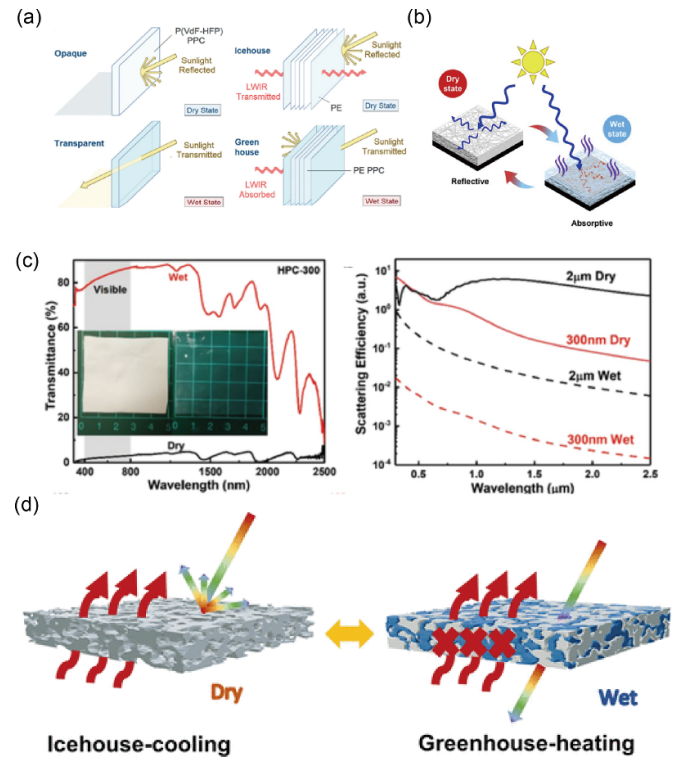


**Figure 17.** PDRC materials based on moisture transfer technique. (a) Schematic illustration of a PVDF-HFP film. Reprinted from [199], Copyright (2019), with permission from Elsevier. (b) Schematic illustration of Janus cellulose. Reproduced from [200]. CC BY 4.0. (c) Photograph, transmission spectrum, and scattering efficiency of the hierarchical porous PVDF coating. [201] John Wiley & Sons. © 2022 Wiley-VCH GmbH. (d) Schematic illustration of a structured polyethylene film. Reprinted with permission from [13]. Copyright (2024) American Chemical Society.

In 2022, Jonsson's team reported on a Janus cellulose structure composed of a porous cellulose layer and an underlying layer of cellulose doped with carbon nanotubes (figure 17(b)) [200]. In its dry state, the material is reflective, exhibiting high reflectivity and low absorbance; upon wetting, the reflectivity decreases significantly ( $\Delta R \approx -0.5$ ), and the optical transparency of the top layer increases, allowing the bottom layer to absorb four times more sunlight than in the dry state and convert it into heat (approximately 60%). This, in turn, initiates an adaptive process that drives water evaporation and dries the structure, causing it to reflect once more. Also in 2022, Li's group reported the first instance of a graded porous PVDF single-layer coating prepared using a simple one-step method (figure 17(c)). This coating exhibits rapid switching between high solar reflectance (approximately 96.6%) and high solar transmittance (approximately 86.6%) [201]. In its dry state, the coating's high solar reflectance and infrared (IR) emissivity (greater than 96% in the range of 8–13 μm) enable passive radiative cooling, maintaining near or below ambient temperatures throughout the day under harsh weather conditions typical of tropical climates. When the coating is wet, its

broadband transparency (0.3–2.5  $\mu\text{m}$ ) significantly increases, allowing for solar heating and enabling a switchable thermal regulation. In 2024, Chen *et al* designed a novel structured PE film, which possesses switchable cooling and heating modes obtained through moisture transfer technology (figure 17(d)) [13]. The 100  $\mu\text{m}$  PE film demonstrates exceptional thermal modulation performance with values ranging from 0.92 (dry state) to 0.32 (wet state) and from 0.86 (dry state) to 0.05 (wet state), respectively. This achievement enables effective thermal regulation during both day and night.

**4.2.4. Electrochromic materials.** Under electrical or electrochemical stimulation, electrochromic materials exhibit reversible optical property changes in the visible and infrared ranges, such as alterations in transmittance and reflectivity [205]. Recently, electrochromic technology has been employed in the fabrication of dynamic, switchable smart windows, enabling reversible switching of optical or infrared signals and thus enhancing the energy efficiency of buildings. These smart windows exhibit exceptional modulation efficiency, capable of rapidly transitioning from a bleached state to a colored state and uniformly coloring the entire window surface within seconds [14, 202–204, 206–208].

In 2021, Hsu's group proposed an electrochromic device composed of a single-layer graphene, gold (Au), and a PE film, as depicted in figure 18(a) [202]. This electrochromic device boasts ultra-broadband (0.2–20  $\mu\text{m}$ ) high transparency and low sheet resistance, which can be electrodeposited on a transparent conductive electrode using a three-electrode cyclic voltammetry. The device can switch from a cooling mode (high emissivity) to a heating mode (low emissivity), while also controlling the absorption of solar radiation. In 2023, they further developed a water-based flexible electrochromic design (figure 18(b)) for building radiative thermal management based on graphene's ultra-broadband transparent conductive electrodes and reversible copper electrodeposition [203]. By switching the voltage, the thermal radiation emissivity of the device can be tuned from 0.07 to 0.92. In the same year, Yu *et al* integrated plasmonic gold nanorods with electrochromic W<sub>18</sub>O<sub>49</sub> nanowires based on a co-assembly strategy to create an electrochromic and thermochromic smart window for solar regulation, as illustrated in figure 18(c) [204]. When a 1.5 V negative voltage is applied, the window transitions to a colored state, effectively blocking over 90% of near-infrared solar radiation, thereby reducing indoor temperatures by about 5 °C under sunlight. This strategy was also applied to the design of traditional thermochromic windows by the team, which successfully broadened the temperature response range of thermochromic smart windows through the co-assembly of heat-sensitive W-doped VO<sub>2</sub> (W-VO<sub>2</sub>) nanowires with varying amounts of tungsten.

#### 4.3. Thermal control material with environmental adaptability

Active dynamic switchable cooling systems offer a convenient means to meet evolving cooling and heating demands, thereby providing thermal comfort to humans. However,

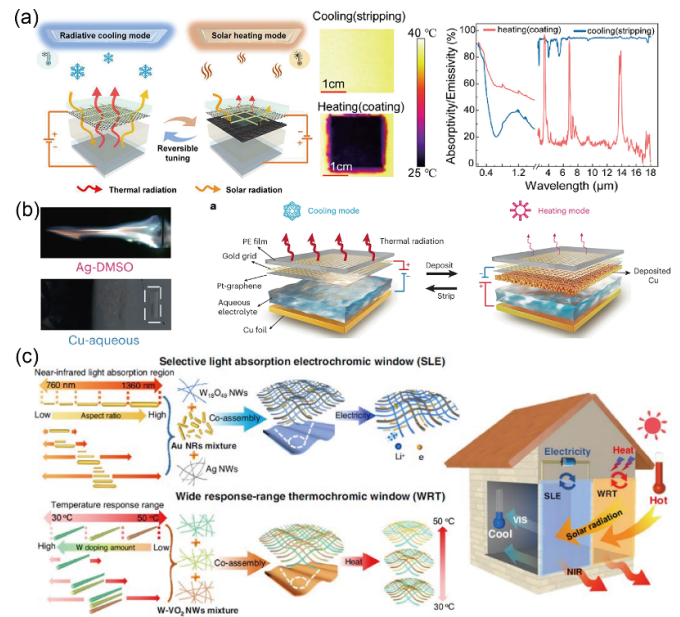


**Figure 18.** Dynamic radiative thermal management devices based on electrochromic materials. (a) Electrochromic materials based on ultra-wideband transparent conductive electrode (UWB-TCE). Reprinted with permission from [202]. Copyright (2021) American Chemical Society. (b) Copper-based water-soluble flexible electrochromic device. Reproduced from [203], with permission from Springer Nature. (c) Nanowire-based electrochromic/thermochromic smart windows for dynamic regulation of solar radiation. Reproduced from [204]. CC BY 4.0.

these mechanical, electrical, or chemical stimuli may also lead to excessive energy consumption. Consequently, passive dynamic switchable systems have been developed that can respond to changes in ambient temperature or humidity without the need for electrical input.

**4.3.1. Thermo-hygroscopic response-induced mechanical deformation.** Given the practical application, the spectral performance of dynamic radiative thermal management devices often varies with environmental conditions, such as temperature and humidity (including local humidity changes due to human sweat). A viable strategy is to utilize the temperature and humidity responsiveness differences between different materials to form a heterojunction. By the environmental changes causing the structure to undergo reversible mechanical deformation, the device's macroscopic optical structure can adaptively modulate in response to environmental parameters.

In 2019, Wang's team at the University of Maryland reported a textile capable of self-adaptively controlling spectral response in the MIR band, as illustrated in figure 19(a) [30]. This performance is achieved by using a dual-crystal fiber composed of hydrophobic triacetate and hydrophilic cellulose, with a coating of few-walled carbon nanotubes on the surface. This infrared-adaptive textile can directly respond to changes in the temperature and relative humidity of human skin. When the human body sweats due to a hot environment, the change in local humidity leads to yarn shrinkage (due to the difference

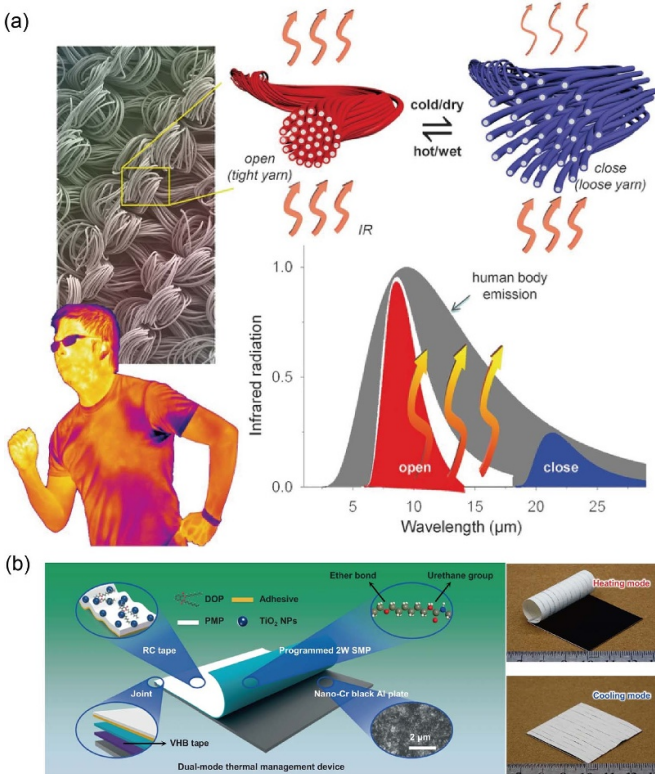


**Figure 19.** Dynamic radiative thermal management devices based on mechanical deformation in response to temperature/humidity. (a) MIR adaptive dynamic radiation control textile. From [30]. Reprinted with permission from AAAS. (b) Temperature-adaptive dynamic radiative thermal management device driven by a temperature-sensitive actuating layer. Reproduced from [31]. CC BY 4.0.

in the coefficient of thermal expansion between triacetate and cellulose), resulting in a blue shift in the electromagnetic coupling wavelength band that overlaps with human body radiation, thereby enhancing human body radiative cooling. In 2022, a zero-energy temperature-adaptive dynamic radiative thermal management device was reported [31]. As shown in figure 19(b), this device can automatically switch between operating modes based on ambient temperature. The device consists of three functional layers: a radiative cooling layer, a temperature-sensitive actuation layer, and a solar heating layer. By controlling the opening and closing of the radiative cooling layer through the temperature-sensitive actuation layer, the device can adaptively switch between cooling and heating/insulation modes. In the heating mode, the radiative cooling layer automatically rolls up to one side, allowing the solar heating layer to absorb solar radiation and suppress the structural heat radiation loss. When cooling is required, the radiative cooling layer can fully cover the solar heating layer to minimize solar absorption and promote its own heat radiation. The device can achieve an average heating power of approximately  $859.8 \text{ W m}^{-2}$  (approximately 91% of the solar thermal conversion efficiency) under cold conditions and an average cooling power of approximately  $126.0 \text{ W m}^{-2}$  under hot conditions.

**4.3.2. Radiation cooling devices with thermochromic materials.** Thermochromic materials are capable of controlling their intrinsic optical properties based on their critical temperature for phase transition, offering a zero-energy solution for dynamic radiative thermal management devices. Dynamic radiative thermal management devices based on thermochromic materials, due to their passive nature and temperature adaptability, hold great potential for practical applications. Among these, vanadium dioxide ( $\text{VO}_2$ ) is particularly noteworthy for its ability to transition from an insulator to a metal. Its unique  $68^\circ\text{C}$  phase transition temperature has made it a promising material for dynamic thermal regulation, attracting widespread attention [209].

In 2018, Fan's team at Stanford University designed a three-layer structure consisting of vanadium oxide ( $\text{VO}_2$ ), magnesium fluoride ( $\text{MgF}_2$ ), and tungsten (W) (figure 20(a)) [35]. This structure exhibits high absorption/high emission characteristics through the Fabry–Perot (F–P) resonance effect in the metallic state above the  $\text{VO}_2$  phase transition temperature. Conversely, at temperatures below the phase transition, the structure exhibits low absorption in the MIR wavelengths. By incorporating an 11-layer bandpass filter, a selective emission spectrum in the  $8\text{--}13 \mu\text{m}$  range is achieved. This design addresses the inherent conflict between the requirement for absorption in the MIR band for phase change materials and their temperature response. Building upon a similar structure, in 2021, Long and Yang *et al* developed a thermochromic smart window that spontaneously switches its MIR emissivity in response to temperature changes, as depicted in figure 20(b) [36]. As shown, this smart window is capable of simultaneously regulating the spectral properties of solar radiation and MIR thermal radiation. During transitions between high and low temperatures, the smart window's solar transmittance can be modulated by 9.3%, and its MIR emissivity can be tuned by approximately 0.4%. Also in 2021, Wu *et al* developed an ultra-surface coating (TARC) with high-efficiency self-adaptive control of MIR emissivity based on W-doped  $\text{VO}_2$ , barium fluoride ( $\text{BaF}_2$ ), and silver, as depicted in figure 20(c) [37]. By controlling the doping concentration, the phase transition temperature of the structure was successfully adjusted to room temperature. The device exhibits a MIR emissivity of 0.20 at temperatures below  $15^\circ\text{C}$  and can increase to 0.90 when the temperature exceeds  $30^\circ\text{C}$ , demonstrating excellent infrared spectral control capabilities. In 2023, a spectral self-adaptive broadband absorber/emitter based on  $\text{VO}_2$  was reported [211]. The device exhibits broadband infrared emissivity modulation, with an emissivity of 0.21 at high temperatures (above  $58.4^\circ\text{C}$ ) and an emissivity of 0.75 at temperatures below  $49.2^\circ\text{C}$ . This device has the potential to be applied in integrated photothermal systems and nighttime radiative cooling energy harvesting systems.

In addition to  $\text{VO}_2$ , organic materials such as polyN-isopropylacrylamide (pNIPAm), hydroxypropyl methylcellulose (HPMC), and hydroxypropyl cellulose (HPC) also exhibit excellent thermochromic properties. Among these, pNIPAm hydrogels are widely utilized in the construction of passive dynamic radiative thermal management devices due to their

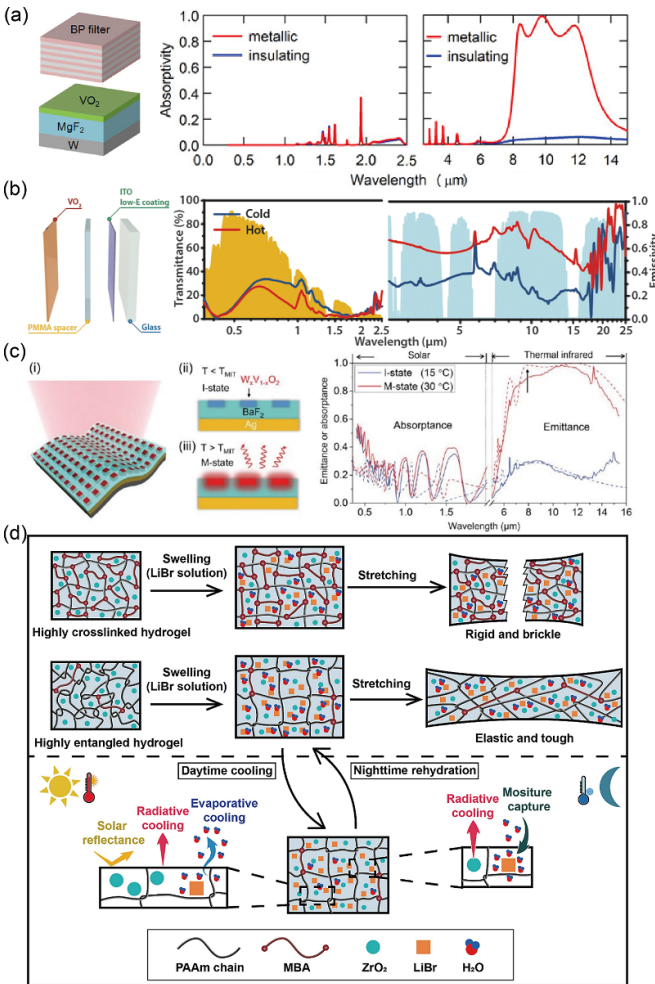


**Figure 20.** Thermochromic materials. (a) Selective emitter based on VO<sub>2</sub> and band-pass filter. Reprinted with permission from [35]. © Optical Society of America. (b) Thermochromic smart window based on VO<sub>2</sub>. From [36]. Reprinted with permission from AAAS. (c) Metasurface coating with adaptive emissivity control utilizing VO<sub>2</sub>. From [37]. Reprinted with permission from AAAS. (d) Schematic illustration of highly entangled hydrogel for sustainable daytime passive cooling enabled by daytime cooling process and nighttime rehydration. Reproduced from [210]. CC BY 4.0.

lower critical solution temperature (LCST) [32–34]. In 2023, Guan’s group discovered that traditional covalently cross-linked PNIPAm hydrogels hinder the phase transition of the hydrogel, potentially causing the smart window to contract and lose structural integrity after phase transition [212]. Building upon this observation, they developed a novel physically cross-linked hydrogel-derived smart window through *in situ* free radical polymerization of NIPAm monomers in a glycerol-water binary solvent system. The non-covalently crosslinked hydrogel exhibits excellent frost resistance, maintaining high transparency even when stored at  $-18^{\circ}\text{C}$ . In 2024, a highly cross-linked hydrogel with embedded particles and a hygroscopic agent was introduced [210], which synergistically harnesses daytime radiative, evaporative cooling, and hygroscopic effects for sustained passive cooling. As shown in figure 20(d), the hydrogel with dense entanglements exhibits elasticity and toughness post-swelling in LiBr solution, with

entanglement points from dense PAAm chains enhancing its mechanical robustness. Additionally, ZrO<sub>2</sub> particles endow the hydrogel with 0.9 solar reflectance and 0.88 MIR emissivity within the atmospheric window, while LiBr enables moisture capture for daytime evaporative cooling and overnight self-rehydration.

The characteristics, advantages, and limits of Dynamic thermal management materials are summarized in table 3.

## 5. Challenge and outlook

Despite the remarkable advancements achieved in fundamental physical mechanisms and innovative device design thus far, there remain several critical challenges that necessitate further resolution. These challenges encompass theoretical design, production, utilization, etc. If the research aims to address real-world applications, it is imperative to consider these aforementioned challenges from the very inception of the design phase. Drawing from future perspectives (figure 21), we will outline the potential for further enhancement of current research.

From the perspective of photonic design, advanced spectral manipulation plays a pivotal role in achieving high-performance radiative cooling. When discussing the impact of spectral band modulation on radiative cooling technology, we should not confine our focus to the traditional 8–13 μm atmospheric window. In fact, depending on varying climatic conditions and the operating temperature of the devices, we can consider utilizing other atmospheric windows to achieve varying radiative cooling effects [84]. Therefore, under specific environmental and operating temperature conditions, designing an ideal emission spectrum that covers the full band and all angles becomes a crucial strategy for enhancing the performance of radiative cooling devices [38]. Furthermore, to address complex working scenarios such as radiative cooling demands in urban environments, we can adopt designs that feature an asymmetric angular emission spectrum. This approach can effectively shield the radiative heat exchange from other high-temperature buildings, thereby improving cooling efficiency [98]. Moreover, although there are currently no practical applications of high-performance radiative cooling devices based on non-reciprocal radiative heat transfer, research in this field still holds great potential. In the study of photonic mechanisms, we should not overlook other interactions between light and matter beyond absorption and scattering. As shown in figure 11(b), using the fluorescence process to enhance the solar reflectance of buildings for radiative cooling not only opens up new research avenues but also has the potential to increase the yield of greenhouse products, demonstrating the vast potential of this technology in practical applications [139].

From the perspective of device design, the multifunctional properties of PDRC materials in practical applications are yet to be fully exploited. While the spectral characteristics of PDRC materials are considered, their thermal conductive properties are frequently underappreciated. The dielectric or organic materials commonly used in PDRC materials often

**Table 3.** Dynamic thermal management materials.

Materials/design	Description	Advantage	Limits
Janus structures	This structure features an asymmetric spectral design, enabling active regulation through flipping.	Rich combinations of feasible designs, economical and simple preparation process.	Fixed spectra on both sides, precluding continuous spectral regulation; automation of flipping process relies on additional mechanical structures.
Mechanical stretchable optical structure	Continuous deformation of the macrostructure results in a change in spectral response.	Absolute control of spectral response, continuously tunable with structural deformation.	Spectral response is limited by the material deformation, with high-frequency and extensive stretching reducing material lifespan.
Moisture transfer technique	By adjusting the internal liquid content, the spectral response of the material is altered.	Continuously tunable spectrum.	Requires external liquid supplementation, with a relatively slow response speed.
Electrochromic materials	Spectral response of the material is regulated by applying an external voltage.	Absolute continuous control of spectrum with rapid response.	High cost and complex preparation process.
Thermochromic materials	Utilizing the temperature sensitivity of phase-change materials or hydrogels, a passive response of spectral variation with temperature is achieved.	Features a temperature-adaptive passive response without the need for additional energy consumption.	High cost, limited temperature range for spectral change, and slow response speed.

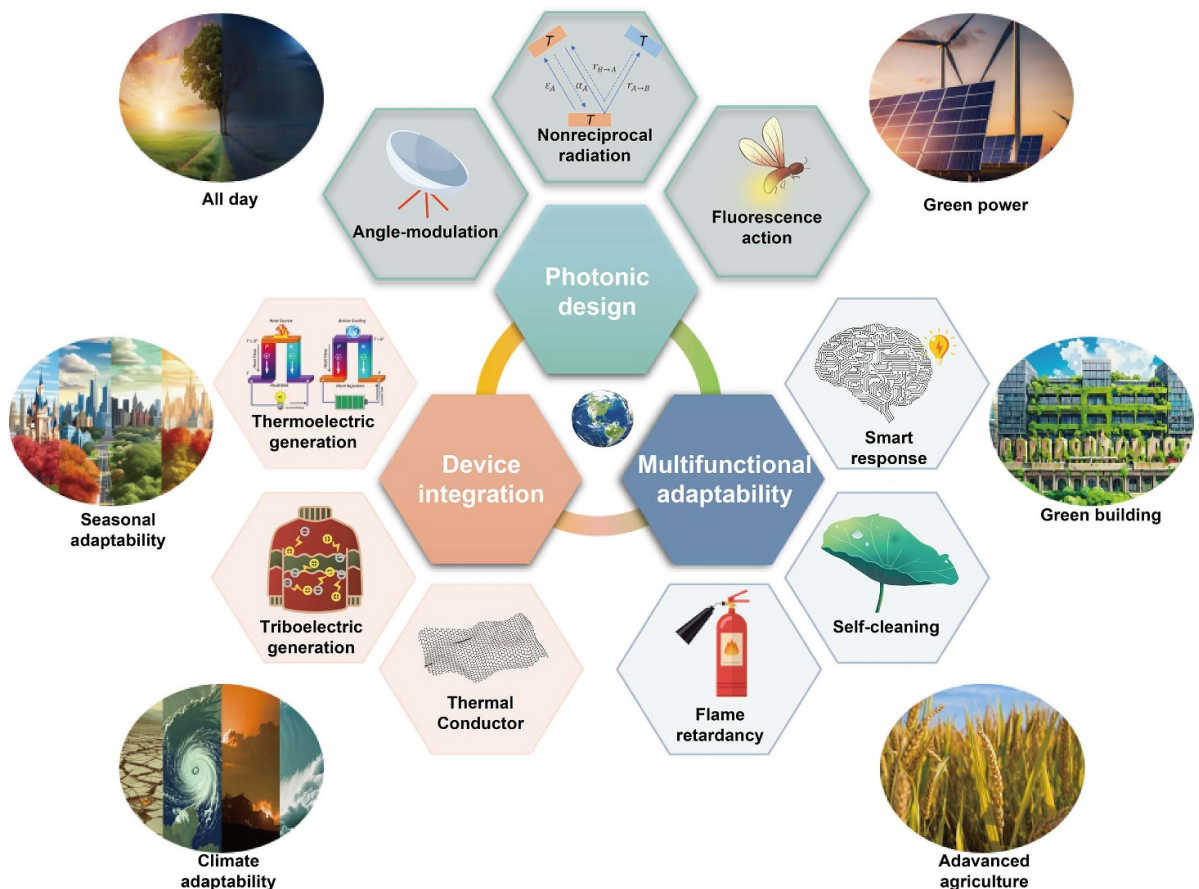
**Figure 21.** The outlook for future development and application of radiative cooling technology.

exhibit high thermal resistance, which can negatively affect the cooling efficiency of the material. Enhancing thermal conductivity represents a promising avenue for the development of novel PDRC materials. Additionally, PDRC materials offer a superior platform for integration with other functional devices, necessitating innovative mechanical structural designs. Research has already begun to integrate PDRC materials with mechanical structures for thermoelectric [170–172] and triboelectric [213] power generation. Exploring strategies to boost the performance and utility of these power generation systems is a fascinating research direction. We foresee the advent of advanced functional materials and designs that will substantially enhance the utility of radiative cooling materials across emerging fields.

For practical device applications, PDRC materials must exhibit durability, maintaining their intrinsic spectral properties despite external physical and chemical impacts such as scratching, dusts, contamination, oxidation, and UV aging. The mechanical properties of these materials should be considered from the outset of design, tailored to specific application environments, such as controlling particle doping within fabrics to enhance flexibility and wear comfort. Incorporating hydrophobic modifications into the material surface can endow PDRC devices with self-cleaning properties, thereby improving anti-soiling capabilities. The addition of fire-resistant materials like ceramic nanofibers, silica aerogels, and calcium carbonate can enhance the material's flame retardancy. Materials such as PTFE and barium sulfate can be used to enhance UV protection. Recycling is crucial, yet strategies for the disposal of radiative cooling materials are still under discussion, presenting a challenge to be addressed in material design and recycling processes. What's more, as indicated in sections 4.2 and 4.3, dynamic thermal management materials are attracting significant attention due to their tunable environmental adaptability. Take electrochromic thermal management materials for instance; their integration with PDRC and photothermal conversion features is particularly crucial for applications in building windows and automotive sunroofs. The flexible switching capability of these materials significantly enhances the adaptability of indoor spaces and vehicles to varying thermal conditions. Additionally, passive switchable materials, such as thermochromic materials represented by VO<sub>2</sub>, suggests vast potential for dynamic thermal management due to their self-adaptive properties. However, these materials are currently primarily in the laboratory research phase due to structural complexity, cost and technological constraints. In addition, the thermal regulation efficiency of most existing dynamic strategies is still very limited, and the control capabilities are limited to just single band between solar radiation and thermal radiation. These issues remain to be resolved based on new structural design and material exploration.

As a renewable cooling technology, radiative cooling holds promise in mitigating global warming and advancing sustainable development. The theoretical framework of radiative cooling has provided a deep understanding of its thermodynamic processes, fueling the continuous growth in the field of radiative cooling research over the past decade. We anticipate that, based on a unified performance characterization

process and a convincing evaluation system, researchers will be able to better communicate their cutting-edge findings and achieve further breakthroughs in the impending evolution of PDRC materials, ultimately serving as a catalyst for transitioning to a more energy-efficient and sustainable society.

## Data availability statement

All data that support the findings of this study are included within the article (and any supplementary files).

## Acknowledgments

This work is supported by the Natural Science Foundation of Zhejiang Province China Grant (LR22F050006), National Natural Science Foundation of China (NSFC) Grants (62222511 and 61905213), National Key Research and Development Program of China Grant (2023YFF0613000) and the STI 2030–Major Projects Grant (2021ZD0200401). The author would like to acknowledge Weige Lv, Liying Chen, and Wei Wang from the State Key Laboratory for Extreme Photonics and Instrumentation and College of Optical Science and Engineering, Zhejiang University for their assistance in experiments.

## ORCID iDs

Zhuning Wang  <https://orcid.org/0009-0005-4321-9496>  
Yaoguang Ma  <https://orcid.org/0000-0002-8091-611X>

## References

- [1] Staffell I, Pfenninger S and Johnson N 2023 A global model of hourly space heating and cooling demand at multiple spatial scales *Nat. Energy* **8** 1328–44
- [2] Bahadori M N 1978 Passive cooling systems in Iranian architecture *Sci. Am.* **238** 144–55
- [3] Eriksson T S and Granqvist C G 1982 Radiative cooling computed for model atmospheres *Appl. Opt.* **21** 4381–8
- [4] Bijarniya J P, Sarkar J and Maiti P 2020 Review on passive daytime radiative cooling: fundamentals, recent researches, challenges and opportunities *Renew. Sustain. Energy Rev.* **133** 110263
- [5] Raman A P, Anoma M A, Zhu L, Rephaeli E and Fan S 2014 Passive radiative cooling below ambient air temperature under direct sunlight *Nature* **515** 540–4
- [6] Zhai Y, Ma Y, David S N, Zhao D, Lou R, Tan G, Yang R and Yin X 2017 Scalable-manufactured randomized glass-polymer hybrid metamaterial for daytime radiative cooling *Science* **355** 1062–6
- [7] Rephaeli E, Raman A and Fan S 2013 Ultrabroadband photonic structures to achieve high-performance daytime radiative cooling *Nano Lett.* **13** 1457–61
- [8] Zou C, Ren G, Hossain M M, Nirantar S, Withayachumnankul W, Ahmed T, Bhaskaran M, Sriram S, Gu M and Fumeaux C 2017 Metal-loaded dielectric resonator metasurfaces for radiative cooling *Adv. Opt. Mater.* **5** 1700460
- [9] Mandal J, Fu Y, Overvig A C, Jia M, Sun K, Shi N N, Zhou H, Xiao X, Yu N and Yang Y 2018 Hierarchically

- porous polymer coatings for highly efficient passive daytime radiative cooling *Science* **362** 315–9
- [10] Cai C, Wang Y, Wu X, Cai W, Wei Z and Fu Y 2024 An engineered superdurable cellulosic radiative cooling–Power generation wearable metafabric *Chem. Eng. J.* **493** 152599
- [11] Lin K-T, Nian X, Li K, Han J, Zheng N, Lu X, Guo C, Lin H and Jia B 2023 Highly efficient flexible structured metasurface by roll-to-roll printing for diurnal radiative cooling *eLight* **3** 22
- [12] Pian S, Lu C, Wang Z and Ma Y 2024 Stretchable metal–dielectric–metal metasurface for dynamic radiation management *Appl. Opt.* **63** F27–33
- [13] Guo N, Yu L, Shi C, Yan H and Chen M 2024 AFacile and effective design for dynamic thermal management based on synchronous solar and thermal radiation regulation *Nano Lett.* **24** 1447–53
- [14] Cai G, Wang J and Lee P S 2016 Next-generation multifunctional electrochromic devices *Acc. Chem. Res.* **49** 1469–76
- [15] Zhu L, Raman A P and Fan S 2015 Radiative cooling of solar absorbers using a visibly transparent photonic crystal thermal blackbody *Proc. Natl Acad. Sci.* **112** 12282–7
- [16] Li M, Lin C, Li K, Ma W, Doppoophoa B, Li Y and Huang B 2023 A UV-reflective organic–inorganic tandem structure for efficient and durable daytime radiative cooling in harsh climates *Small* **19** 2301159
- [17] Du T, Niu J, Wang L, Bai J, Wang S, Li S and Fan Y 2022 Daytime radiative cooling coating based on the Y<sub>2</sub>O<sub>3</sub>/TiO<sub>2</sub> microparticle-embedded PDMS polymer on energy-saving buildings *ACS Appl. Mater. Interfaces* **14** 51351–60
- [18] Son S, Liu Y, Chae D and Lee H 2020 Cross-linked porous polymeric coating without a metal-reflective layer for sub-ambient radiative cooling *ACS Appl. Mater. Interfaces* **12** 57832–9
- [19] Wang T, Wu Y, Shi L, Hu X, Chen M and Wu L 2021 A structural polymer for highly efficient all-day passive radiative cooling *Nat. Commun.* **12** 365
- [20] Wang Y *et al* 2023 Controllable-morphology polymer blend photonic metafoam for radiative cooling *Mater. Horiz.* **10** 5060–70
- [21] Li T *et al* 2019 A radiative cooling structural material *Science* **364** 760–3
- [22] Liu R, Zhou Z, Mo X, Liu P, Hu B, Duan J and Zhou J 2022 Green-manufactured and recyclable coatings for subambient daytime radiative cooling *ACS Appl. Mater. Interfaces* **14** 46972–9
- [23] Song J, Zhang W, Sun Z, Pan M, Tian F, Li X, Ye M and Deng X 2022 Durable radiative cooling against environmental aging *Nat. Commun.* **13** 4805
- [24] Zhao D, Aili A, Zhai Y, Lu J, Kidd D, Tan G, Yin X and Yang R 2019 Subambient cooling of water: toward real-world applications of daytime radiative cooling *Joule* **3** 111–23
- [25] Zhu L, Raman A, Wang K X, Anoma M A and Fan S 2014 Radiative cooling of solar cells *Optica* **1** 32–38
- [26] Li W, Shi Y, Chen K, Zhu L and Fan S 2017 A comprehensive photonic approach for solar cell cooling *ACS Photonics* **4** 774–82
- [27] Wang Z, Kortge D, Zhu J, Zhou Z, Torsina H, Lee C and Bermel P 2020 Lightweight, passive radiative cooling to enhance concentrating photovoltaics *Joule* **4** 2702–17
- [28] Lee K W, Lim W, Jeon M S, Jang H, Hwang J, Lee C H and Kim D R 2022 Visibly clear radiative cooling metamaterials for enhanced thermal management in solar cells and windows *Adv. Funct. Mater.* **32** 2105882
- [29] Xia T and Wang H 2022 High reflective polyethylene glycol terephthalate package layer for passive daytime radiative cooling in photovoltaic cells *Sol. Energy* **237** 313–9
- [30] Zhang X A, Yu S, Xu B, Li M, Peng Z, Wang Y, Deng S, Wu X, Wu Z, Ouyang M and Wang Y 2019 Dynamic gating of infrared radiation in a textile *Science* **363** 619–23
- [31] Zhang Q, Lv Y, Wang Y, Yu S, Li C, Ma R and Chen Y 2022 Temperature-dependent dual-mode thermal management device with net zero energy for year-round energy saving *Nat. Commun.* **13** 4874
- [32] Fang Z, Ding L, Li L, Shuai K, Cao B, Zhong Y, Meng Z and Xia Z 2021 Thermal homeostasis enabled by dynamically regulating the passive radiative cooling and solar heating based on a thermochromic hydrogel *ACS Photonics* **8** 2781–90
- [33] Chen G *et al* 2023 Printable thermochromic hydrogel-based smart window for all-weather building temperature regulation in diverse climates *Adv. Mater.* **35** 2211716
- [34] Lin C, Hur J, Chao C Y, Liu G, Yao S, Li W and Huang B 2022 All-weather thermochromic windows for synchronous solar and thermal radiation regulation *Sci. Adv.* **8** eabn7359
- [35] Ono M, Chen K, Li W and Fan S 2018 Self-adaptive radiative cooling based on phase change materials *Opt. Express* **26** A777–87
- [36] Wang S, Jiang T, Meng Y, Yang R, Tan G and Long Y 2021 Scalable thermochromic smart windows with passive radiative cooling regulation *Science* **374** 1501–4
- [37] Tang K *et al* 2021 Temperature-adaptive radiative coating for all-season household thermal regulation *Science* **374** 1504–9
- [38] Fan S and Li W 2022 Photonics and thermodynamics concepts in radiative cooling *Nat. Photon.* **16** 182–90
- [39] Zhao D, Aili A, Zhai Y, Xu S, Tan G, Yin X and Yang R 2019 Radiative sky cooling: fundamental principles, materials, and applications *Appl. Phys. Rev.* **6** 021306
- [40] Hossain M M and Gu M 2016 Radiative cooling: principles, progress, and potentials *Adv. Sci.* **3** 1500360
- [41] Zhao B, Hu M, Ao X, Chen N and Pei G 2019 Radiative cooling: a review of fundamentals, materials, applications, and prospects *Appl. Energy* **236** 489–513
- [42] Yu X, Chan J and Chen C 2021 Review of radiative cooling materials: performance evaluation and design approaches *Nano Energy* **88** 106259
- [43] Huang J, Lin C, Li Y and Huang B 2022 Effects of humidity, aerosol, and cloud on subambient radiative cooling *Int. J. Heat Mass Transfer* **186** 122438
- [44] Zhang Q, Rao Z and Ma R 2024 Radiative cooling: arising from practice and in turn serving practice *Nanophotonics* **13** 563–82
- [45] Gueymard C A, Myers D and Emery K 2002 Proposed reference irradiance spectra for solar energy systems testing *Sol. Energy* **73** 443–67
- [46] Goody R and Yung Y 1989 *Atmospheric Radiation* (Oxford University Press)
- [47] Berk A, Conforti P, Kennett R, Perkins T, Hawes F and Den Bosch J V 2014 MODTRAN® 6: a major upgrade of the MODTRAN® radiative transfer code *2014 6th Workshop on Hyperspectral Image and Signal Processing: Evolution in Remote Sensing (WHISPERS)* (IEEE) pp 1–4
- [48] Wang H *et al* 2021 Direct observation and manipulation of hot electrons at room temperature *Natl Sci. Rev.* **8** nwaa295
- [49] Wang H, Guo J, Miao J, Luo W, Gu Y, Xie R, Wang F, Zhang L, Wang P and Hu W 2022 Emerging single-photon detectors based on low-dimensional materials *Small* **18** 2103963
- [50] Harris D C 1998 Durable 3–5 μm transmitting infrared window materials *Infrared Phys. Technol.* **39** 185–201

- [51] Long L, Yang Y and Wang L 2019 Simultaneously enhanced solar absorption and radiative cooling with thin silica micro-grating coatings for silicon solar cells *Sol. Energy Mater. Sol. Cells* **197** 19–24
- [52] Brunt D 1932 Notes on radiation in the atmosphere. I *Q. J. R. Meteorol. Soc.* **58** 389–420
- [53] Angström A K 1936 Effective radiation during the second international polar year
- [54] Bliss Jr R W 1961 Atmospheric radiation near the surface of the ground: a summary for engineers *Sol. Energy* **5** 103–20
- [55] Idso S B and Jackson R D 1969 Thermal radiation from the atmosphere *J. Geophys. Res.* **74** 5397–403
- [56] Staley D and Jurica G 1972 Effective atmospheric emissivity under clear skies *J. Appl. Meteorol.* **11** 349–56
- [57] Idso S B 1981 A set of equations for full spectrum and 8-to 14- $\mu$ m and 10.5-to 12.5- $\mu$ m thermal radiation from cloudless skies *Water Resour. Res.* **17** 295–304
- [58] Granqvist C and Hjortsberg A 1981 Radiative cooling to low temperatures: general considerations and application to selectively emitting SiO films *J. Appl. Phys.* **52** 4205–20
- [59] Andreas E L and Ackley S F 1982 On the differences in ablation seasons of Arctic and Antarctic sea ice *J. Atmos. Sci.* **39** 440–7
- [60] Centeno M 1982 New formulae for the equivalent night sky emissivity *Sol. Energy* **28** 489–98
- [61] Berdahl P and Fromberg R 1982 The thermal radiance of clear skies *Sol. Energy* **29** 299–314
- [62] Lushiku E, Hjortsberg A and Granqvist C 1982 Radiative cooling with selectively infrared-emitting ammonia gas *J. Appl. Phys.* **53** 5526–30
- [63] Berdahl P, Martin M and Sakkal F 1983 Thermal performance of radiative cooling panels *Int. J. Heat Mass Transfer* **26** 871–80
- [64] Lushiku E M and Granqvist C-G 1984 Radiative cooling with selectively infrared-emitting gases *Appl. Opt.* **23** 1835–43
- [65] Martin M and Berdahl P 1984 Characteristics of infrared sky radiation in the United States *Sol. Energy* **33** 321–36
- [66] Berger X, Buriot D and Garnier F 1984 About the equivalent radiative temperature for clear skies *Sol. Energy* **32** 725–33
- [67] Sugita M and Berdahl W 1993 Cloud effect in the estimation of instantaneous downward longwave radiation *Water Resour. Res.* **29** 599–605
- [68] Chen B, Clark D, Maloney J, Mei W and Kasher J 1995 Measurement of night sky emissivity in determining radiant cooling from cool storage roofs and roof ponds *Proc. National Passive Solar Conf.* vol 20 (American Solar Energy Society Inc.) pp 310–3
- [69] Dilley A and O'brien D 1998 Estimating downward clear sky long-wave irradiance at the surface from screen temperature and precipitable water *Q. J. R. Meteorol. Soc.* **124** 1391–401
- [70] Crawford T M and Duchon C E 1999 An improved parameterization for estimating effective atmospheric emissivity for use in calculating daytime downwelling longwave radiation *J. Appl. Meteorol. Climatol.* **38** 474–80
- [71] Niemelä S, Räsänen P and Savijärvi H 2001 Comparison of surface radiative flux parameterizations: part I: longwave radiation *Atmos. Res.* **58** 1–18
- [72] Tang R, Etzion Y and Meir I 2004 Estimates of clear night sky emissivity in the Negev Highlands, Israel *Energy Convers. Manage.* **45** 1831–43
- [73] Lhomme J-P, Vacher J J and Rocheteau A 2007 Estimating downward long-wave radiation on the Andean Altiplano *Agric. For. Meteorol.* **145** 139–48
- [74] Sicart J E, Hock R, Ribstein P and Chazarin J P 2010 Sky longwave radiation on tropical Andean glaciers: parameterization and sensitivity to atmospheric variables *J. Glaciol.* **56** 854–60
- [75] Anon 2006 In-situ measured spectral directional emissivity of snow and ice in the 8–14  $\mu$ m atmospheric window *Remote Sens. Environ.* **100** 486–502
- [76] Parameswaran K and Murthy B K 1990 Altitude profiles of tropospheric water vapor at low latitudes *J. Appl. Meteorol. Climatol.* **29** 665–79
- [77] Sánchez-Lavega A, Pérez-Hoyos S and Hueso R 2004 Clouds in planetary atmospheres: a useful application of the Clausius–Clapeyron equation *Am. J. Phys.* **72** 767–74
- [78] Bao Z, Yibin Y A O and Chaoqian X U 2015 Global empirical model for estimating water vapor scale height *Acta Geod. Cartogr. Sin.* **44** 1085
- [79] Yue C, Hu L and Yan Y 2024 Estimation on the hourly near-surface temperature lapse rate and its time-varying characteristics *Heliyon* **10** e31964
- [80] Jaffer A 2023 Natural convection heat transfer from an isothermal plate *Thermo* **3** 148–75
- [81] Camci M, Karakoyun Y, Acikgoz O and Dalkilic A S 2021 A comparative study on convective heat transfer in indoor applications *Energy Build.* **242** 110985
- [82] Lord S 1992 *NASA Technical Memor.* 103957 (Gemini Observatory)
- [83] Jiankun Z, Meiyang P, Huigao D, Honghui J and Yueqiang H 2023 Review on new infrared stealth structural materials *OEE* **50** 220218–21
- [84] Wu X *et al* 2024 A dual-selective thermal emitter with enhanced subambient radiative cooling performance *Nat. Commun.* **15** 815
- [85] Kang Q, Guo K and Guo Z 2023 A tunable infrared emitter based on phase-changing material GST for visible-infrared compatible camouflage with thermal management *Phys. Chem. Chem. Phys.* **25** 27668–76
- [86] Kang Q, Guo K, Zhang X, Wang W and Guo Z 2024 Dynamically manipulating long-wave infrared polarized thermal radiation by a vanadium dioxide metasurface *Opt. Lett.* **49** 2485–8
- [87] Kang Q, Li D, Wang W, Guo K and Guo Z 2021 Multiband tunable thermal camouflage compatible with laser camouflage based on GST plasmonic metamaterial *J. Appl. Phys.* **55** 065103
- [88] Kang Q, Li D, Guo K, Gao J and Guo Z 2021 Tunable thermal camouflage based on GST plasmonic metamaterial *Nanomaterials* **11** 260
- [89] Chen Z, Zhu L, Raman A and Fan S 2016 Radiative cooling to deep sub-freezing temperatures through a 24-h day–night cycle *Nat. Commun.* **7** 13729
- [90] Dong M, Zhu L, Jiang B, Fan S and Chen Z 2022 Concentrated radiative cooling and its constraint from reciprocity *Opt. Express* **30** 275–85
- [91] Kirchhoff G 1860 I. On the relation between the radiating and absorbing powers of different bodies for light and heat *London, Edinburgh Dublin Phil. Mag. J. Sci.* **20** 1–21
- [92] Yang S, Liu M, Zhao C, Fan S and Qiu C-W 2024 Nonreciprocal thermal photonics *Nat. Photon.* **18** 412–24
- [93] Seeger K 2013 *Semiconductor Physics* (Springer)
- [94] Armelles G, Cebollada A, García-Martín A and González M U 2013 Magnetoplasmonics: combining magnetic and plasmonic functionalities *Adv. Opt. Mater.* **1** 10–35
- [95] Hadad Y, Soric J C and Alu A 2016 Breaking temporal symmetries for emission and absorption *Proc. Natl Acad. Sci.* **113** 3471–5
- [96] Khandekar C, Messina R and Rodriguez A W 2018 Near-field refrigeration and tunable heat exchange through four-wave mixing *AIP Adv.* **8** 055029
- [97] Yu J, Qin R, Ying Y, Qiu M and Li Q 2023 Asymmetric directional control of thermal emission *Adv. Mater.* **35** 2302478

- [98] Zhou J *et al* 2023 Angle-selective thermal emitter for directional radiative cooling and heating *Joule* **7** 2830–44
- [99] Zhao B, Wang J, Zhao Z, Guo C, Yu Z and Fan S 2021 Nonreciprocal thermal emitters using metasurfaces with multiple diffraction channels *Phys. Rev. Appl.* **16** 064001
- [100] Ghanekar A, Wang J, Guo C, Fan S and Povinelli M L 2023 Nonreciprocal thermal emission using spatiotemporal modulation of graphene *ACS Photonics* **10** 170–8
- [101] Ghanekar A, Wang J, Fan S and Povinelli M L 2022 Violation of Kirchhoff's law of thermal radiation with space–time modulated grating *ACS Photonics* **9** 1157–64
- [102] Yu Z and Fan S 2009 Complete optical isolation created by indirect interband photonic transitions *Nat. Photon.* **3** 91–94
- [103] Abedrabbo O, Koç M and Biçer Y 2022 Sustainability performance of space-cooling technologies and approaches *Energy Sources A* **44** 9017–42
- [104] Pian S, Wang Z, Lu C, Wu P, Chen Q, Liu X and Ma Y 2024 Scalable colored Janus fabric scheme for dynamic thermal management *iScience* **27** 110948
- [105] Charlton M, Stanley S A, Whitman Z, Wenn V, Coats T J, Sims M and Thompson J P 2020 The effect of constitutive pigmentation on the measured emissivity of human skin *PLoS One* **15** e0241843
- [106] Wu R *et al* 2024 Spectrally engineered textile for radiative cooling against urban heat islands *Science* **384** 1203–12
- [107] Anon 2020 Spectrally selective approaches for passive cooling of solar cells: a review *Appl. Energy* **262** 114548
- [108] Anon 2024 Optimization of tilt angle for PV in China with long-term hourly surface solar radiation *Renew. Energy* **229** 120741
- [109] Feng J, Santamouris M, Feng J and Santamouris M 2019 Numerical techniques for electromagnetic simulation of daytime radiative cooling: a review *AIMSMATES* **6** 1049–64
- [110] Garnett J M 1904 XII. Colours in metal glasses and in metallic films *Phil. Trans. R. Soc. A* **203** 385–420
- [111] Bruggeman V D 1935 Berechnung verschiedener physikalischer Konstanten von heterogenen Substanzen. I. Dielektrizitätskonstanten und Leitfähigkeiten der Mischkörper aus isotropen Substanzen *Ann. Phys.* **416** 636–64
- [112] Xiang T, Zheng Q and Qin S 2017 Particle size influence on the effective static dielectric constant of composite materials *IEEE Trans. Dielectr. Electr. Insul.* **24** 1197–202
- [113] Nayak J K, Roy Chaudhuri P, Ratha S and Sahoo M R 2023 A comprehensive review on effective medium theories to find effective dielectric constant of composites *J. Electromagn. Waves Appl.* **37** 282–322
- [114] Anon 1995 MCML—Monte Carlo modeling of light transport in multi-layered tissues *Comput. Methods Programs Biomed.* **47** 131–46
- [115] Anon 2019 A strategy of hierarchical particle sizes in nanoparticle composite for enhancing solar reflection *Int. J. Heat Mass Transfer* **131** 487–94
- [116] Yao K, Ma H, Huang M, Zhao H, Zhao J, Li Y, Dou S and Zhan Y 2019 Near-perfect selective photonic crystal emitter with nanoscale layers for daytime radiative cooling *ACS Appl. Nano Mater.* **2** 5512–9
- [117] Yuan H, Yang C, Zheng X, Mu W, Wang Z, Yuan W, Zhang Y, Chen C, Liu X and Shen W 2018 Effective, angle-independent radiative cooler based on one-dimensional photonic crystal *Opt. Express* **26** 27885–93
- [118] Sun K, Riedel C A, Wang Y, Urbani A, Simeoni M, Mengali S, Zalkovskij M, Bilenberg B, de Groot C H and Muskens O L 2018 Metasurface optical solar reflectors using AZO transparent conducting oxides for radiative cooling of spacecraft *ACS Photonics* **5** 495–501
- [119] Kcs L, Liu X, Song X, Xiao C, Wang P, Zhou H and Fan T 2022 A dual-mode infrared asymmetric photonic structure for all-season passive radiative cooling and heating *Adv. Funct. Mater.* **32** 2203789
- [120] Didari-Bader A, Estakhri N M and Mohammadi Estakhri N 2023 Adaptive plasmonic metasurfaces for radiative cooling and passive thermoregulation *Front. Photon.* **4** 1193479
- [121] Yang J, Li Q, Liu S, Fang D, Zhang J, Jin H and Li J 2024 Temperature-adaptive metasurface radiative cooling device with excellent emittance and low solar absorptance for dynamic thermal regulation *AP* **6** 046006
- [122] Zeng S *et al* 2021 Hierarchical-morphology metafabric for scalable passive daytime radiative cooling *Science* **373** 692–6
- [123] Chae D, Kim M, Jung P-H, Son S, Seo J, Liu Y, Lee B J and Lee H 2020 Spectrally selective inorganic-based multilayer emitter for daytime radiative cooling *ACS Appl. Mater. Interfaces* **12** 8073–81
- [124] Tzarouchis D and Sihvola A 2018 Light scattering by a dielectric sphere: perspectives on the Mie resonances *Appl. Sci.* **8** 184
- [125] D'Aguanno G 2015 Coherent thermal emission near 10.6  $\mu\text{m}$  mediated by localized phonon-polariton modes in microparticle arrays *Appl. Phys. Lett.* **106** 031110
- [126] Wang X, Liu X, Li Z, Zhang H, Yang Z, Zhou H and Fan T 2020 Scalable flexible hybrid membranes with photonic structures for daytime radiative cooling *Adv. Funct. Mater.* **30** 1907562
- [127] Zhou K, Li W, Patel B B, Tao R, Chang Y, Fan S, Diao Y and Cai L 2021 Three-dimensional printable nanoporous polymer matrix composites for daytime radiative cooling *Nano Lett.* **21** 1493–9
- [128] Ziming C, Fuqiang W, Dayang G, Huaxu L and Yong S 2020 Low-cost radiative cooling blade coating with ultrahigh visible light transmittance and emission within an “atmospheric window” *Sol. Energy Mater. Sol. Cells* **213** 110563
- [129] Jiang K, Zhang K, Shi Z, Li H, Wu B, Mahian O and Zhu Y 2023 Experimental and numerical study on the potential of a new radiative cooling paint boosted by SiO<sub>2</sub> microparticles for energy saving *Energy* **283** 128473
- [130] Chen G, Wang Y, Qiu J, Cao J, Zou Y, Wang S, Jia D and Zhou Y 2021 A facile bioinspired strategy for accelerating water collection enabled by passive radiative cooling and wettability engineering *Mater. Des.* **206** 109829
- [131] Chen X, He M, Feng S, Xu Z, Peng H, Shi S, Liu C and Zhou Y 2021 Cellulose-based porous polymer film with auto-deposited TiO<sub>2</sub> as spectrally selective materials for passive daytime radiative cooling *Opt. Mater.* **120** 111431
- [132] Jing W, Zhang S, Zhang W, Chen Z, Zhang C, Wu D, Gao Y and Zhu H 2021 Scalable and flexible electrospun film for daytime subambient radiative cooling *ACS Appl. Mater. Interfaces* **13** 29558–66
- [133] Dong S, Wu Q, Zhang W, Xia G, Yang L and Cui J 2022 Slippery passive radiative cooling supramolecular siloxane coatings *ACS Appl. Mater. Interfaces* **14** 4571–8
- [134] Iqbal M I, Lin K, Sun F, Chen S, Pan A, Lee H H, Kan C-W, Lin C S K and Tso C Y 2022 Radiative cooling nanofabric for personal thermal management *ACS Appl. Mater. Interfaces* **14** 23577–87
- [135] Li X, Peoples J, Yao P and Ruan X 2021 Ultrawhite BaSO<sub>4</sub> paints and films for remarkable daytime subambient radiative cooling *ACS Appl. Mater. Interfaces* **13** 21733–9
- [136] Anon 2019 Selection of polymers with functional groups for daytime radiative cooling *Mater. Today Phys.* **10** 100127
- [137] Zhang X *et al* 2023 Scalable bio-skin-inspired radiative cooling metafabric for breaking trade-off between optical

- properties and application requirements *ACS Photonics* **10** 1624–32
- [138] Anon 2023 Scalable nanofibrous silk fibroin textile with excellent Mie scattering and high sweat evaporation ability for highly efficient passive personal thermal management *Chem. Eng. J.* **466** 143127
- [139] Xue X *et al* 2020 Creating an eco-friendly building coating with smart subambient radiative cooling *Adv. Mater.* **32** 1906751
- [140] Zhou Z, Wang X, Ma Y, Hu B and Zhou J 2020 Transparent polymer coatings for energy-efficient daytime window cooling *Cell Rep. Phys. Sci.* **1** 100231
- [141] Mandal J, Yang Y, Yu N and Raman A P 2020 Paints as a scalable and effective radiative cooling technology for buildings *Joule* **4** 1350–6
- [142] Wang N, Lv Y, Zhao D, Zhao W, Xu J and Yang R 2022 Performance evaluation of radiative cooling for commercial-scale warehouse *Mater. Today Energy* **24** 100927
- [143] Lin K *et al* 2023 Hierarchically structured passive radiative cooling ceramic with high solar reflectivity *Science* **382** 691–7
- [144] Zhao X *et al* 2023 A solution-processed radiative cooling glass *Science* **382** 684–91
- [145] Chowdhary A K, Bhowmik T and Sikdar D 2022 Infrared-blocking plasmonic meta-glass for energy-saving passive windows *Opt. Lett.* **47** 2242–5
- [146] Huang G *et al* 2024 Radiative cooling and indoor light management enabled by a transparent and self-cleaning polymer-based metamaterial *Nat. Commun.* **15** 3798
- [147] Li G, Wang J, Zhao X, Su Y and Zhao D 2023 Simultaneous modulation of solar and longwave infrared radiation for smart window applications *Mater. Today Phys.* **38** 101284
- [148] Mustafa M N, Mohd Abdah M A A, Numan A, Moreno-Rangel A, Radwan A and Khalid M 2023 Smart window technology and its potential for net-zero buildings: a review *Renew. Sustain. Energy Rev.* **181** 113355
- [149] Niu Y *et al* 2022 Energy saving and energy generation smart window with active control and antifreezing functions *Adv. Sci.* **9** 2105184
- [150] Hsu P-C, Song A Y, Catrysse P B, Liu C, Peng Y, Xie J, Fan S and Cui Y 2016 Radiative human body cooling by nanoporous polyethylene textile *Science* **353** 1019–23
- [151] Cai L, Peng Y, Xu J, Zhou C, Zhou C, Wu P, Lin D, Fan S and Cui Y 2019 Temperature regulation in colored infrared-transparent polyethylene textiles *Joule* **3** 1478–86
- [152] Miao D, Cheng N, Wang X, Yu J and Ding B 2022 Integration of Janus wettability and heat conduction in hierarchically designed textiles for all-day personal radiative cooling *Nano Lett.* **22** 680–7
- [153] Peng Y *et al* 2018 Nanoporous polyethylene microfibres for large-scale radiative cooling fabric *Nat. Sustain.* **1** 105–12
- [154] Cai L *et al* 2018 Spectrally selective nanocomposite textile for outdoor personal cooling *Adv. Mater.* **30** 1802152
- [155] Cheng N, Miao D, Wang C, Lin Y, Babar A A, Wang X, Wang Z, Yu J and Ding B 2023 Nanosphere-structured hierarchically porous PVDF-HFP fabric for passive daytime radiative cooling via one-step water vapor-induced phase separation *Chem. Eng. J.* **460** 141581
- [156] Wu X *et al* 2023 An all-weather radiative human body cooling textile *Nat. Sustain.* **6** 1446–54
- [157] Wu X-E *et al* 2024 Durable radiative cooling multilayer silk textile with excellent comprehensive performance *Adv. Funct. Mater.* **34** 2313539
- [158] Xue S, Huang G, Chen Q, Wang X, Fan J and Shou D 2024 Personal thermal management by radiative cooling and heating *Nano-Micro. Lett.* **16** 153
- [159] Xie L *et al* 2023 Facile “synergistic inner–outer activation” strategy for nano-engineering of nature-skin-derived wearable daytime radiation cooling materials *Small* **19** 2207602
- [160] Zhu B *et al* 2021 Subambient daytime radiative cooling textile based on nanoprocessed silk *Nat. Nanotechnol.* **16** 1342–8
- [161] Zanatta A R 2022 The Shockley–Queisser limit and the conversion efficiency of silicon-based solar cells *Results Opt.* **9** 100320
- [162] Ananda W 2017 External quantum efficiency measurement of solar cell. *2017 15th Int. Conf. on Quality in Research (QIR) : Int. Symp. on Electrical and Computer Engineering 2017* pp 450–6
- [163] Polman A and Atwater H A 2012 Photonic design principles for ultrahigh-efficiency photovoltaics *Nat. Mater.* **11** 174–7
- [164] Liu G, Xu J, Chen T and Wang K 2022 Progress in thermoplasmonics for solar energy applications *Phys. Rep.* **981** 1–50
- [165] Wang K, Luo G, Guo X, Li S, Liu Z and Yang C 2021 Radiative cooling of commercial silicon solar cells using a pyramid-textured PDMS film *Sol. Energy* **225** 245–51
- [166] An Y, Sheng C and Li X 2019 Radiative cooling of solar cells: opto-electro-thermal physics and modeling *Nanoscale* **11** 17073–83
- [167] Heo S-Y, Kim D H, Song Y M and Lee G J 2022 Determining the effectiveness of radiative cooler-integrated solar cells *Adv. Energy Mater.* **12** 2103258
- [168] Chen J, Lu L, Gong Q, Lau W Y and Cheung K H 2021 Techno-economic and environmental performance assessment of radiative sky cooling-based super-cool roof applications in China *Energy Convers. Manage.* **245** 114621
- [169] Ott D H and Ross R G 1983 Assessing photovoltaic module degradation and lifetime from long term environmental tests Institute of Environmental Sciences Annual Technical Meeting (Los Angeles, CA)
- [170] Raman A P, Li W and Fan S 2019 Generating light from darkness *Joule* **3** 2679–86
- [171] Yu L, Xi Z, Li S, Pang D, Yan H and Chen M 2022 All-day continuous electrical power generator by solar heating and radiative cooling from the sky *Appl. Energy* **322** 119403
- [172] Sun H, Tang F, Bi Y, Sun H, Huang L, Jiang F, Chen L and Li J 2023 Hierarchically porous cellulose membrane via self-assembly engineering for ultra high-power thermoelectrical generation in natural convection *Adv. Funct. Mater.* **33** 2307960
- [173] Xu J, Zhang J, Fu B, Song C, Shang W, Tao P and Deng T 2020 All-day freshwater harvesting through combined solar-driven interfacial desalination and passive radiative cooling *ACS Appl. Mater. Interfaces* **12** 47612–22
- [174] Zhang Y *et al* 2022 Atmospheric water harvesting by large-scale radiative cooling cellulose-based fabric *Nano Lett.* **22** 2618–26
- [175] Li J, Liang Y, Li W, Xu N, Zhu B, Wu Z, Wang X, Fan S, Wang M and Zhu J 2022 Protecting ice from melting under sunlight via radiative cooling *Sci. Adv.* **8** eabj9756
- [176] Chowdhary A K, Reddy V A and Sikdar D 2021 Selective thermal emitters for high-performance all-day radiative cooling *J. Appl. Phys.* **55** 085504
- [177] Chowdhary A K, Reddy V A and Sikdar D 2022 Nanophotonics-enabled high-efficiency selective solar absorbers for waste heat management *IEEE Trans. Nanotechnol.* **21** 131–6
- [178] Haechler I, Park H, Schnoering G, Gulich T, Rohner M, Tripathy A, Milionis A, Schutzius T M and Poulikakos D 2021 Exploiting radiative cooling for uninterrupted

- 24-hour water harvesting from the atmosphere *Sci. Adv.* **7** eabf3978
- [179] Xi Z, Li S, Yu L, Yan H and Chen M 2022 All-day freshwater harvesting by selective solar absorption and radiative cooling *ACS Appl. Mater. Interfaces* **14** 26255–63
- [180] Zhou M *et al* 2021 Vapor condensation with daytime radiative cooling *Proc. Natl Acad. Sci.* **118** e2019292118
- [181] Nilsson T, Vargas W E, Niklasson G A and Granqvist C 1994 Condensation of water by radiative cooling *Renew. Energy* **5** 310–7
- [182] Haddad O, Al-Nimr M and Maqableh A 2000 Enhanced solar still performance using a radiative cooling system *Renew. Energy* **21** 459–69
- [183] Jacobs A, Heusinkveld B and Berkowicz S 2008 Passive dew collection in a grassland area, The Netherlands *Atmos. Res.* **87** 377–85
- [184] Zhang Y, Wang F, Yu Y, Wu J, Cai Y, Shi J, Morikawa H and Zhu C 2023 Multi-bioinspired hierarchical integrated hydrogel for passive fog harvesting and solar-driven seawater desalination *Chem. Eng. J.* **466** 143330
- [185] Yang R, Niu D, Pu J H, Tang G, Wang X and Du M 2022 Passive all-day freshwater harvesting through a transparent radiative cooling film *Appl. Energy* **325** 119801
- [186] Huang M-C *et al* 2023 Scalable multifunctional radiative cooling materials *Prog. Mater. Sci.* **137** 101144
- [187] Wu S, Cao Y, Li Y and Sun W 2023 Recent advances in material engineering and applications for passive daytime radiative cooling *Adv. Opt. Mater.* **11** 2202163
- [188] Hsu P-C *et al* 2017 A dual-mode textile for human body radiative heating and cooling *Sci. Adv.* **3** e1700895
- [189] Yue X, Zhang T, Yang D, Qiu F, Wei G and Zhou H 2019 Multifunctional Janus fibrous hybrid membranes with sandwich structure for on-demand personal thermal management *Nano Energy* **63** 103808
- [190] Luo H, Zhu Y, Xu Z, Hong Y, Ghosh P, Kaur S, Wu M, Yang C, Qiu M and Li Q 2021 Outdoor personal thermal management with simultaneous electricity generation *Nano Lett.* **21** 3879–86
- [191] Dai B, Li X, Xu T and Zhang X 2022 Radiative cooling and solar heating Janus films for personal thermal management *ACS Appl. Mater. Interfaces* **14** 18877–83
- [192] Shi M, Song Z, Ni J, Du X, Cao Y, Yang Y, Wang W and Wang J 2023 Dual-mode porous polymeric films with coral-like hierarchical structure for all-day radiative cooling and heating *ACS Nano* **17** 2029–38
- [193] Li X, Sun B, Sui C, Nandi A, Fang H, Peng Y, Tan G and Hsu P-C 2020 Integration of daytime radiative cooling and solar heating for year-round energy saving in buildings *Nat. Commun.* **11** 6101
- [194] Yang Z, Jia Y and Zhang J 2022 Hierarchical-morphology metal/polymer heterostructure for scalable multimodal thermal management *ACS Appl. Mater. Interfaces* **14** 24755–65
- [195] Ke Y, Li Y, Wu L, Wang S, Yang R, Yin J, Tan G and Long Y 2022 On-demand solar and thermal radiation management based on switchable interwoven surfaces *ACS Energy Lett.* **7** 1758–63
- [196] Leung E M *et al* 2019 A dynamic thermoregulatory material inspired by squid skin *Nat. Commun.* **10** 1947
- [197] Zhao H, Sun Q, Zhou J, Deng X and Cui J 2020 Switchable cavitation in silicone coatings for energy-saving cooling and heating *Adv. Mater.* **32** 2000870
- [198] Liu X, Pian S, Zhou R, Shen H, Liu X, Yang Q and Ma Y 2020 Tunable radiative cooling based on a stretchable selective optical filter *J. Opt. Soc. Am. B* **37** 2534–7
- [199] Mandal J, Jia M, Overvig A, Fu Y, Che E, Yu N and Yang Y 2019 Porous polymers with switchable optical transmittance for optical and thermal regulation *Joule* **3** 3088–99
- [200] Dastidar S, Alam M M, Crispin X, Zhao D and Jonsson M P 2022 Janus cellulose for self-adaptive solar heating and evaporative drying *Cell Rep. Phys. Sci.* **3** 101196
- [201] Fei J *et al* 2022 Switchable surface coating for bifunctional passive radiative cooling and solar heating *Adv. Funct. Mater.* **32** 2203582
- [202] Rao Y, Dai J, Sui C, Lai Y-T, Li Z, Fang H, Li X, Li W and Hsu P-C 2021 Ultra-wideband transparent conductive electrode for electrochromic synergistic solar and radiative heat management *ACS Energy Lett.* **6** 3906–15
- [203] Sui C *et al* 2023 Dynamic electrochromism for all-season radiative thermoregulation *Nat. Sustain.* **6** 428–37
- [204] Sheng S-Z *et al* 2023 Nanowire-based smart windows combining electro- and thermochromics for dynamic regulation of solar radiation *Nat. Commun.* **14** 3231
- [205] Shao Z *et al* 2022 All-solid-state proton-based tandem structures for fast-switching electrochromic devices *Nat. Electron.* **5** 45–52
- [206] Mandal J, Du S, Dontigny M, Zaghib K, Yu N and Yang Y 2018 Li<sub>4</sub>Ti<sub>5</sub>O<sub>12</sub>: a visible-to-infrared broadband electrochromic material for optical and thermal management *Adv. Funct. Mater.* **28** 1802180
- [207] Chowdhary A K and Sikdar D 2020 Low-power design of electrotunable color filters and optical switches *J. Opt. Soc. Am. B* **37** 3865–73
- [208] Chowdhary A K and Sikdar D 2021 Design of electrotunable all-weather smart windows *Sol. Energy Mater. Sol. Cells* **222** 110921
- [209] Babulanam S, Eriksson T, Niklasson G and Granqvist C 1987 Thermochromic VO<sub>2</sub> films for energy-efficient windows *Sol. Energy Mater.* **16** 347–63
- [210] Xu L, Sun D-W, Tian Y, Sun L and Zhu Z 2024 Self-rehydrating and highly entangled hydrogel for sustainable daytime passive cooling *Chem. Eng. J.* **479** 147795
- [211] Liu M *et al* 2023 Continuous photothermal and radiative cooling energy harvesting by VO<sub>2</sub> smart coatings with switchable broadband infrared emission *ACS Nano* **17** 9501–9
- [212] Li G, Chen J, Yan Z, Wang S, Ke Y, Luo W, Ma H, Guan J and Long Y 2023 Physical crosslinked hydrogel-derived smart windows: anti-freezing and fast thermal responsive performance *Mater. Horiz.* **10** 2004–12
- [213] Fan C, Long Z, Zhang Y, Mensah A, He H, Wei Q and Lv P 2023 Robust integration of energy harvesting with daytime radiative cooling enables wearing thermal comfort self-powered electronic devices *Nano Energy* **116** 108842